A Dissertation

Entitled

Issues in the Development of All-Sputtered ZnO/CdS/CdTe Flexible Solar Cells

By

Anthony Clark Vasko

Submitted as partial fulfillment of the requirements for

The Doctor of Philosophy in Physics

_____

Advisor: Dr. Alvin D. Compaan

_____

College of Graduate Studies

The University of Toledo

August 2009

An Abstract of

Issues in the Development of All-Sputtered ZnO/CdS/CdTe Flexible Solar Cells

Anthony Clark Vasko

Submitted as partial fulfillment of the requirements for

The Doctor of Philosophy in Physics

The University of Toledo

August 2009

Cadmium telluride (CdTe) solar cells are traditionally made on glass in a superstrate configuration, taking advantage of the transparency and mechanical rigidity of glass, as well as the ability to form the back contact last.   However, there are advantages to fabricating solar cells on flexible substrates such as plastic sheets. Advantages include high specific powers (power generated per mass of the device) for low weight applications, the possibility for continuous roll-to-roll manufacturing suitable for industry, and the opportunity to place solar devices on objects and structures that are not necessarily flat.

We have fabricated various flexible CdTe devices through sputter deposition, using aluminum doped zinc oxide (AZO) as a transparent conducting oxide (TCO) top contact. Early devices, made by naively applying fabrication techniques used with glass cells, had poor performance. This inspired several investigations.

Traditional simple heuristic analysis of solar cell current-voltage curves assumes the cell is reasonably performing and that series and shunt resistance losses are small. This was not true for our early cells, inspiring us to derive a simple model for very poor cells.

Early cells showed significant losses due to both series and shunt resistance. Series resistance losses in flexible cells inspired us to investigate more deeply series resistance losses in general, resulting in a fairly simple model that relates fill factor losses, in dot cells made in a typical geometry, to TCO sheet resistance. This model was confirmed by experiment.

Series resistance losses also led to futher investigation of AZO properties. We have found that AZO sheet resistance increases during cell fabrication, but a model that is supported by experiment indicates that the resistivity change is limited to a finite thickness of material. This allows fabrication of AZO which remains of good sheet resistance throughout the fabrication process.

Shunt resistance losses inspired a study of highly resistive and transparent (HRT) zinc oxide made by reactive sputtering with oxygen, which can be used as a buffer for shunts. Data on resisitivity as a function of oxygen in the sputter gas is given when using doped and undoped zinc oxygen sputter targets. Calculations on theoretical effects of such buffer layers are also presented.

A high temperature cadmium chloride ($CdCl_2$) treatment is needed to create high efficiency CdTe cells. This can be a difficult step for flexible cells, as it can lead to CdTe film delamination. We have optimized a treatment for flexible cells and found that

conditions, different from those which are optimal for cells on glass, allows high performance with no delamination.

Understanding of these issues allowed progress in the performance of our cells fabricated on flexible substrates. Ultimately, we have fabricated a flexible CdTe cell with efficiency of 10.5%. This efficiency is, to our knowledge, the best of any flexible CdTe cell which uses zinc oxide as a transparent conducting oxide. The performance of these cells also compares favorably to the best overall flexible CdTe cells.

Acknowledgements

Table of Contents

ix

List of Figures

List of Tables

Chapter 1 - Introduction

Our research is on flexible cadmium telluride (CdTe) solar cells. In this chapter,

we will begin by considering the broadest relevant context, that of energy in general, then

focus on narrower contexts, covering solar energy and solar energy technology, then

broad CdTe issues. Finally, we will review previous work on flexible CdTe cells, then

our own recent work in the field and outline the remainder of the thesis.

1.1 Global Overview

1.1.1 Energy and Fossil Fuels

Ever since 1882, when commercial power lines were first strung, serving 59 New

York households with Edison's direct current, electricity has become ubiquitous in our

society.   US residences with electricity have increased from 8% in 1907 to 98% in 1956

[1]. As access has increased, so has usage. Individual energy usage had grown almost

exponentially until the 1970's, when rising prices slowed the rate of usage increase.

In 2007, the world consumed energy at an average rate of 15.8 terawatts.   The

United States uses more energy overall than any other nation. In 2005, it consumed at an

average rate of 3.3 terawatts. Of that, 1.27 terawatts were from petroleum, the majority

of which was used for transportation. About 0.75 terawatts were from coal and natural

gas each. 0.26 terawatts were from nuclear. The most prominent renewable energy source, hydroelectric, contributes only 0.1 terawatts.

In total, 84% of the United State's energy is produced from fossil fuels. While the United States accounts for 21% of the world's energy consumption and 25% of the world's petroleum consumption, only 3% of the world's known oil reserves are within its borders. The United State's dependence on foreign oil is not only a source of a trade deficit but also one of its greatest threats to its security. Beyond the United States, the world's oil supply also is finite. Moreover, fossil fuel availability will not become a problem when the supply has been completely depleted, but merely when production reaches a maximum while demand continues to increase (this is the theory of "peak oil")[2]. Projections for when the world's oil output will peak vary, from imminently to within a century. The United State's oil output has already peaked, in the 1970's.

The United States does have considerable coal reserves. Its supplies are projected to last over a hundred years. However, by 2007, the majority of evidence suggests that global warming observed since the 1960's has anthropogenic causes, primarily the burning of fossil fuels, especially coal.

Clearly, for our society to maintain and improve its lifestyle over the long term, alternatives to fossil fuels need to be implemented.

1.1.2 Renewable Energy and Solar

Although Edison delivered the first commercial power in 1882, his efforts were eclipsed in 1896 when Westingtonhouse, using Tesla's alternating current system, tapped

Niagara Falls to deliver power to industry in Buffalo, New York. To this day, hydroelectric energy is the most used renewable source of electricity in the world.

Hydroelectric sources currently generate 0.7 terawatts of power world-wide and have an estimated capacity to generate 7.2 terawatts. Aside from its production capacity, hydroelectric dams, once built, can generate energy for a long time. Some plants that are one hundred years old are still in operation. A disadvantage of hydroelectric power is the effects a dam can have on an ecosystem. Salmon has difficulty swimming upstream (an important part of its breeding cycle) in rivers with hydroelectric plants, water leaving a turbine can cause erosion of rivers (more efficiently than other water, due to temperature differences and a low amount of silt in water leaving turbines), and even human populations may need to be relocated so dams can be built (such as over one million for the Three Gorges Dam on the Yang Tse River in China).

Wind has the potential to produce even more energy than water. Although currently only 0.09 TW are generated from wind, 72 TW are predicted to be available. Wind is intermittent (in fact, unpredictably intermittent) and cannot be expected to provide society with a continuous source of electricity by itself, at least until battery storage technology improves. Wind turbines also can produce noise and kill birds.

Geothermal energy has an estimated potential of about 70 GW. This number depends on the technology used to utilize the energy from the Earth's internal heat. The actual heat flow from the center of the Earth is estimated as being much higher, around 9 TW. Currently, only 10 GW of electricity are produced from geothermal sources, with another 33 GW of geothermal used directly for heating.

Geothermal energy comes from heat produced by decaying radioactive material in the center of the Earth. All other forms, such as hydroelectricity, wind, fossil fuels, and biomaterials, ultimately come, or came, from the Sun. (And even the radioactive elements responsible for geothermal energy had stellar origins) Thus, we would expect energy from sunlight to be by far the most plentiful renewable resource. This is in fact the case.

1.2 Solar Energy

As the focus of this thesis is related to solar energy in particular, it will be discussed in more detail than previous forms of energy.

1.2.1 Solar Energy Availability

Let us do a back-of-the-envelope style estimate of the amount of solar energy that strikes the Earth. If we have forgotten the Stefan-Boltzmann constant, we can find a number with the proper units by combining the relevant constants h-bar, k and c. The proper combination is

$$\sigma \approx \frac{k_B^4}{\hbar^3 c^2}$$

Using further rules of thumb $k_B \approx 1/40$ eV/(295K), $\hbar c \approx 197$ eV-nm, and $c \approx 3 \times 10^8$m/s, this gives $\sigma \approx 2.0 \times 10^{-15}$ eV-m/(s-nm^3-K^4) $= 2.0 \times 10^{12}$ eV/(s-m^2-K^4). We as physicists also probably remember that 1eV $= 1.6 \times 10^{-19}$J, so $\sigma \approx 3.2 \times 10^{-7}$ W/(m^2-K^4). We can say that one million (an easy to remember number) Earths would fit in the Sun so the Sun has a radius 100 times that of the Earth. Although this is unfortunately no longer taught in schools, a meter was originally defined such that the distance from the North Pole to the equator

along the prime meridian was ten million meters. This implies that the Earth has a radius

of 6,400 kilometers. The Sun then has a radius of 640 megameters, and with a corona

temperature of about 6000K, releases energy in the form of photons at a rate of 2.2×10^{27}

watts. We also might remember that light from the Sun takes 8.5 minutes to reach the

Earth. This implies a distance of 1.5×10^{11}m. The Earth's cross section subtends a solid

angle of $\pi r_{Earth}^2/d_{Earth-Sun}^2$, and thus (dividing by a total of 4π steradians) intercepts a

$r_{Earth}^2/(4d_{Earth-Sun}^2)$ fraction of the power of the sun. Then that energy is distributed over

Earth's cross sectional area of $1/(\pi r_{Earth}^2)$, so that the average power density delivered to

the (daytime side of) Earth's atmosphere is $1/(\pi d_{Earth-Sun}^2)$ x Psun = 7900 W/m^2.

The only major problem with our back-of-the-envelope method is that the

Stephan-Boltzmann constant has a constant prefactor that is not given by unit analysis.

Rigorous derivation using Planck's blackbody model reveals that the prefactor is $\pi^2/60 \approx$

1/6. 7900 W/m^2 / 6 = 1300 W/m^2, which is very close to the accepted value of the solar

constant, 1366 W/m^2. It is fairly easy to remember (at least if you are a solar energy

researcher) that the solar power density delivered to the Earth's surface is 1000 W/m^2.

The solar radiation intensity is reduced to that value from 1366 W/m^2 due to absorption

in the atmosphere (in particular, after traveling through the atmosphere at an angle of

$\cos^{-1}(1/1.5) = 48°$, a so-called air mass of 1.5, leading to the AM1.5 spectrum)

The 1000W/m^2 power density is then reduced by two other factors. First, and

obviously, it is reduced by a factor of 2 due to the Earth's day / night cycle. Secondly, it

is reduced by a geometric factor due to light generally not striking the Earth's surface

perpendicularly. Figure 1.1 shows the derivation for this factor; assuming the direction

rays from the sun (which are essentially parallel at the Earth) travel is along y, we need to

find the average value of y dot r over a unit hemisphere. The integral of the dot product is π. The average of the dot product is that integral divided by the area (2π) of the hemisphere, so the average is 1/2.
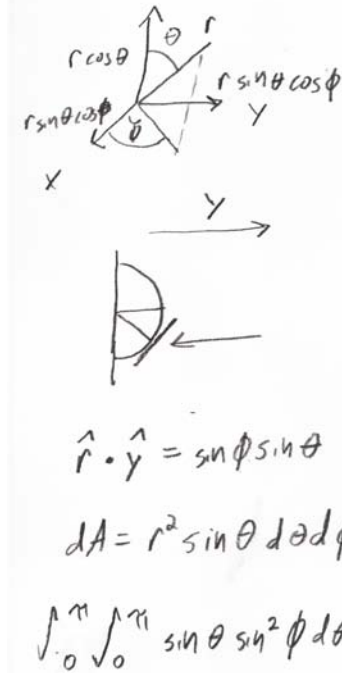
Figure 1.1 – Derivation of the geometric correction to the incoming power from the sun.

Sunlight travels along the y direction, and strikes the Earth's surface, which is perpendicular to r. The projection of r along y is sinθsinϕ, which is also the dot product of the two unit vectors. The remaining integration is straight forward.

Therefore, over a day, the average insolation is about 250 W/m^2. Integrating over the entire 5×10^{14} m^2 surface area of the Earth gives that, over a day, the Earth receives power from the sun at a rate of 1.3×10^{17} W. This is a tremendous amount of power, more than 8000 times the energy consumption of the Earth's entire human population. Alternatively, if a tenth of a percent of the world's surface was covered with 10% efficient solar cells (a figure that is today technologically feasible), those cells would almost be sufficient to supply the entire human race with energy. Figure 1.2 shows the power the Earth receives from the sun, averaged over a year, as a function of geography. The maximum energy is about 350 W/m^2. Even at the equator, light does not constantly strike any spot perpendicularly. In that case, the geometric factor is 2/π, and

$500\text{W/m}^2 * 2/\pi = 318 \text{ W/m}^2$. This is slightly less than 350 because sunlight at the equator does not travel through an air mass of 1.5 but rather through an air mass of 1, so the maximum solar flux is greater than 1000 W/m^2.
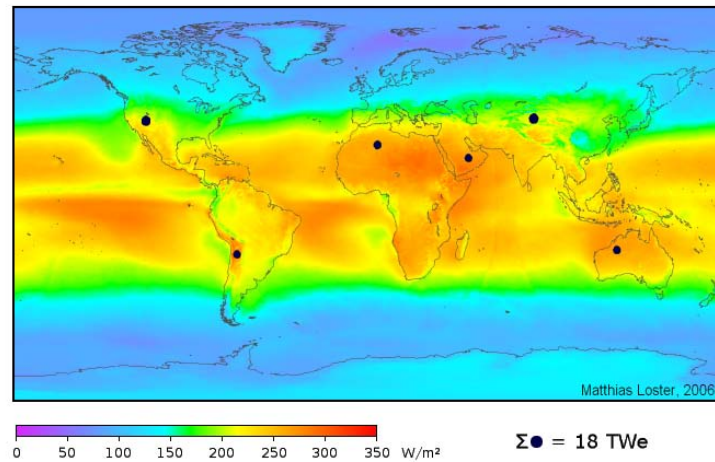
Figure 1.2 – Distribution of solar power delivered to the Earth's surface. Data is averaged over a year. Solar energy plants at the areas indicated by and of the size of the dots, using 8% efficient devices, would be sufficient to produce 18 terawatts of electrical energy, enough to cover the entire human race's energy needs.[3]

1.2.2 Disadvantages of Solar Power

In my experience, the most common layman objection to solar power is, "What will we do when it's night?" Obviously, solar power is not available when the sun has set. In the short term, this is unlikely to be a problem since instantly converting all of our sources of electricity to solar is unrealistic. Solar power works well by supplementing existing power plants. Energy consumption as a function of time throughout the day is at a maximum during the day when workplaces and offices are open. The output of coal and nuclear plants cannot easily be finely adjusted over periods of time as short as a day, so they must be running constantly, day and night, at a rate needed to meet the maximum

demand during the day. Solar energy could be used to supply the difference between day and night energy consumption, allowing other plants to run at a lower level.

In the long term, if we were ever to hope to replace fossil fuels entirely with solar, the day-night cycle would be more of a problem. It would be necessary to generate excess energy during the day and store it for use at night. Storage technologies (such as batteries) are not yet capable of solving this demanding problem.

More important as a short term issue is cost. It is perhaps understandable that fossil fuels, which basically (granted, this is a simplification) require extracting something from the ground and burning it, should be less expensive than solar cells, which are a relatively new technology, and whose technology continues to be refined. There is an arcane (at least to scientists who have not studied business) issue, however: The Time Value of Money.

Let us do a simple estimate. A solar panel might cost $12 / watt installed. It might last 25 years. If it operated 10 hours a day for 25 years, it would generate 91 kilowatt-hours per installed watt.   This comes to a final cost of 13 cents per kilowatt-hour. This is comparable to the cost of electricity generated by fossil fuels, which may be 12 cents per kilowatt-hour. However, fossil fuels are paid for as they are needed. A solar panel needs to be paid for upfront.

Suppose you needed 1 kilowatt for your personal needs during the day at home. A solar installation to cover those needs could cost $12,000. On the other hand, your electric bill using municipal power at that rate, for 10 hours a day, could be $36 a month. After 28 years, then it seems the two costs would be equal. If today you had $12,000, you could buy the solar panels, or you could pay $36 a month for grid electricity, and

invest the remainder. Assuming an interest rate of 3% per year (for reference, the Federal Reserve interest rate was 3.5% before the September 11th attacks), compounded monthly, at the end of 28 years, using the latter plan, you would still have $88000 remaining. Thus the solar cells would effectively cost, considering the time value of money, not $12,000 but $20,800, for an effective price rate of 21 cents a watt. If the only concern was cost, it would be a better decision to simply continue to use fossil fuel generated electricity.

Another factor influencing the time value of money is inflation, which may also have a 3% annual rate. Interest and inflation rates are somewhat unpredictable, so such calculations can be complex and subject to uncertainty. This may be why investment bankers make so much more money than scientists. At the time of this writing, the United States is experiencing a recession and many investors have been losing rather than earning money. In such times, solar systems reliably produce value every day with the rising of the sun. See Figure 1.3.
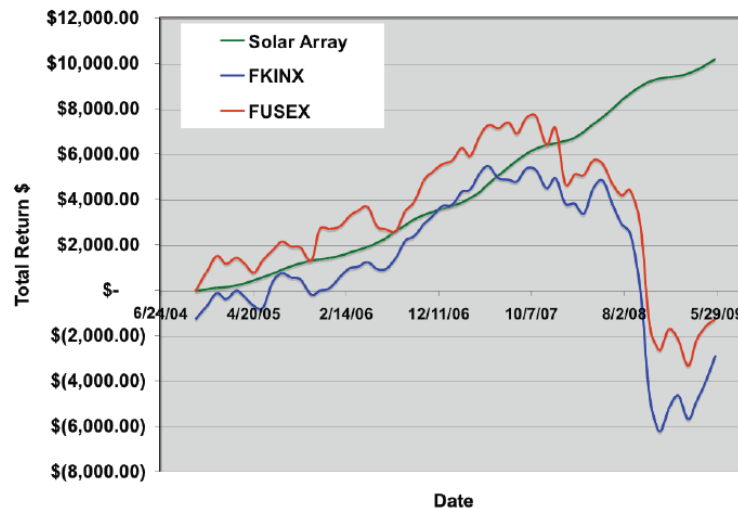
Figure 1.3. Comparison of after tax returns on investment for a solar array system, Fidelity Investments FUSEX Mutual Fund and Franklin Templeton Investments FKINX Mutual Fund. Installed solar systems are immune to poor market performance as seen in 2008.[4]

9

There is a drive to lower the cost of solar. Since the cost is measured in terms of dollar per power, a cell that generates more power (by being more efficient) at the same price will produce less expensive electricity; or a cell that generates the same power but costs less (by having reduced manufacturing costs) will produce less expensive electricity. It would even be tolerable, for instance, to have *less* efficient cells if the manufacturing costs were reduced by so much to more than compensate.

In any case, as of this writing, First Solar is approaching grid parity. Grid parity is when the cost of solar is equal to the cost of conventional electricity. Partially, First Solar is achieving this through building CdTe modules which are less expensive than traditional silicon modules. Another factor is that government subsidies, intended to encourage environmentally friendly policies, lower the price. Subsidies may not seem to be a long term solution to keeping costs down (and could be argued that they don't so much reduce the cost as simply shift it somewhere else). However, solar is a developing industry and lower prices now can encourage new factories and larger markets, and then economies of scale can reduce costs on a more permanent basis.

1.2.3 Photovoltaic Energy Conversion Technologies

Various technologies exist to convert photons to electricity. Generic traits of such technologies are a diode-like structure to provide an electric field to separate charge carriers, transparent "window" layers to allow light to enter the structure (including a transparent conducting oxide, or TCO, that both allows light to enter, and collection of the resulting current), and an absorber layer that absorbs light, converting photons to electron-hole pairs. The technologies are generally named after the absorber layer.

1.2.3.1 Crystalline Silicon

Crystalline silicon is the oldest and most pervasive form of photovoltaic technology. In 1939, Russell Ohl, working at Bell Labs, discovered the p-n junction. In 1946, he published patent 2402662, "Light sensitive device," a silicon device that converted light into electricity. A Time Magazine article (May 3rd, 1954) reported Bell's solar "batteries" could produce 50 watts per square yard, making them about 5% efficient.

Today, crystalline silicon solar cells account for 90% of the world's solar energy supply. The world record laboratory cell is 24.7% efficient.

The advantage of crystallinity of the silicon is fewer defects exist within the material to trap charge carriers. Consequently, single silicon cells are more efficient than any cells made of polycrystalline material. Single crystal devices are also easier to understand theoretically.

Crystalline silicon has a relatively low absorption coefficient. See Figure 1.4. This is a consequence of its having an indirect bandgap. The lowest energy photon it can absorb is 1.1eV, but to absorb a photon at that energy it must also absorb a crystal lattice vibration to conserve momentum. Since this requires a coincidence of two events (a second order perturbation), it is less likely. Consequently, crystalline silicon solar cells must be thicker than direct gap multicrystalline cells. A goal for a good "thin" crystalline silicon cell would be 50-100μm, whereas a goal for a thin Cadmium Telluride solar cell would be two orders of magnitude thinner than that.
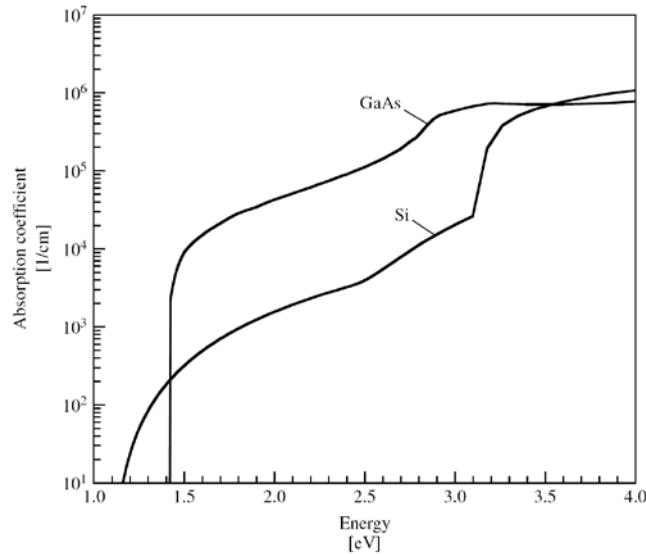
Figure 1.4. The absorption coefficient of crystalline silicon (indirect gap) and GaAs (direct bandgap) as a function of wavelength, showing that thick Si layers are needed for good light absorption [5]

Laymen invariably express surprise that silicon supply shortages are a dominant concern for crystalline silicon cells [6]. Silicon is the second most abundant element, after oxygen, in the Earth's crust, comprising 27.7% by weight. However, the issue is not merely procuring silicon in any form, but converting silicon into a single crystal in a factory. Further, crystalline silicon has a greater value when used in with in the traditional semiconductor market (such as making CPUs) than in making solar panels; also, the former market had historically been larger. Thus, the silicon supply problem is economic rather than fundamental.

1.2.3.2 Concentrator Cells

Concentrator cells use, as their name implies, sunlight that has been focused or concentrated through the use of lenses or mirrors. The obvious advantage of this is that

fewer cells are needed to take advantage of sunlight distributed over a large area. A less obvious advantage is that concentrating light enhances cell efficiency. This is due to short circuit current being linearly dependent on illumination, while open circuit voltage is logarithmically dependent. The linear dependence of the illumination would result in increased power output, but in terms of efficiency that would proportionally cancel with the increased input power resulting in no net efficiency gain. However, the open circuit voltage increase with increasing light intensity means there is an efficiency gain increase order of Log(I). This is a slowly increasing function (and the real increase eventually saturates when the open circuit voltage approaches the bandgap of the absorber material), but when the concentration is on the order of several hundred times, there can be a significant effect. Fill factor also increases with concentration. The world-record solar cell efficiency is held by a concentrator cell. The efficiency is 41.1%[7] .

Concentrator cells are, like crystalline silicon, made of single crystals. However, while crystalline silicon is made from sliced ingots drawn from a crucible, concentrator cells are grown using molecular beam epitaxy. Essentially, the atomic layers of the crystal are deposited one at a time. This is a slow and expensive process.

1.2.3.3 Multi-junction Cells

A material with a smaller bandgap will absorb more light, but will lose excess photon energy to heat. A material with a single bandgap, therefore, must be a compromise between those two effects. Another possibility is to use multiple materials with different bandgaps. This allows splitting the solar spectrum. The shorter wavelength region of the spectrum may first be absorbed by a material with a large

bandgap, producing a large voltage, and then the remaining light may be absorbed by a material with a smaller bandgap, producing a smaller voltage. In principle (and practice), it is possible to have many junctions, not just two, but it is easier to describe in the case of two.

There are two main ways of using multi-junction cells. In monolithically stacked cells, the two cells are part of the same structure, deposited sequentially, and only two wires lead from the device. The two cells are in series and therefore must produce the same current (this is called current matching). A more complete (after all, a battery and resistor in series will have the same current flow through both, but the current produced in them is not the same) but complex explanation is that in operation, solar cells are reverse biased diodes in parallel with current sources; the current sources freely transmit as much current as they generate, but no excess current may flow backwards through the diode. Because the two cells must have equal current, their current is about half that of a single cell. But the voltages of the two cells add, so the voltage is about twice that of a single cell. By proper choice of two bandgaps, the two effects do not cancel out but make a cell somewhat better than a single junction cell. Additional junctions can improve performance further.

Consider the AM1.5 solar spectrum as shown in Figure 1.5. The solar spectrum is often graphed with wavelength on the x axis and power density per wavelength on the y axis; this is done to emphasize the similarity between the solar spectrum and a black body at 5800K. The deviations from a black body spectrum are due to atmospheric effects, such as water absorption. However, for solar considerations, it is more intuitive to graph the spectrum with photon energy on the x axis and photon flux on the y axis. We are

graphing flux in the unusual units of amperes per electron rather than number per second since with the former units, integration of the spectrum directly leads to expected current density produced by a solar cell in units of A/m^2.
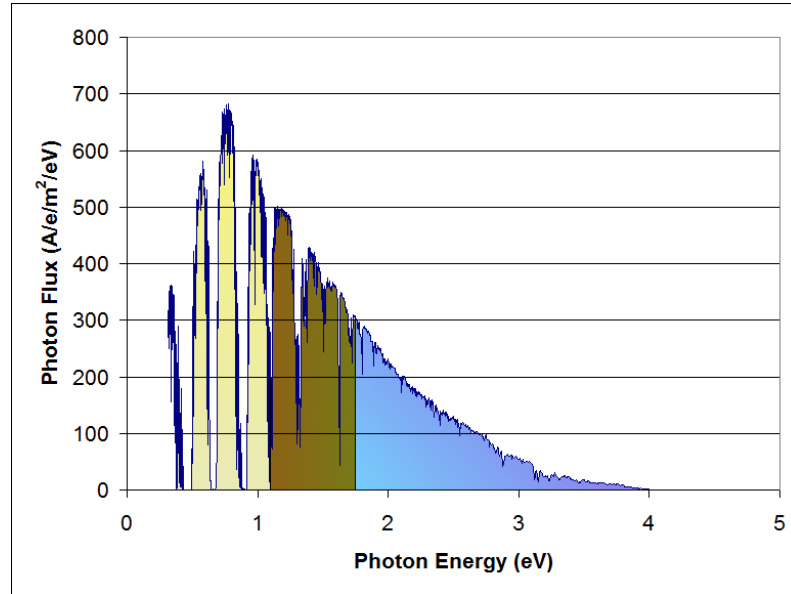
Figure 1.5. The AM1.5 solar spectrum. Suppose a double junction device had absorbers with bandgaps equal to 1.75 and 1.1eV. Photons with energy greater than 1.75eV will be absorbed by the top cell (right region), photons with energy between 1.75 and 1.1eV will be absorbed by the bottom cell (middle region) and photons with energy less than 1.1eV will not be absorbed at all (left region). For current matching, the middle and right regions must have equal areas. (Graph based on data taken from [8])

Suppose we had a monolithically stacked device whose top cell has an absorber bandgap of 1.75eV, and whose bottom cell absorber has a bandgap of 1.1eV. Photons with energy greater than 1.75eV will be absorbed by the top cell, and the top cell should have a large voltage (near but somewhat less than the bandgap of 1.75V). These photons are represented by the far right area under the curve in Figure 1.5. Photons with energy between 1.1eV and 1.75eV will be absorbed by the lower cell, and the lower cell will produce a lesser voltage (near but somewhat less than the bandgap of 1.1eV). These

photons are represented by the middle area under the curve in Figure 1.5. Photons with

energy less than 1.1eV will simply not be utilized by the device at all. These photons are

represented by the area in left under the curve in Figure 1.5. For the current matching

condition to be met, the areas of the middle and right sections under the curve must be

equal. We can estimate by eye that they approximately are equal in this case.

An alternative to monolithically stacked cells is to have two separate cells that are

simply mechanically stacked on each other, with four wires leading out (it is also possible

to use three wires). The difficulty with this situation is that the top cell must be

transparent to long wavelength light; transparent top and bottom electrodes must be used.

Metal grids may be used for current collection, but may produce shadows on the bottom

cell. Two separate production lines will need to be used. This approach has advantages,

however. For example, the two cells may be optimized separately. If the top cell is

already "good", the bottom cell can only add to the performance of the total stack. Also,

there is no need for current matching.

CdS/CdTe technology could be used to create multi-junction cells, by alloying the

CdTe with different materials to adjust the bandgap. Efficiencies as high as 25% are not

just theoretically predicted but are strongly argued to be feasible[9]. However, to date,

no multi-junction device based on CdTe has exceeded record single junction performance

of a CdTe cell.

1.2.3.4 CIGS Cells

CIGS cells are also referred to as chalcogenide cells. The chalcogens are elements

in the periodic table in the row of and under oxygen: sulfur, selenium, tellurium and

polonium. Accordingly, the "S" in CIGS stands for either sulfur or selenium, though selenium is more common. The remaining elements are copper, indium, and gallium. The chemical formula is then (in the case of selenium) $CuIn_{1-X}Ga_XSe_2$.

A strength of CIGS cells is in the flexibility to vary the components. The bandgap can vary from 1.0 eV for pure CIS to 1.7 eV for pure CGS. By varying the bandgap throughout the cell (so called bandgap grading), it is possible to reap advantages of small and large bandgaps. You would of course not want to have the small bandgap near the sun-side of the device, as then more light would be absorbed there before reaching the large bandgap material, making the latter redundant. Therefore, bandgaps are graded so that the large bandgap material is on the sun side. This is achieved by using different stages in the deposition process. The sophistication of this process has resulted in CIGS achieving the highest laboratory efficiency of any thin film photovoltaic device, 19.9%[10]. The disadvantage of this is that this causes the deposition to be relatively complicated and poorly suited for industrial mass production.

Another disadvantage of CIGS is that indium is rare and expensive.

1.2.3.5 Amorphous Silicon

Amorphous silicon has a structure that locally resembles crystalline silicon, but has random variations that disrupt any long range order. Consequently, there can be no long range structural anisotropy (or, there is so much anisotropy, but it is in all directions and random, so over large scales it averages out). This causes amorphous silicon to be effectively a direct bandgap semiconductor. It therefore can be made thinner than

crystalline silicon, with layers having thickness on the order of microns rather than hundreds of microns.

Amorphous silicon can also be produced more cheaply than crystalline silicon. Rather than growing large bulk perfect crystals at high temperature, amorphous silicon can be grown at low temperature as a thin film from a gas precursor, SiH_4.

The amorphous structure has many defects which can serve as charge carriers recombination centers and reduce efficiency. A perfectly bonded silicon atom should have four nearest neighbors, but due to the random amorphous structure, some silicon atoms might not be bonded with four others. These dangling bonds can be ameliorated by introducing hydrogen into the structure. Hydrogen is small enough to fit where a silicon atom might not be able to, and since it forms exactly one bond, it will complete the dangling bond while adding no dangling bonds of its own. Adding hydrogen is not a perfect solution. During operation, photons from sunlight can provide enough energy to split the hydrogen-silicon bond. This causes amorphous silicon solar cells to degrade 10-20% below their initial efficiency over time, a phenomenon known as the Staebler-Wronski effect[11].

1.2.3.6 Cadmium Telluride

As more detail was given to solar energy than other forms of renewables, so will more detail be given to cadmium telluride, as it has greater bearing on the subject of this thesis.

Cadmium telluride is a semiconductor with a bandgap of 1.5 electron volts. Figure 1.6 shows the predicted theoretical maximum efficiency of a solar cell as a

function of absorber bandgap when illuminated with AM1.5 light[12]. There is a fairly

broad peak from about 1.1 to 1.5 eV, making CdTe a good match for the solar spectrum.
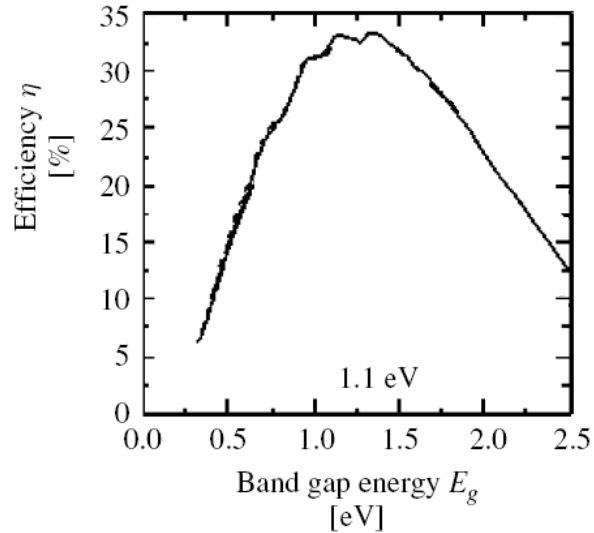
Figure 1.6. Maximum theoretical efficiency for a single absorber solar
cell as a function of bandgap, the Shockley-Queisser limit[12].

CdTe is natively doped p-type due to a relative excess of Te. It is typically used

with CdS, which is natively doped n-type due to a relative deficiency of S, as a

heterojunction partner. CdS has a bandgap of 2.4 eV, and so acts as a window layer in

cells. The need for CdS is not well understood. It, on the face, in fact seems to be a

liability: It absorbs some blue light, but this absorbed light does not contribute to the

current. Even this phenomenon is not completely understood. It could be due to a large

defect density in CdS, resulting in generated carriers simply recombining. An alternative

explanation is that the field within the CdS could even point the "wrong" way[13] – that

is, the field could point in the direction from the CdTe towards the CdS, contrary to the

expected built-in field direction (and the direction of the field in the CdTe) in a diode,

which points from the n-type side to the p-type side. Consequently, the best CdTe/CdS

cells use as little CdS as possible to obtain maximum current. However, eliminating CdS

entirely has not been successful. Cells made in our laboratory with no CdS may have

efficiencies of 6% while similarly produced cells with CdS may have efficiencies of 13%.

An important step in fabricated CdTe/CdS cells is a high temperature (near

400°C) treatment in $CdCl_2$ vapors. This treatment encourages diffusion between the CdS

and CdTe layers. There is a miscibility gap in the $CdTe_xS_{1-x}$ phase diagram.   See Figure

1.7. However, while there is not complete interdiffusion, there is a tellurium-rich phase

with some sulfur, and a sulfur-rich phase with some tellurium. This interdiffusion

extends the cells' gainful absorption of blue light, by thinning the CdS layer, and also

extends the red absorption, by lowering the bandgap of the CdTe, through band bowing,

by alloying with sulfur. There is also a lattice mismatch match between CdS (lattice

constant=0.583nm) and CdTe (lattice constant=0.648nm); alloying and intermixing

reduces the strain at the interface and improves carrier transport there.
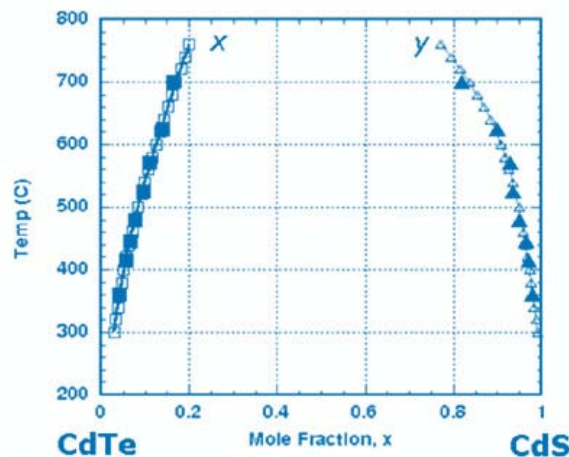
Figure 1.7. Phase diagram of $CdTe_XS_{1-X}$, showing a miscibility
gap.[14]

Copper plays an important role in CdTe cells. As shown in Figure 1.9, CdTe has a high electron affinity (the distance from the vacuum to the Fermi level) (5.6 eV) which makes forming an ohmic (or nearly ohmic) back contact difficult. A non-ohmic back contact will reduce efficiency and in extreme cases can result in "roll over" in the first quadrant (see Figure 1.8). Typically high work function metals are used. Gold is commonly used for CdTe contacts in research laboratories. Other common materials are zinc telluride, molybdenum, or graphite. Platinum also seems to have a work function that would make a good match. However, no material has been found that gives a perfect ohmic contact. To improve the contact, copper is deposited as part of the back contact of the CdTe cell and is then diffused. It is believed that the copper dopes the CdTe more heavily p-type and lowers the width of the energy barrier between the CdTe and the metal contact (see Figure 1.9). This benefit has a price. Copper atoms can diffuse in the cell, particularly under operating conditions, away from the back contact, reducing its original effectiveness.
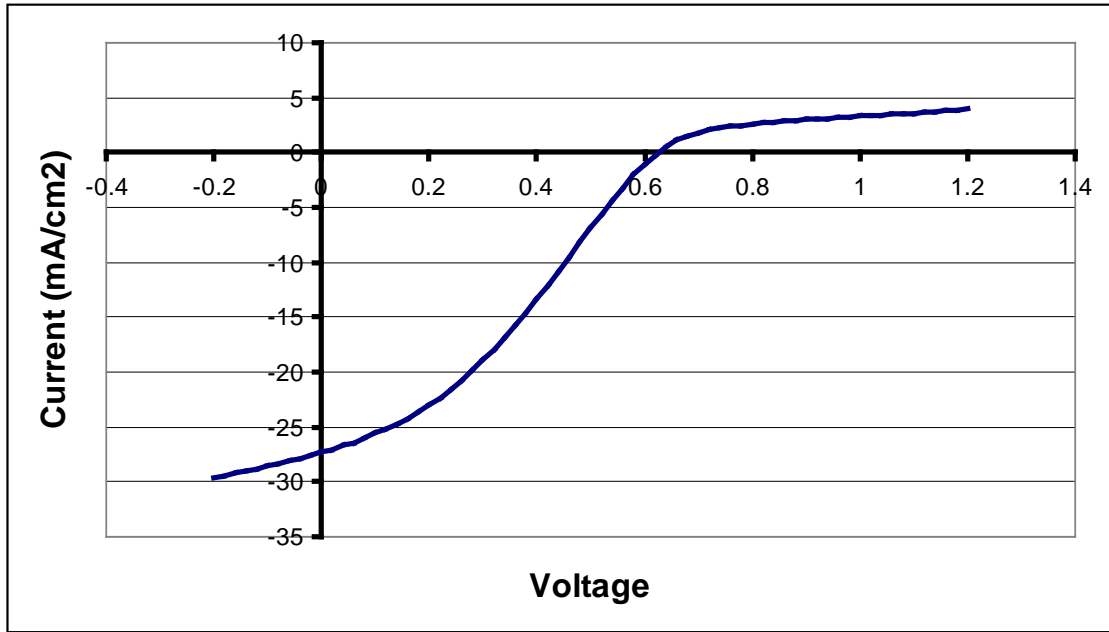
Figure 1.8. The current-voltage characteristics of a CdTe cell made on molybdenum foil. The non-ohmic nature of the back contact is manifested in "roll over" – the curve's horizontal bent in the first quadrant.[15]
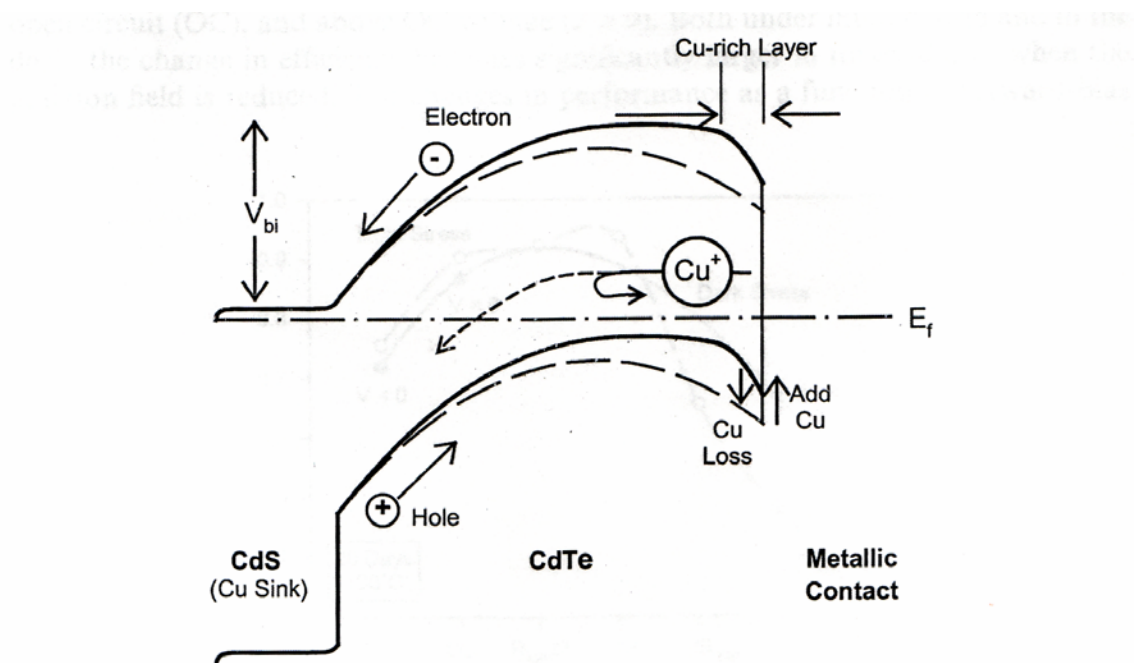
Figure 1.9. The effect of copper in CdTe cells. Copper alloying raises the valence band towards the Fermi level, decreasing the width of the barrier between the CdTe and the back metallic contact.[16]

The world record best CdTe cell is 16.5%[17]. It was fabricated by NREL in 2001. The high efficiency is attributed to a high temperature (near 600°C) growth on borosilicate glass and a novel transparent conducting oxide and buffer layer, cadmium and zinc stannates (Cd_2SnO_4 and Zn_2SnO_4), respectively, which allow high current while reducing shunting losses. Although CdTe is a better theoretical match to the solar spectrum than CIGS with a bandgap of 1.1eV, such CIGS cells have been made with 19.9% efficiency. The greatest difference between the record CdTe cell and an ideal one is in the open-circuit voltage[18]. The open-circuit voltage is related to the bandgap of the material by

$$V_{oc} = \frac{E_g}{q} - \frac{kT}{q} \ln\left(\frac{q^2 N_v p v_r^2}{J_L^2}\right)$$

with E_g the bandgap, N_v the density of states in the valence band, p the density of holes, J_L the light induced current and v_r the surface recombination velocity. CdTe cells have an unusually high surface recombination velocity which results in a unusually large E_g/q-V_{oc}. It is 0.65 V in the case of CdTe. For comparison, for the best CIGS and monocrystalline silicon cells, this measure is about 0.4V. Despite deviations from ideality, it is believed that a 19% CdTe cell could be feasible. If fact, if E_g/q-V_{OC} was reduced to 0.4V, with all other parameters of the record CdTe cell unchanged, a 21.3% cell would result.

Cadmium is a toxic material and a carcinogen. It is therefore understandable that people might have concerns about the environmental impact of producing CdTe solar panels. However, cadmium is already present in other consumer products, such as NiCd

batteries. A square meter CdTe PV module has less cadmium than a C-size Ni-Cd

battery[19]. Cadmium is also produced as an unavoidable product of mining. Studies

have shown that more cadmium is released into the atmosphere by coal power plants than

by CdTe photovoltaic module manufacturing plants[20]. It therefore may well be the

case that the safest way of dealing with cadmium is by bonding it with tellurium and

sealing it in a solar panel!

1.3 Flexible CdS/CdTe Solar Cells

Solar cells deposited on glass are, of course, rigid. Solar cells deposited on

plastics (polymers), however, may be thin and flexible. See Figure 1.10. There are

several reasons for fabricating flexible cells.
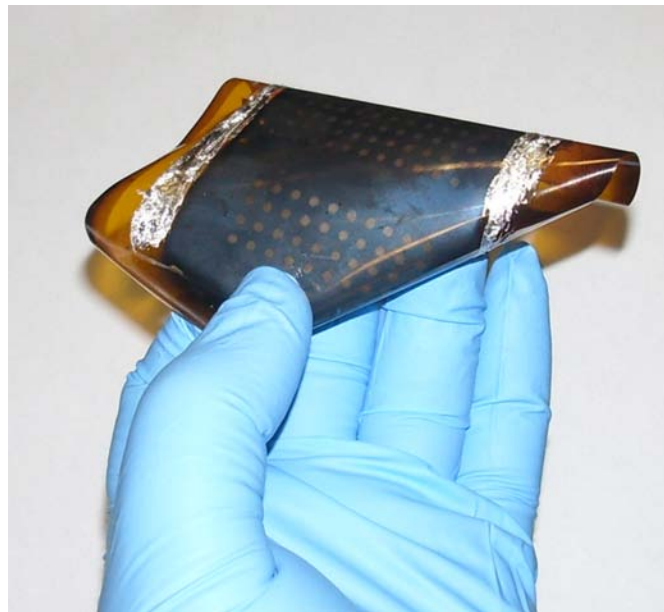
Figure 1.10. A CdS/CdTe device made on polymer in our
laboratory.   The gray coating is CdTe; the gold dots are for
contacting individual cells. The device really is flexible!

1.3.1 Motivation for Flexible Solar Cells

Thin polymer substrates lead to high specific powers – that is, power generated per mass of the cell. A 10% cell on 3mm glass would generate 14W/kg, while a 10% cell on 12.5μm polyimide (a type of polymer) would generate 5600 W/kg. This would be important in any situation for which weight is important, from consumer electronics, such as solar cells in a backpack to charge cell phones or MP3 players, to military use. Marines may already carry 70 pounds of gear.

By virtue of being flexible, such cells could be mounted on surfaces that are not necessarily flat.

Continuous sheets of polymers may be run through deposition equipment in a "roll-to-roll" process. This would be useful for industry. Automated manufacturing of solar cells on glass, on the other hand, may require robots to place the glass on the assembly line.

1.3.2 Substrates Suitable for Flexible CdTe

A selection of plastics and their glass transition temperatures are listed in Table 1. Considering that CdTe solar cells require a chloride treatment near 400°C, of those listed, only polyimides are suitable for a substrate.

Plastic	Glass Temperature
PET (Polyethylene terephthalate)	75°C
PVC (Polyvinyl chloride)	82°C
PLA (Polylactic acid)	50-80°C
Polyimide	>400°C
Polycarbonate	150°C
Polystyrene	95°C

Table 1.1 A selection of plastics and their glass temperatures. Of those listed, only polyimide is suitable for use as a CdS/CdTe substrate. (compiled from [21])

1.3.3 Review of Prior Art

Pioneering work in flexible CdTe cells was done by Tiwari et al.[22]. They used evaporation methods to deposit the semiconductor layers. They originally used zinc oxide as a transparent top contact. The polyimide used was not commercially available but was fabricated by them (using spin coating). A thin lift off layer of sodium chloride (NaCl) was evaporated onto glass, and the polyimide was coated over the NaCl. The polyimide was adhered thusly to glass throughout the deposition process. Afterwards, the NaCl was dissolved in water to remove the polyimide and obtain a free standing flexible solar device. They achieved 8.6% efficiency with this procedure. Figure 1.11 shows a current-voltage (JV) curve of this cell.
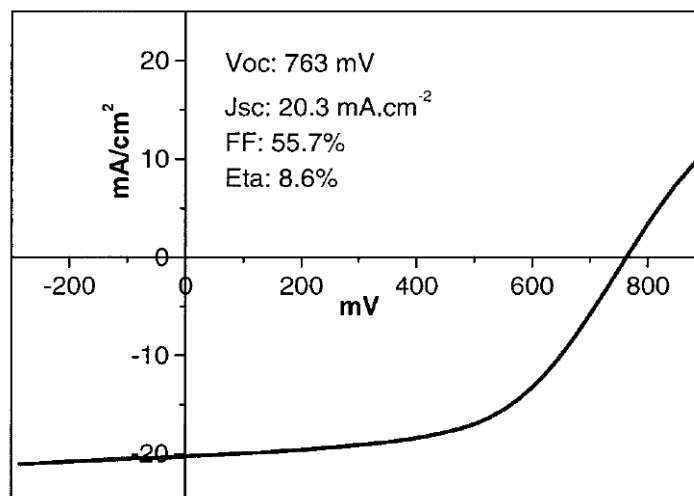
Figure 1.11. The best flexible cell fabricated by Tiwari et al. using AZO as a TCO.[23]

Near the end of their paper, they state, "To understand the reasons for lower efficiency of CdTe solar cells on ZnO:Al/polyimide, it is important to mention that the ZnO:Al, despite its good opto-electronic properties, does not yield efficient CdTe/CdS solar cells. Earlier we have reported that solar cells on ZnO:Al-coated glass substrated exhibit … a very low fill factor … and high series resistance."

In later work, they therefore eventually moved to using indium tin oxide (ITO) as their front transparent contact. They also used a thin (~10μm) commercial polymer (Upilex) as well as their in-house polymer. They found that a 450°C anneal in air of the polyimide/ITO stack slightly increased the sheet resistance of the ITO, but led to greater stability during processing. With ITO, they achieved 11% using their in-house polymer and 11.4% efficiency with Upilex[23].

27

1.3.4 Review of Our Work and Thesis Overview

We have grown flexible CdTe solar cells using sputtering. Sputtering is a relatively low temperature deposition technique; our substrates generally do not go above 300°C during growth processes. This makes sputtering suitable for work with polyimide substrates, which are stable at temperatures near or over 400°C. As sputtering as a deposition technique is a distinction of our work in comparison to work done by Tiwari's group, we in Chapter 2 review the technique of sputtering and describe our deposition systems.

JV data of an early flexible cell we had made is shown in Figure 1.12. Although the cell functions (efficiency is 1.4%), performance is very low, and the JV curve does not even display rectifying (diode-like) behavior.
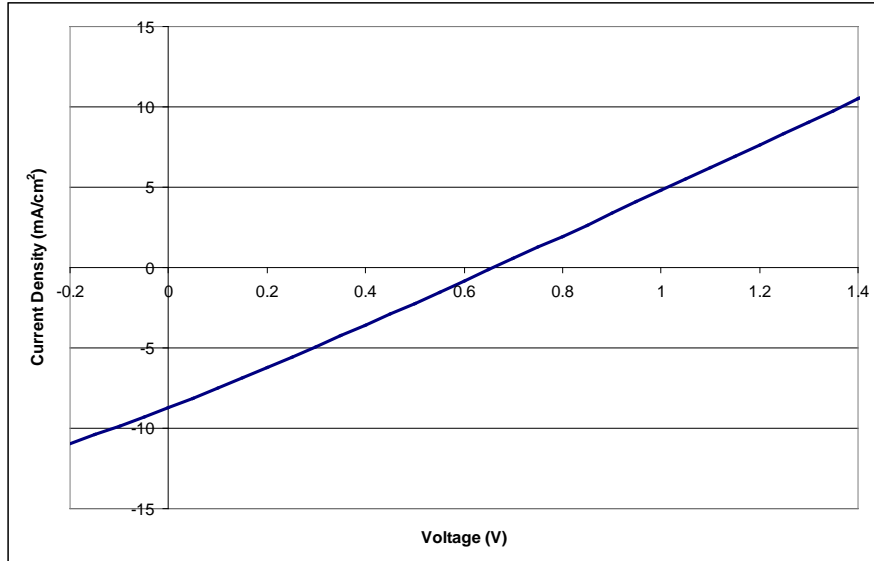
Figure 1.12 JV data of an early flexible cell of ours.

After initial difficulties, we decided that making flexible cells might not merely be a mechanical task but might raise issues requiring physical understanding.

One simple difficulty is that the JV curve as shown in Figure 1.12 is not amenable to typical JV curve analysis (eg., that the inverse of the slope of the curve in reverse bias is approximately the shunt resistance) because such analysis assumes at a minimum that the cell is performing reasonably enough to at least show rectifying behavior. Therefore, in Chapter 3 we first review JV curves and their typical interpretations, and in Section 3.6 derive a simple model for very poor cells, as in Figure 1.12, which allows for easy analysis.

Such analysis reveals that the cell in Figure 1.12 has large losses due to both shunting and series resistance. A large series resistance loss might be mystifying since our TCO layer was deposited to have sheet resistance near 15 ohms/square, equivalent to commercial Pilkington Tec15, which we have used to deposit high efficiency (~13%) cells on glass. Often it is assumed in the laboratory that if TCO sheet resistance is "good enough" that series resistance losses will be low. In Chapter 4, we present calculations that relate sheet resistance to series resistance for cells in a geometry that we typically use in our laboratory, and confirm those calculations with experiment.

Shunting issues are often addressed with a highly resistive and transparent (HRT) buffer layer, but in our opinion optimal HRT parameters have typically been considered purely a matter of experiment, and even attempts to explain their function might rely on complex, opaque techniques (eg., finite element simulation on a computer). We therefore present calculations on expected results of using an HRT in Chapter 5.

Tiwari had mentioned difficulties with using ZnO as a TCO. The ZnO layer is very important, and is discussed in Chapter 6. We first discuss basic properties, such as its resistivity and optical transparency. ZnO is also used for HRT films, which we have

grown using both doped and undoped ZnO targets. We report the properties of these

films as a function of oxygen in the sputter gas. Another important ZnO issue is stability

during processing. We have observed a change in ZnO sheet resistance after $CdCl_2$

treatment. We studied this change systematically as a function of ZnO thickness.

Chapter 7 traces the progress of our flexible cells. Much of our progress was due

to understanding series and shunt resistance losses, ZnO issues, and incorporation of

HRT layers in our cell design. Other issues which led to cell improvement include $CdCl_2$

optimization.

Through working through various challenges and understanding further issues, the

efficiency of our flexible cells improved. Ultimately, we have fabricated a 10.5%

flexible CdTe cell. JV data of this cell is shown in Figure 1.13.
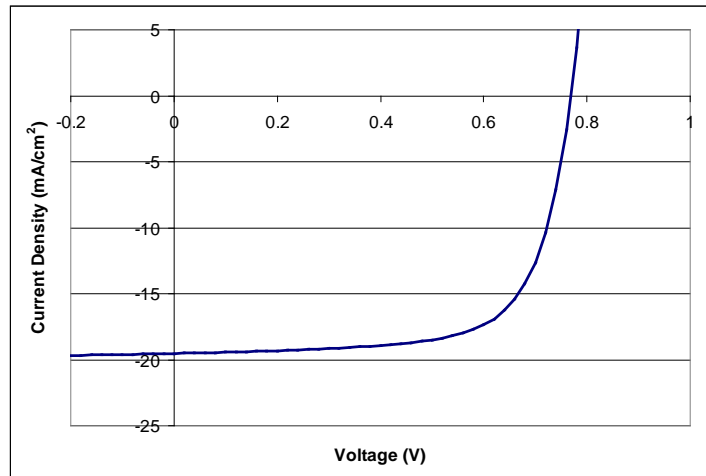
Figure 1.13. JV data of our best flexible cell. Efficiency=10.5%

This 10.5% cell is in fact of higher efficiency than the 8.6% best AZO cell

fabricated by Tiwari's group. In comparison to their cell, we note that ours has lower

series resistance (which can be confirmed simply by looking at the JV curves) and higher

fill factor. We therefore speculate that our improved performance could be attributed to the discovery and characterization of AZO's sheet resistance change with $CdCl_2$ treatment as well as detailed understanding of the effect of series resistance.

Their 11.4% cell with an ITO contact still has higher efficiency, but we believe improved performance with an AZO contact is significant. Due to the rarity of indium, zinc oxide is less expensive than indium tin oxide and thus may be more suitable for large scale manufacturing. Zinc oxide is also nontoxic (it is in fact an ingredient in Gold Bond Medicated Powder and in some sunblocks).

Ultimately, through identifying and understanding issues presented in this thesis, we have achieved good efficiency for flexible ZnO/CdS/CdTe solar cells.

Chapter 2 -- Experimental Procedures and Sputtering

2.1. Introduction

Various techniques may be used to deposit the semiconductor layers of which a solar cell is composed.   Among them:

Molecular beam epitaxy, in which atoms are deposited in ultra high vacuum slowly on a single crystal so the deposited atoms grow as a single crystal;

Pulsed laser depositon, in which the material to be deposited is ablated by a focused laser, then the ablated material condenses on a substrate;

Chemical vapor deposition, in which volatile precursors in a vapor state react and condense as a nonvolatile film on a substrate; chemical dissociation may be enhanced with a plasma;

Thermal evaporation, in which the material to deposited is heated to raise its vapor pressure, described in more detail below;

Electron beam evaporation, similar to thermal evaporation, but instead of equilibrium heating of the to-be-deposited material, it is heated locally with an electron beam;

Closed space sublimation, also similar to thermal evaporation, but the close proximity of the deposited material and the substrate means the vapor pressure needed for useful deposition need not be so high;

32

Electrodeposition, in which ions in solution are attracted to a substrate, where the film grows, by applying a voltage, similar to the well-known process of electroplating;

Vapor Transport Deposition, a high-speed technique, done at high temperature, in which carrier gasses are saturated with elements of the compound to be deposited, which condense on a colder substrate; further distinguished from closed space sublimation because the source and substrate need not be close;

Chemical Bath Deposition, a process by which a substrate is placed in a solution of chemicals; chemical reactions produce the desired material, which coat everything in the solution.

The solar cell layers described in this thesis were deposited with only two techniques: Thermal evaporation and sputtering. The metal back contacts are deposited with thermal evaporation while the semiconductor layers are all sputtered.

2.2 Thermal Evaporation

Thermal evaporation is perhaps the simplest deposition technique. It can be considered in complex terms – phase diagrams may need to be consulted when different sources of different elements are co-evaporated, as in copper indium gallium diselenide (CIGS) cells. One could also consider the growth modes of the developing film. However, it is essentially, and in our application, simplicity itself. A large current (in our case, of about 200 Amperes) is passed through a refractory metal (in our case, tantalum) "boat" which holds the material to be deposited. Joule heating raises the temperature of

the boat, and the increase in temperature in turn raises the vapor pressure of (and

generally melts) the to-be-deposited material.

Thermal evaporation must be performed in high vacuum. Our system is pumped

with a diffusion pump with a liquid nitrogen trap, which prevents backstreaming of the

hot diffusion pump oil (that is, it causes the oil to cool, condense and fall back into the

diffusion pump, rather than rise into and contaminate the deposition chamber). The base

pressure is typically on the order of $1x10^{-5}$ Torr. High vacuum is needed both to prevent

contamination and to allow a long mean free path so evaporated atoms can reach the

substrate.

Photographs of our evaporation system are shown in Figures 2.1 to 2.4.

Figure 2.1. The system for thermally evaporating the copper-gold back contacts for
the cells described in this thesis. When in operation, the bell jar is closed, as shown.
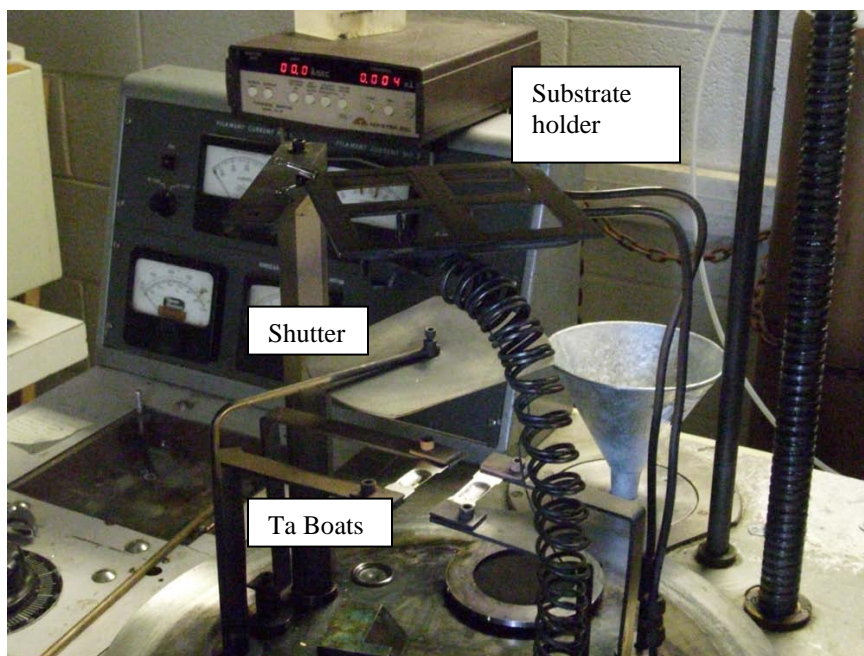
Figure 2.2. The interior of the copper-gold evaporation bell jar chamber. Liquid nitrogen is added for the cold trap with the funnel.

Figure 2.3. Detail of the tantalum boats, holding gold (left) and copper (right). The shutter (in the open position) is visible in the upper left corner.

Figure 2.4. The quartz thickness monitor, below the substrate holder. The view is from below, near the boats, looking up. Gold from many depositions visibly coats the equipment.

2.3 The Quartz Crystal Thickness Monitor

A quartz crystal microbalance is used as a thickness monitor to control the amount of material deposited. We will describe the physical principles of this instrument.

Quartz is a piezoelectric material; it deforms upon application of a voltage. If an alternating current is applied, it will oscillate.

As shown in Figure 2.5 from Sauerbrey's original paper on quartz thickness monitors, the quartz crystal oscillates in the mode of a shear wave. Therefore, we will consider the physics of shear.
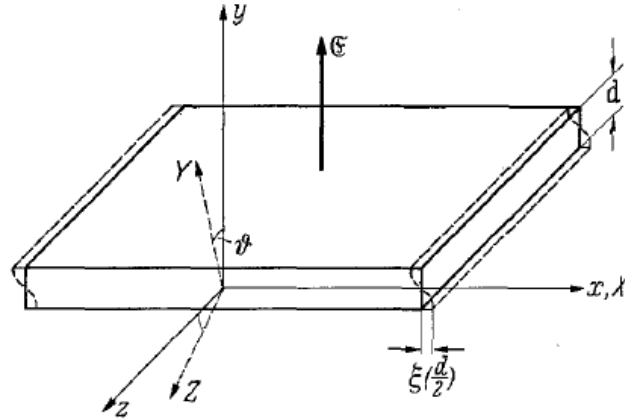
Figure 2.5. A shear wave in a quartz thickness monitor.[24]

Shear strain is of the sort shown in Figure 2.6.
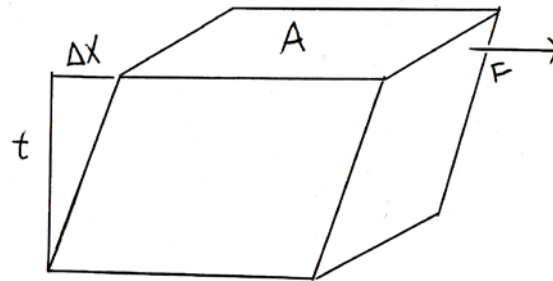
Figure 2.6. An object experiencing a shear strain

A force is applied at and parallel to the top face of the material. The bottom of the material could be assumed to be held stationary. Rather than elongating, as in tensile strain, the material is deflected. The stress is defined as $\Delta x/t$. As in Hooke's law, stress is proportional to strain, defining the Shear Modulus, G:

$$\frac{F}{A} = G\frac{\Delta x}{t}$$

[2.1]

Let us consider an infinitesimal thickness element in a crystal experiencing shear. The situation is as shown in Figure 2.7.

37
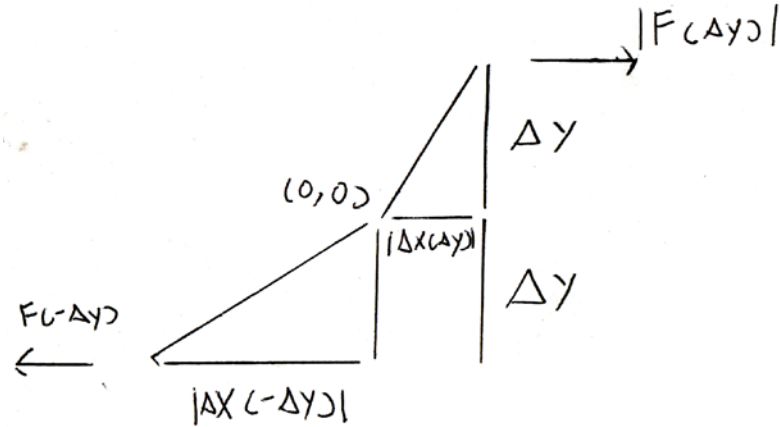
Figure 2.7. Side view of an infinitesimal element in a shear wave.

We want to describe how shear affects the location labeled in the image as the origin (though it could be any arbitrary location in the crystal). The y-axis is the independent variable axis while x is the dependent variable axis. At a position Δy above the origin, a force $F(\Delta y)$ is applied, resulting in deformation $\Delta x(\Delta y)$. By the definition of the shear modulus, we have

$$\frac{F(\Delta y)}{A} = G\frac{\Delta x(\Delta y)}{\Delta y}.$$

[2.2]

We can similarly consider the bottom triangle. As drawn, but with no loss of generality, F is in the negative x direction, as is Δx. Therefore,

$$\frac{-F(-\Delta y)}{A} = G\frac{-\Delta x(-\Delta y)}{\Delta y}.$$

[2.3]

Adding both equations and multiplying by A gives

$$F(\Delta y) - F(-\Delta y) = GA\frac{\Delta x(\Delta y) - \Delta x(-\Delta y)}{\Delta y} = GA\frac{\Delta^2 x}{\Delta y}.$$

[2.4]

As Δy tends to zero, the left side of the equation becomes the *net* force acting at

the given point. We can write that as $m\dfrac{d^2x}{dt^2}$. The mass is equal to $\rho A\Delta y$, with ρ the

density of the material. Making those substitutions, dividing by the mass, and finally

taking the limit as Δy tends to zero gives

$$\frac{\partial^2 x}{\partial t^2} = \frac{G}{\rho}\frac{\Delta^2 x}{\Delta y^2} = \frac{G}{\rho}\frac{\partial^2 x}{\partial y^2}. \tag{2.5}$$

This is a wave equation describing a wave of velocity $v = \sqrt{\dfrac{G}{\rho}}$. If the wave is a

standing wave with antinodes at the two edges of the crystal, then the first order

wavelength would be $\lambda=2t$, so the frequency would be

$$f = \frac{1}{2t}\sqrt{\frac{G}{\rho}}. \tag{2.6}$$

Therefore, the vibrational frequency of the crystal is a function of its thickness.

We find that

$$\frac{df}{dt} = -\frac{1}{2t^2}\sqrt{\frac{G}{\rho}} = -\frac{f}{t} \tag{2.7}$$

so that

$$\frac{df}{f} = -\frac{dt}{t} = -\frac{dm}{\rho A t} \tag{2.8}$$

The canonical form of the Sauerbrey equation is

$$\Delta f = -\frac{2f_o^2}{A\sqrt{\rho G}}\Delta m. \tag{2.9}$$

This is equivalent to the previous equation, as seen by solving for df/dm in each equation,

setting them equal, and dividing by f, at which point the original formula for the original

frequency may be obtained.

39

In the right side of the previous equation, everything other than Δm depends only on the original crystal parameters. The newly deposited material is treated as an extension of the quartz crystal, so it does not change ρ or G, but only enters into the equation as Δm.

This is the most involved physics of our evaporation deposition system. We now will consider the more complicated method of sputtering.

2.4 Sputtering

In sputtering, material to be deposited (which is in the form of a "target") is bombarded with high energy ions from a plasma, knocking the material free so it may travel to a substrate.

In thermal evaporation, the deposited material must have a significantly higher vapor pressure (and generally lower melting point) than the boats holding the material to prevent contamination. Due to the high melting points of tantalum and tungsten, for example, those materials would be unsuited for deposition by thermal evaporation.

Sputtering, by contrast, may be used with any material, no matter how refractory. Impinging ions may have energy on the order of 100-500 eV, which would correspond to a thermal energy of up to about 6 million Kelvin.

Another advantage of sputtering is that stoichiometry of final films can be controlled through the stoichiometry of the original target. The activated depth of sputtering (the depth of the target from which atoms may be removed at a given instant) can be as low as tenths of nanometers. If the target material is a compound (say, AB), and one element of the compound (say, A) has a higher sputter rate than the other, then

the film could become A rich. However, at the same time, the target's surface is becoming B rich. Since the B rich surface must be sputtered before the stoichiometric AB material deeper in the target is reached, stoichiometry in the growing film is maintained.

2.5 Schematics of a Typical Sputtering System

A sputter system uses a *sputter gun* which holds the *target* material and which functions as a *cathode*. The terminology is somewhat confusing as the target is *part* of the gun, contrary to colloquial usage of the words. The gun is surrounded by a ground shroud which restricts sputtering to the target material, preventing sputtering of the gun itself. The gun and the walls of the chamber are grounded; essentially, the entire rest of the system could act as an anode. More specifically, the substrate may also be grounded, it may be at a floating potential, or a specific bias may be applied. In any case, the geometrical asymmetry of the system (that the cathode is much smaller than the anode) focuses the electric field (to be described later) at the cathode so the cathode is sputtered rather than the anode. See Figure 2.8.
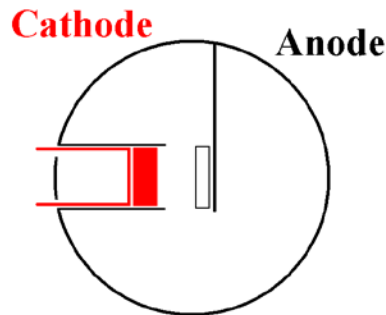
Figure 2.8. A very schematic illustration of the sputter gun (left) inside a sputter chamber. The target (red rectangle) is facing the substrate (black outlined rectangle). The substrate may be grounded (as implied here) or have some bias.

Sputtering is done at high vacuum to prevent contamination. Our systems are rough pumped with mechanical pumps into the torr range (our systems are rough pumped through the turbo pump, which is initially turned off, though it is also possible to valve a system so the roughing phase is separated from the high vacuum phase) and then is turbo pumped, with the mechanical pump backing the turbo, into high vacuum, generally in the 10^{-6} to 10^{-7} torr range. High purity argon is used as the working gas and the source of the bombarding ions. The chamber pressure during sputtering is in the millitorr range. The working pressure is an important parameter that can be used to influence film properties, which will be discussed later. Argon is used as it is inert and will not react with the depositing material. On the other hand, it is also possible to mix the argon with another gas, such as oxygen or nitrogen, to intentionally allow chemical reactions to occur. This is called, naturally enough, Reactive Sputtering. We will describe this in more detail later, as we have used reactive sputtering with zinc oxide targets.

A radio frequency (RF) power generator is used to power the plasma. The frequency used is usually 13.6 MHz. This number is chosen more due to be in compliance with Federal Communications Commission (FCC) guidelines than for any effect on the film. However, for the RF fields to couple to and power the plasma, their frequency must be below the gaseous plasma frequency. We make a unit analysis argument considering a single electron inside the plasma, subject to the Coulomb force due to the charge of the rest of the plasma. Treating that electron as a harmonic oscillator,

$$k = \frac{F}{x} = \frac{\left(\frac{eq}{4\pi\varepsilon_o d^2}\right)}{d} \sim \frac{e^2 n_e}{\varepsilon_o} \qquad [2.10]$$

Where d is some "characteristic length", so d^3 is a volume, and the total charge, q, divided by that volume is the electron density, n_e. Then simply using the frequency of a harmonic oscillator

$$f = \frac{1}{2\pi}\sqrt{\frac{k}{m}}$$
[2.11]

we derive the plasma frequency (this equation happens to be exact, though often is given in terms of circular frequency rather than actual frequency)

$$f_p = \frac{1}{2\pi}\sqrt{\frac{e^2 n_e}{m_e \varepsilon_o}}$$
[2.12]

For a typical plasma density of $10^{10}/cm^3$ (corresponding to ~10^{-5} ionization), the plasma frequency would be 3.5×10^{10} Hz. Therefore, while 13.6 MHz is not specifically chosen for its utility, it is usable.

An impedance matching network is needed to maximize power transfer to the gun. Direct Current (DC) sputtering is also possible, but requires a conducting target, such as a metal, as will be explained later. On the other hand, a matching network is not needed for DC sputtering.

A means for heating the substrate to control the temperature of the growing film is needed.

In magnetron sputtering, magnets inside the gun are used to control the plasma conditions. The magnetic properties are usually not treated as a *continuous* parameter influencing film quality, since replacing magnets inside the gun is more difficult than adjusting temperature or pressure.

These various features of a sputter deposition system are summarized in Figure 2.9. Real sputter systems used for this thesis work are shown in Figures 2.10-2.12.
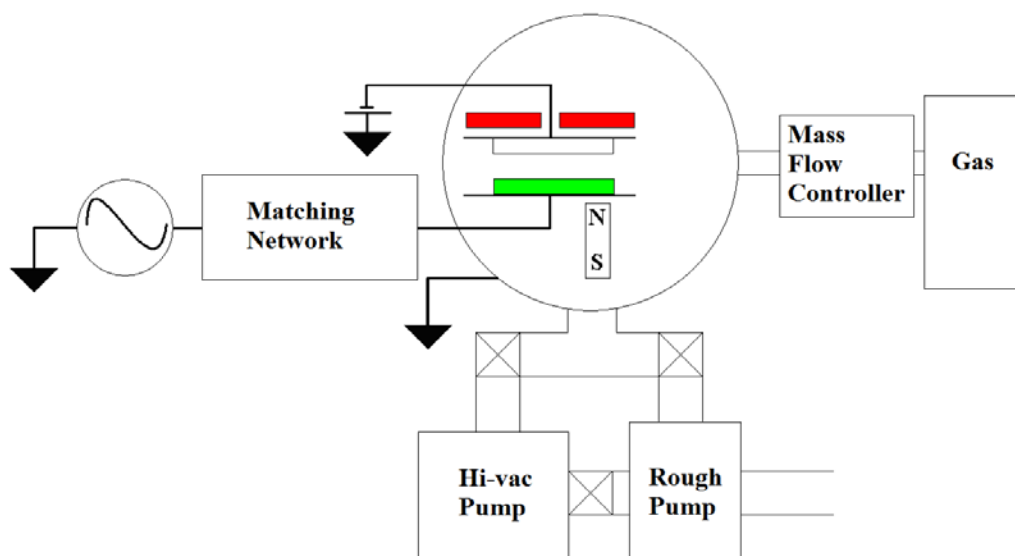
Figure 2.9. A schematic summarizing the components of a generic sputter system. The system is pumped with high vacuum and rough pumps (valved at different stages of pumping). An RF power supply, connected through a matching box, powers the gun; the target is represented as a green rectangle. The N/S rectangle under the gun represents one magnet of a set of magnets that establish the magnetic field of the magnetron. A gas is needed for the plasma. The precise flow of gas into the chamber may be controlled with a mass flow controller; this is especially important if two or more gases are used for reactive sputtering, so the ratio between them can be controlled. Heating (red rectangle) is needed to control substrate temperature. The substrate may be biased.
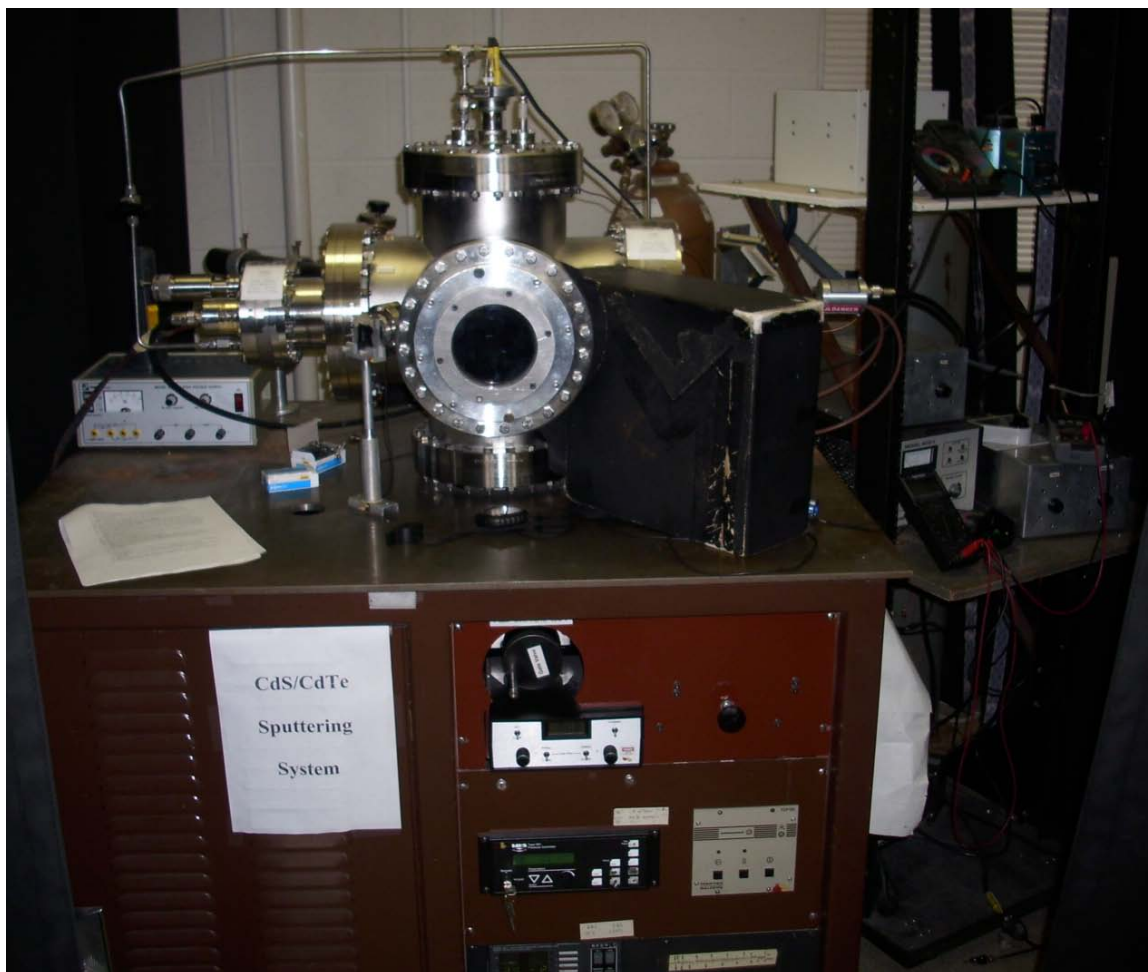
Figure 2.10. The CdS/CdTe sputter system. This system has two guns, for CdS (on the left) and CdTe (on the right) so the two layers can be deposited without breaking vacuum, by rotating the substrate. The front, bottom of the console has controls for controlling the turbo pump, vacuum gauges, and gas flow. Controls for the heater and RF power supply are on a shelf to the right.

Figure 2.11. The Zinc Oxide Chamber. Currently only one sputter gun (on the right) is installed on this system.
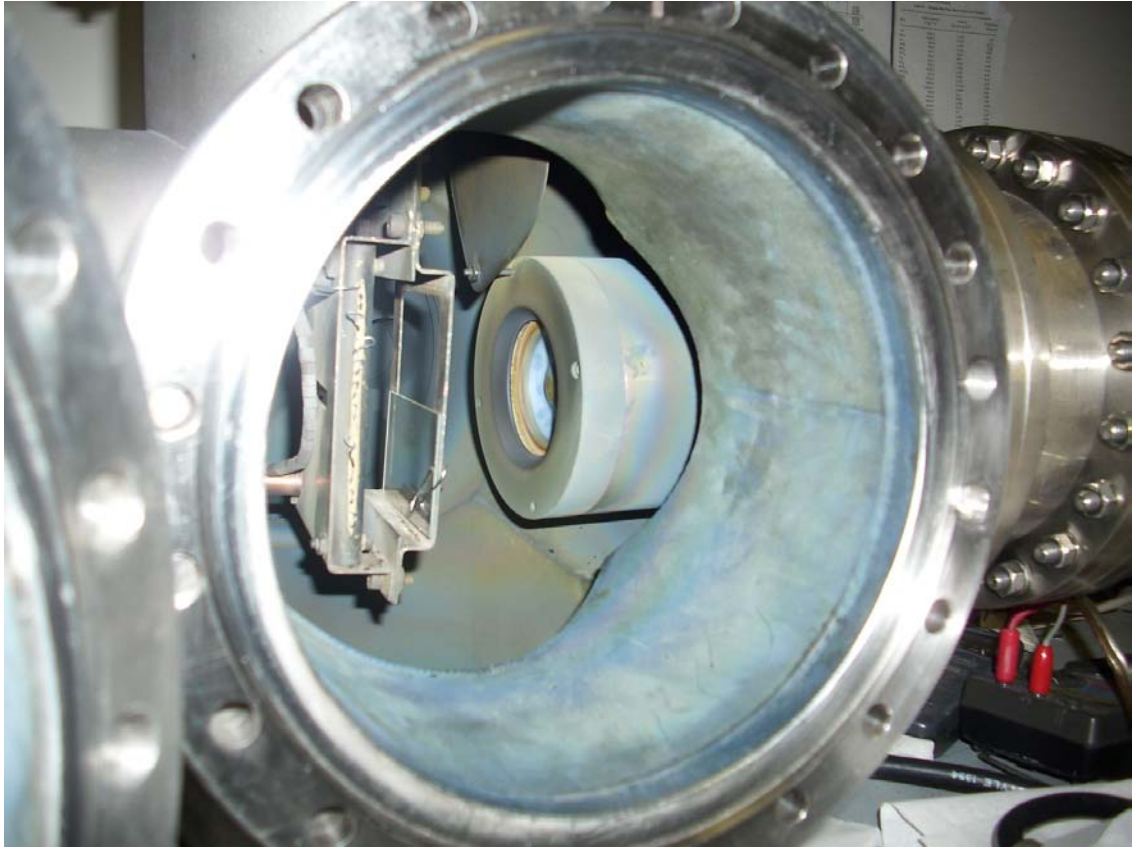
Figure 2.12. The interior of the zinc oxide system. The substrate holder is on the left; a 1.5"x3" microscope glass slide is loaded (held in place with a paperclip) as a substrate. On the back of the substrate holder is the heater element. The heater element is made of two vertical boron-nitride rods, threaded through drilled holes with tantalum wire. The boron-nitrate is normally white, but has been coated with gray material after many depositions; some white is still visible around the holes for the tantalum wire. The ground shroud is the most visible part of the gun. The target is in the middle of the gun. A shutter in front of the gun is in the up (open) position.

2.6 Physics of Sputtering

Sputtering is a plasma process. The sputter gun supplies energy and electrons to the plasma.

Electrons within the sputter gun target may be thought of as sitting in a potential well with depth equal to the work function. See Figure 2.13. With an electric field applied, the electron has a probability of leaving the target through tunneling.
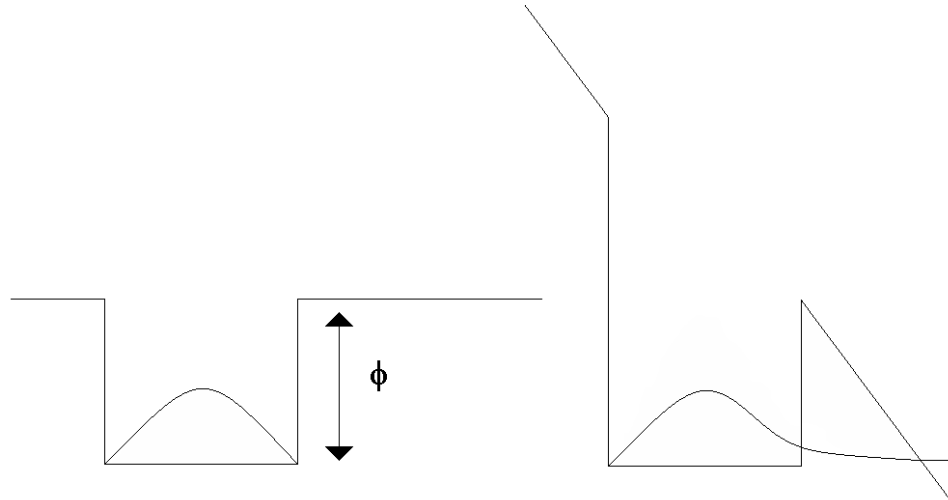
Figure 2.13. An electron wavefunction in a potential well with work function depth (left). When an electric field is applied (right), the electron has a probability of tunneling.

The current in the case of no electric field is controlled by the Richardson equation:

$$J = \left(\frac{4\pi m k_B^2 e}{h^3} \right) T^2 e^{-\frac{W}{k_B T}}$$

[2.13]

The leftmost e in that equation is the electron charge, while the rightmost e is Euler's constant. W is the work function. With estimates of the work function as 1 eV and T as 300K, we obtain a current of $5 \times 10^{-7} A/m^2$. If, during sputtering, the power supply provides a voltage difference of 1500 V, and the cathode-anode distance is estimated as 5

cm, then the electric field would be 1500V/5cm. This would "effectively" reduce the work function in Equation 2.13 by

$$\Delta W = e\sqrt{\frac{eE}{4\pi\varepsilon_o}} \sim 0.006eV << 1eV \ . \hspace{3cm} [2.14]$$

Therefore, the RF power supply does not provide sufficient voltage to maintain the plasma through thermionic emission alone. However, even the original current density, for a target size of 2 inch diameter, implies a current of $1\mathrm{x}10^{-9}$ A, or $6\mathrm{x}10^{9}$ electrons/second. These electrons are able to initiate the plasma, which is then maintained, with the field applied, by secondary ion emission.

As an electron from the cathode is accelerated towards the anode, it gains kinetic energy. As it travels to the anode, it also may collide with an argon atom. The first ionization energy of argon is 15.7 eV, so that an electron that has traveled through a potential drop of merely 15.7 V will have gained enough energy to ionize an argon atom. This process is called electron impact ionization. As stated, the source of electrons for this process could be the cathode; electrons from ionized argon atoms can also ionize further atoms.

Argon atoms that have been ionized will be accelerated towards the cathode. When they collide with the cathode, they possess energy such that they may: become implanted within the target, sputter material from the target (which may or may not be ionized), release photons, or release secondary electrons.

The term "secondary electrons" may be confusing and needs clarification. They are not secondary as compared to, say, the original electrons emitted from the cathode by field-assisted thermionic emission. Rather, secondary electron emission is a name for a specific process. As the positively charged ion approaches the target, an electron from
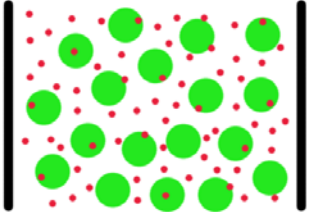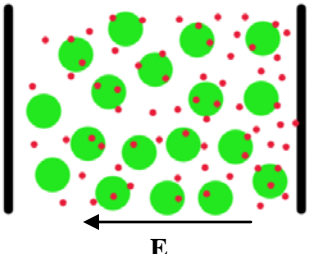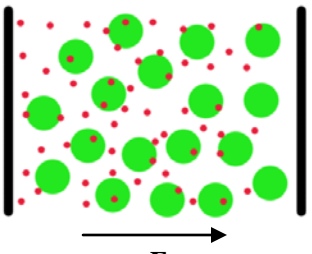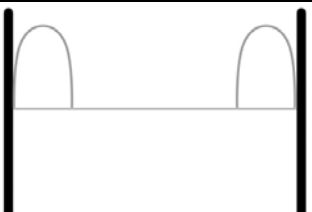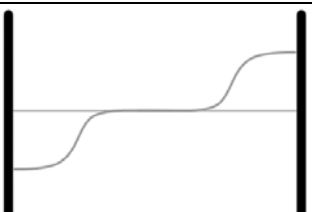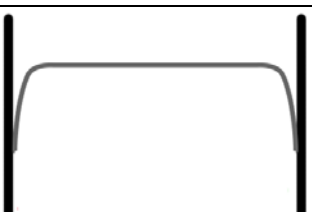
the target may tunnel into the ion to neutralize it. In the process, the electron falls from

whatever energy state it existed in inside the target, often to the lowest available state in

the ion, which is generally at a lower energetic state than the electron from the target. In

order to conserve energy, the excess energy is transferred to a different electron in the

target, which may be sufficient to reach the vacuum level. This freed electron is called

the secondary electron, explaining the meaning of the terminology. This process is

summarized in Figure 2.14. Secondary ion emission provides the current necessary to

sustain the plasma since, as explained previously, thermionic emission does not provide a

large enough current. If removed electrons in the target were not replaced, eventually

more could not be removed and the plasma would discharge. To resupply electrons in the

target with more electrons from the cathode requires the target to be conducting.

Therefore, conducting materials such as metals may be sputtered with DC sputtering. For

insulating targets, it is impossible to take a DC current from the target, and RF sputtering

must be used, essentially "reusing" electrons which already exist in the plasma.
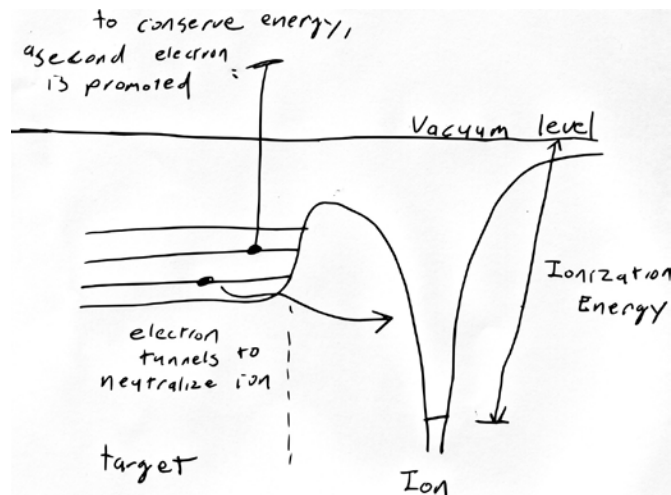
Figure 2.14. The process of secondary electron emission. An electron tunnels
from the target into the incoming ion, neutralizing it by falling to the lowest
energy stage, and to conserve energy, a second electron is promoted.

As mentioned, one asymmetry that allows sputtering to work is the difference between the geometry of the cathode and the anode. Another is the difference in mass between electrons and ions. This determines the potential of the plasma with respect to ground. Imagine if the plasma were at lower potential than the chamber walls. This would mean the plasma would act as a "basket" for positive charge, but a "hill" for negative charge. This would cause the more mobile electrons to move to walls, lowering their potential until they were at a potential lower than or equal to that of the plasma. Therefore, the opposite is true; the plasma is at a higher potential than the walls. Thinking in those terms allows one to mentally quickly determine the sign of the plasma potential by reductio ad absurdum, but it reverses the proper cause and effect order.

The cause of the sign of the plasma with respect to ground may be deduced by considering the motion of ions and electrons within one period of alternating current. In our example, we treat the situation as a simple two dimensional geometry, with the cathode and anode as symmetric, for convenience. The plasma consists of ions surrounded by free electrons (Figure 2.15a). Figures 2.15b-d explain how, as a consequence of the lighter mass of the electron, there is a net positive charge by either electrode. The electric field may be found by Gauss's Law. By symmetry, the electric field must be perpendicular to the electrodes. The Gaussian surface could be a rectangle containing the left electrode and extending a variable distance into the plasma. As the distance increases, passing through the left region of positive charge, the charge enclosed by the surface increases, and, by Gauss's law, the electric field increases as well. As the

	Figure 2.15a. A plasma in equilibrium consists of ions (green) and electrons (red). Assuming the plasma is neutral, the net charge density everywhere is zero. The plasma is contained between two electrodes, represented as two black vertical bars.
	Figure 2.15b. When the applied electric field points left, the ions will move left and the electrons will move right. The force on each is equal (assuming singly ionized atoms), but the acceleration of the electrons is much more due to their lesser mass. Therefore, a net positive charge arises on the left.
	Figure 2.15c. When the applied electric field reverses during the second half of the period, the ions drift right and the electrons left. Similar to before, a net positive charge arises on the left.
	Figure 2.15d. Net charge is plotted on the vertical axis. On average (that is, averaged over a time scale equal or greater to one period), there is net positive charge near both electrodes.
	Figure 2.15e. The electric field (vertical axis) may be found by Gauss's law. It increases in regions of net positive charge. The absolute value of zero electric field in the center of the plasma may be inferred either from symmetry, or by usual arguments that the electric field in a conductor is zero.
	Figure 2.15f. Finally, by integration of the (negative of) the electric field, the DC potential is obtained. The plasma is at a positive potential with respect to the electrodes.

distance progresses through the neutral region, the enclosed charge, and thus the electric

field, remains constant. Finally, as the distance passes into the second region of positive

net charge, the enclosed charge and electric field increase again. As we are integrating,

we have inferred the increasing trend of the electric field but not its absolute value (an

integration constant may be added; alternatively, in terms of Gauss's law, we do not *a*

priori know if the electrodes are charged). By symmetry, the electric field in the neutral

region must be zero. Alternatively, since the plasma has free carriers, the usual argument

that an electric field must be zero within a conductor applies. This determines the

qualitative features of the electric field, as shown in 2.15e. That is, it points towards

either electrode. Finally, the electric field may be integrated (and multiplied by -1) to

determine the potential, as in Figure 2.15f. Again, an integration constant may be added,

but the important feature is that the center of the plasma is at higher potential than the

electrodes.

We can consider the development of this positive plasma potential in one other

way: how the potential develops at the gun as a function of time as the plasma is ignited.

Figure 2.16 shows the (qualitative) potential on the cathode as a function of time. Before

the plasma is ignited, the AC oscillations are symmetric about ground, as is typical for

AC. As electrons are ejected from the gun and a sheath of positive charge builds in front

of the gun, the DC potential of the gun decreases. (It might be naively expected that

positive charge will attract negative charge and hence be at a positive potential, but the

entire system, as in Figures 2.15, needs to be taken into account) The potential continues

to oscillate around this decreasing DC potential. When the potential is negative, positive

ions are accelerated towards the target, and sputtering occurs. At the moments when the

potential rises above zero, electrons are accelerated towards the target, so AC current, and

thereby the plasma itself, may be maintained. These segments of the cycle must

necessarily be in the minority, again, so the plasma does not completely discharge. The

need for some segments of the cycle to be positive (to maintain AC current) while the

average potential must be negative (to prevent electrons from completely leaving the

plasma) are two competing effects which determine the equilibrium DC potential of the

gun.
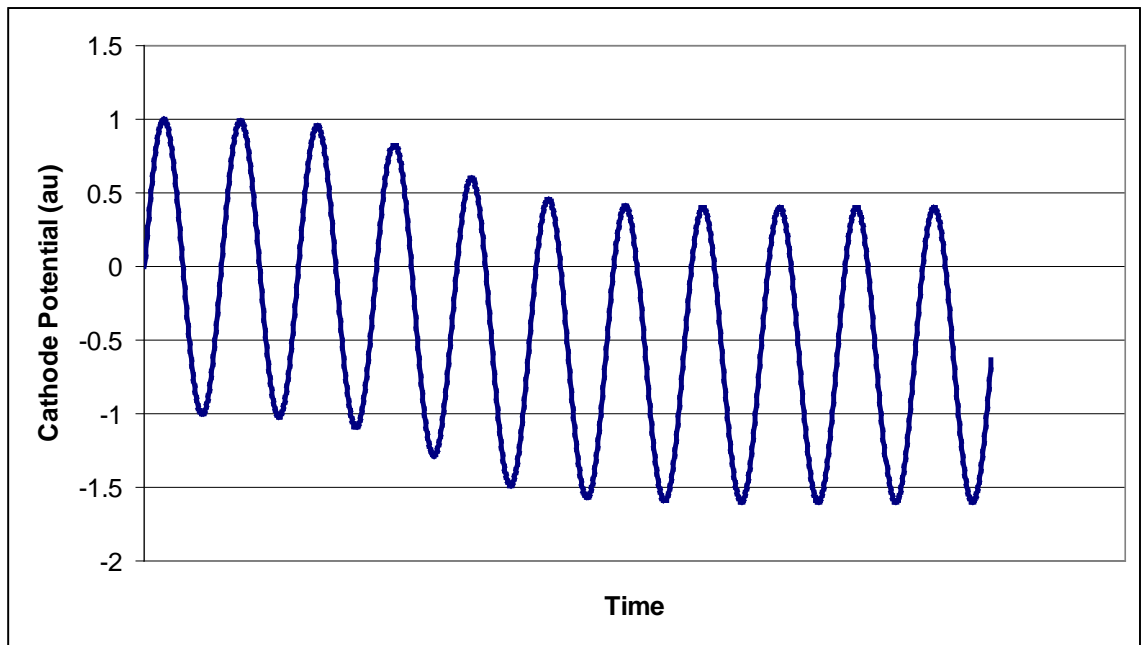
Figure 2.16. The potential on the cathode as a function of time as the plasma is ignited.
Before ignition, the DC potential is zero. After ignition, the DC potential decreases to a
negative stable value. When the potential is below zero, sputtering may occur; when the
potential is above zero, electrons are replenished in the gun, maintaining AC current. This
graph is for illustrative purposes and is not taken from data.

The previous treatment dealt with the plasma on a microscopic level, by

considering motion of electrons and such. On a macroscopic level, plasma ignition was

described by Friedrich Paschen. He discovered that the breakdown voltage was given by

$$V = \frac{a(pd)}{\log(pd)+b}$$

[2.15]

where p is the pressure, d is the cathode-anode distance, and a and b are constants dependent on the gas composition. The logarithmic dependence comes from assuming the electron current increases with distance at a rate proportional to the current at that distance (in other words, the electron current increases exponentially with distance). Figure 2.17 shows graphs of breakdown voltage versus pd for various gasses. As our gun-substrate distances are on the order of 6 cm and our operating pressures are on the order of 10 mTorr (0.01 mmHg), our situation is always on the left side of the graph, so if temporary pressure adjustments are needed to ignite the plasma, the adjustment would always be to raise the pressure (generally over 100mTorr).

For there to be a minimum in the breakdown voltage, there must be two competing effects. At low pressure, there are fewer atoms to be ionized to supply electrons to the plasma. At high pressure, the mean free path is less, so ions gain less kinetic energy as they move through the potential between collisions, meaning they have less energy to ionize further atoms.
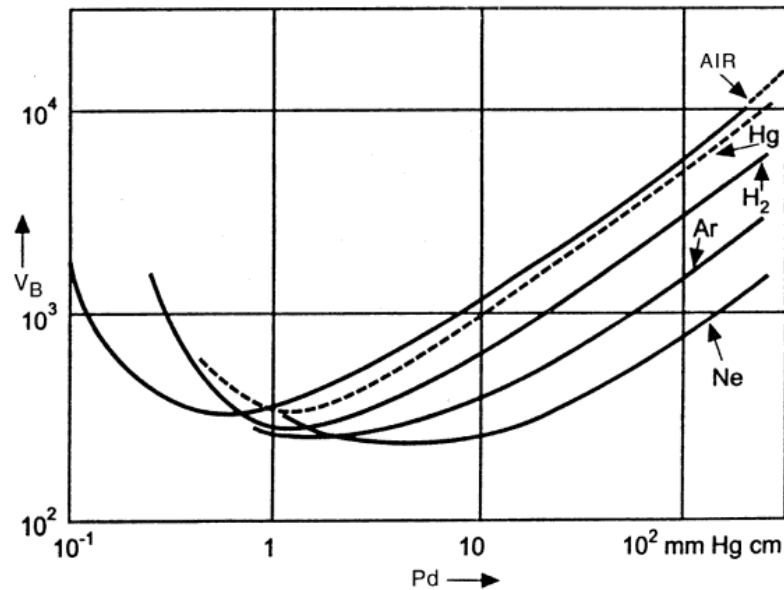
Figure 2.17. Paschen curves. Breakdown voltages versus pressure times distance for a variety of gases.[25]

2.7 Magnetron Sputtering

A sputter gun may use a magnetic field to control the path of electrons. This is the case in magnetron sputtering. Generally, a magnetron in a sputter gun consists of one magnet in the center of the gun and a ring of magnets in the periphery of the gun oriented with opposite polarity (so that they would be north-up if the center magnet was south-up). The outer magnets may be in a continuous ring or an arrangement of discrete magnets. Figure 2.18 shows a sputter gun that has been disassembled, with the ground shroud and target removed, revealing the magnets below. The magnets are surrounded by the cathode, which is made of copper, both for conductivity and cooling (water flows into the cathode) reasons. Beneath the copper cathode is a piece permeable soft iron, a "yoke" to provide magnetic flux linkage on the back side.

Figure 2.18. A sputter gun with the ground shroud and target removed, revealing the underlying magnets. This image is looking down the axis of the gun, which points towards the substrate.

An electron (or ion) moving in a magnetic field experiences a Lorentz force $\vec{F} = q\vec{v} \times \vec{B}$, with q the electric charge, v the velocity of the particle, and B the magnetic field vector. If the electron is moving in the direction of the field, the magnetic field imparts no force. If the electron is moving skew to the magnetic field, it will be deflected. In the simple case of a uniform magnetic field, an electron will have components $v_{\parallel}$ parallel to the magnet field and v_T perpendicular. $v_{\parallel}$ is uninfluenced by the magnetic field. The cross product of v_T and B results in a centripetal force qvB. By equating this with the general expression for a centripetal force, we determine the radius of gyration is $r = \dfrac{mv}{qB}$. Since $v_{\parallel}$ is unchanged while v_T rotates, the net motion is of a helix about the magnetic field. See Figure 2.19. To put it simply, the magnetic field generally forces charged particles to move generally (averaged over several gyrations) parallel to the magnetic field. In the situation where an electric field is also present (which of course will actually be the case while sputtering), the electron may not be confined to move parallel to the magnetic field itself. Suppose B is in the z direction,

$$\vec{B} = (0, 0, B)$$ [2.16]

while v is arbitrary

$$\vec{v} = (a, b, c).$$ [2.17]

The electric field may have a component in the z direction. This component will accelerate the electron in that direction, but will not mix in a complicated manner with the magnetic field. Therefore, we focus only on the electric field in the x-y plane

$$\vec{E} = (E_x, E_y, 0).$$ [2.18]

Applying the cross product, we find the Lorentz force

$$\vec{F} = (qbB + qE_x, -qaB + qE_y, 0).$$ [2.19]

Applying Newton's second law, we get the differential equations

$$a' = \frac{qB}{m}b + \frac{qE_x}{m}$$ [2.20]

$$b' = -\frac{qB}{m}a + \frac{qE_y}{m}$$ [2.21]

Differentiating the top equation and substituting from the bottom gives

$$a'' = -\frac{q^2 B^2}{m^2}a + \frac{q^2 BE_y}{m^2}$$ [2.22]

which has solution (phase chosen out of convenience)

$$a = R\sin\left[\frac{qB}{m}t\right] + \frac{E_y}{B}$$ [2.23]

Likewise,

$$b = R\cos\left[\frac{qB}{m}t\right] - \frac{E_x}{B}$$ [2.24]

The trigonometric terms demonstrate that the electron is still gyrating, but the other terms show that the axis of gyration is not parallel to the z axis. If Ez=0, so the electron is only deflected and does not have its speed increased, then the axis of gyration is parallel to

$$\left(\frac{E_y}{B}, -\frac{E_x}{B}, c\right)$$ [2.25]

where, again, c is the z component of the velocity. These calculations are summarized by Figure 2.19.
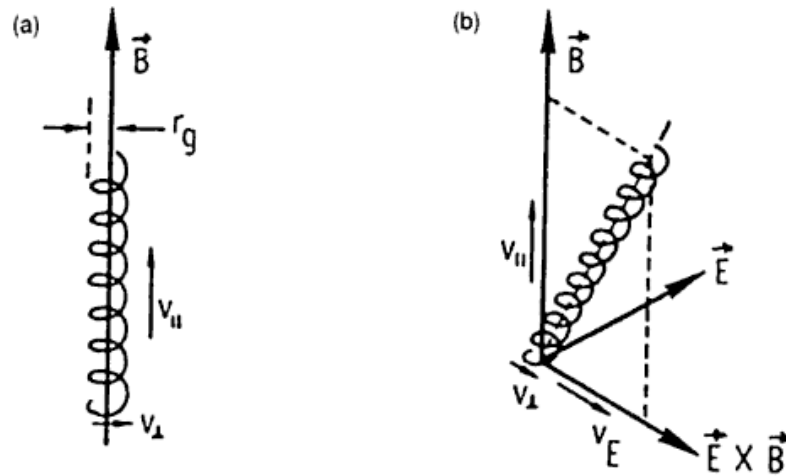
Figure 2.19. Motion of an electron under the influence of (a) a uniform magnetic field and (b) perpendicular uniform magnetic and electric fields.[26]

This gyration has two important effects. First, by gyrating while moving, the effective path of the electron is lengthened, making it more likely to collide with and possibly ionize other particles. Secondly, it works to confine the charged particles. Figure 2.20 shows magnetic field lines and electron trajectories above a sputter target.
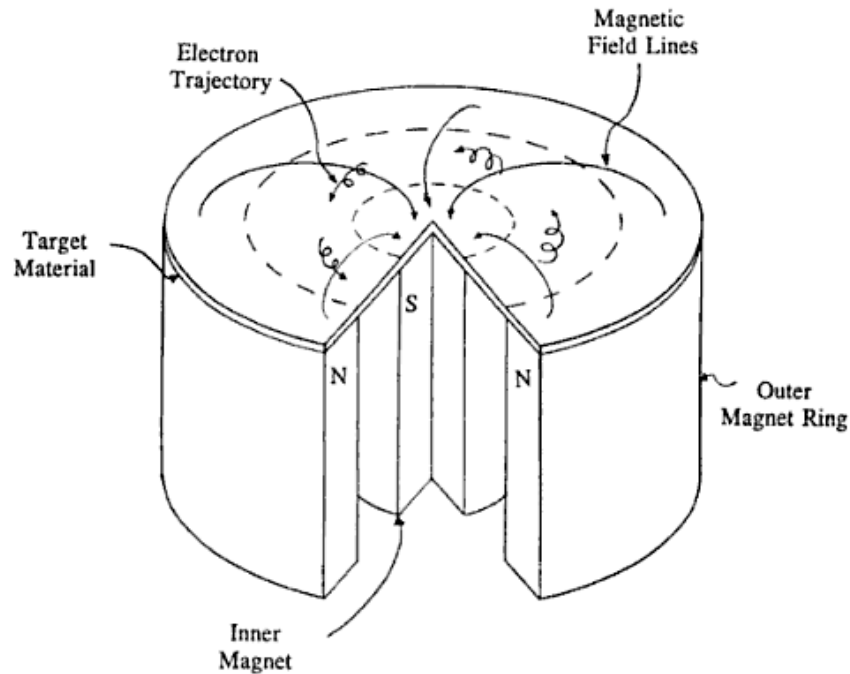
Figure 2.20. Magnetic field lines and electron confinement above a sputter target.[27]

The magnetic field comes from the north poles and enters the south poles. Between the two, the magnetic field bends parallel to the surface of the target. The electric surface is perpendicular to the target over its entire surface, so where the magnetic field is parallel to the target, the two fields are perpendicular. The deflection described above causes the electrons to move in a circle about halfway between the center and outer magnets. This causes the plasma to be most dense in this region which also causes the material in the target there to be sputtered at a higher rate. See Figure 2.21.

Figure 2.21. (Left) A sputter plasma used in depositing a solar cell. The sputter gun is on the left, facing the substrate holder on the right. (Right) By reducing the camera exposure, the high density ring of plasma above the race track is seen more clearly.

The ring of removed material, of radius about half the radius of the target, is commonly called the racetrack. See Figure 2.22.

Figure 2.22. An eroded ZnO:Al target. (top) Overhead view. (bottom) Side view. The bulk of the erosion has occurred within a circular region of radius about half of the radius of the target. This is the so-called "racetrack". This target is 95% through its useful life, as the target can no longer be used after the erosion depth at the race track equals the thickness of the target.

2.8 Typical Values of the Magnetic Field

We have used a gaussmeter to measure values of the magnetic field above a Kurt J. Lesker commercial sputter gun. Above a quarter inch sputter target, the field is about 430 gauss at the edge maximum and -700 G in the center. Between the two, with the gaussmeter held perpendicular to the target (so that the field is measured parallel to the target), the maximum was 280 G. On the other hand, our laboratory has once used a home-made sputter gun that we could fill with any magnets we choose. We found that

using stronger magnets, such as (again, with a target in place) 0.8 kG at the edge and 1.15

kG at the center, limited the race track to a region only millimeters wide.

2.9 A Sputtering Mechanism

We have described how, inside a sputter chamber, a plasma develops and how

ions are accelerated into a sputter target. It may not be obvious, however, how an ion

colliding *into* a sputter target causes the target material to go *out of* the target.

It is unlikely for an incoming ion to hit one atom in the target directly, but is more

likely to strike between atoms. Of those two atoms, it is again unlikely to hit exactly

between them, but is more likely to strike one at a sharper angle and the other at a

shallow angle. More energy is delivered to the atom struck at a sharper angle, called the

high energy knock-on; the other atom is called the low energy knock-on. See Figure

2.23.
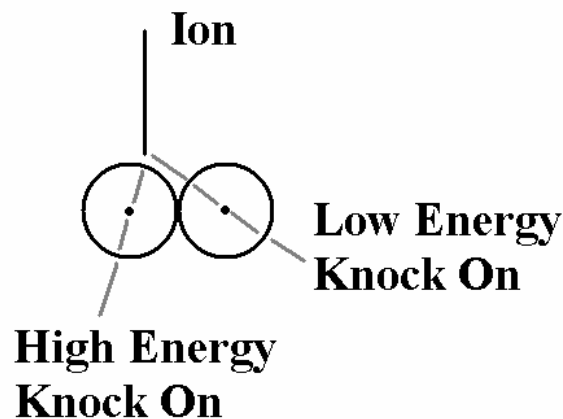
Figure 2.23. An ion colliding with a sputter target may hit two atoms in the target, but at different angles. The atom that is hit most directly has the most kinetic energy transferred to it, and is called the high energy knock-on; the other atom is the low energy knock-on.

The high energy knock on may be driven into the target. The low energy knock

on will be driven laterally, where it may collide with other atoms in the target. As in the

initial collision, the low energy knock on may collide with two other target atoms at

different angles. One of the atoms in the second collision may be driven into the target,

while the other may receive momentum to cause it to be ejected from the target. See

Figure 2.24. This is called the mole mechanism[28]; as a mole digs under ground, raising

the level of the ground above it, atoms driven into and parallel to the target impart

upward momentum to atoms above.
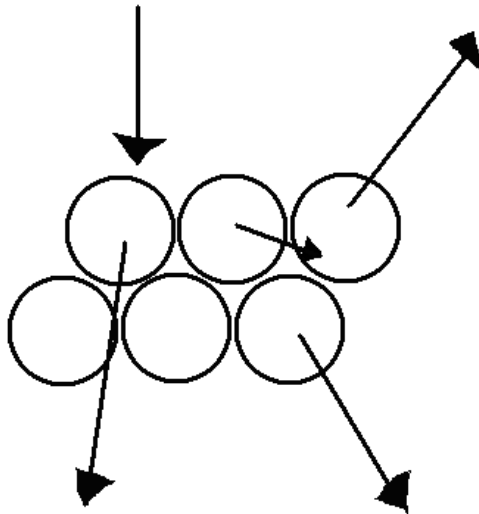
Figure 2.24. The mole mechanism. After the initial collision of an ion,
momentum may be transferred in subsequent collisions to force an atom out
of the target.

2.10 Effect of Sputter Parameters

It is important for any technician or scientist growing films through sputtering to

be able to control film quality. This is done by adjusting the parameters of the sputter

deposition: Primarily, the working pressure and temperature. Also adjustable are RF (or

DC) power to the target, substrate-sputter gun distance, gas flow rates, gas ratios (in the case of reactive sputtering), magnetic field configurations, and substrate bias.

2.11 Effects of Temperature and Pressure

Figure 2.25 summarizes the various effects of temperature and pressure in Thornton's four zone (I, T, II and III) scheme. The most noticeable distinctions are along the temperature axis (which measures substrate temperature divided by material melting temperature). The trend is at lower temperatures for films to be composed of small grains, while grain size increases with increasing temperature. At very low temperatures, low surface adatom mobility implies deposited atoms remain where they first land, and shadowing (existing islands of deposited material can block incoming atoms) is a factor. Films deposited in this zone may be amorphous. In zone II, adatom mobility determines film microstructure. At very high temperatures, zone III, deposited films may recrystallize.
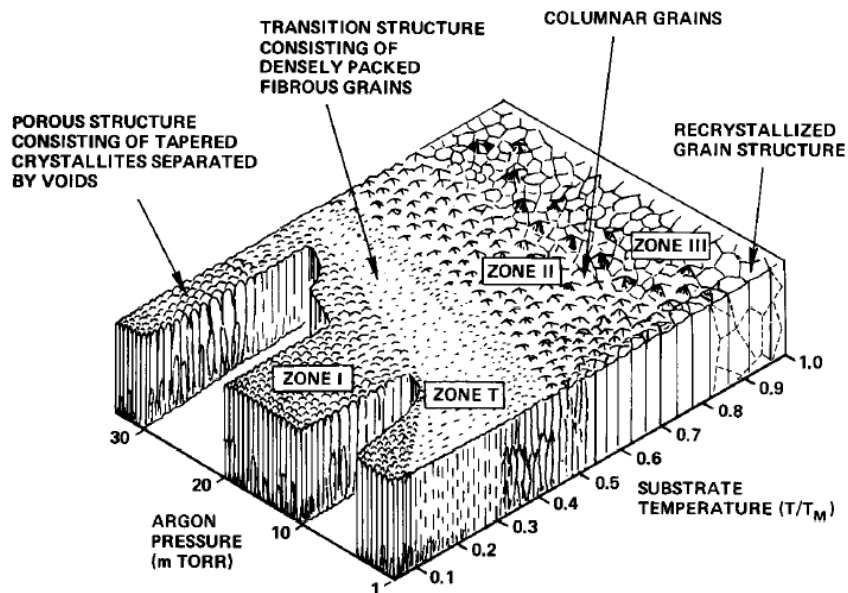
Figure 2.25. Generic traits of sputtered thin film microstructure as a function of temperature and pressure.[29]

Pressure controls film density (as shown in the cutaways in Figure 2.25). High

sputtering pressures are associated with porous films. At low pressures, incoming atoms

have higher energy from fewer collisions in the plasma, and when they collide with the

growing film, the collision tends to make the film more dense. This is called atomic

peening.

2.12 An Example of the Effect of Pressure on Films – Sputtered Molybdenum

Molybdenum is especially sensitive to deposition pressure. It is unusual in that

the stresses in the film from the growth process can be great enough to cause the film to

spontaneously delaminate from the substrate. See Figure 2.26.
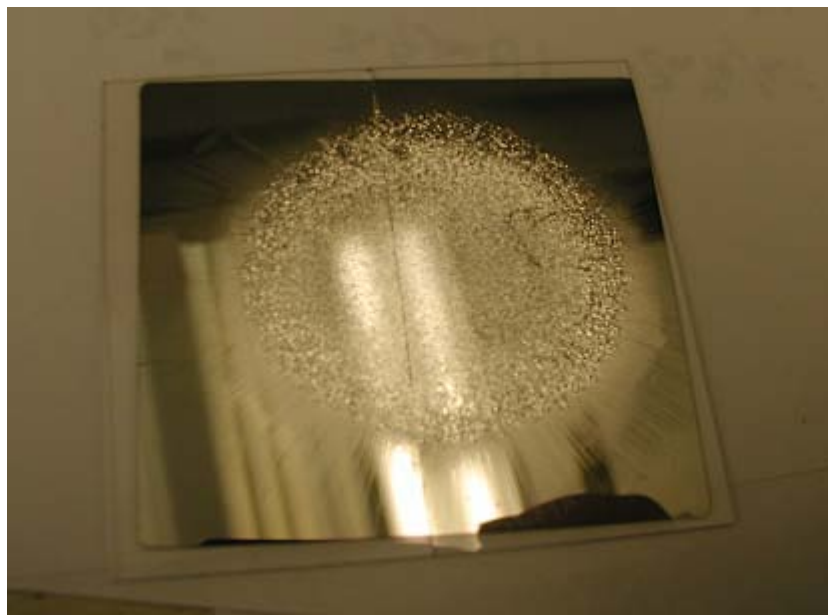
Figure 2.26. A molybdenum film on soda lime glass deposited
by sputtering. The stresses in the film have caused it to
spontaneously delaminate.

We have grown molybdenum films at various pressures and performed x-ray diffraction (XRD) on those films. XRD was also performed on a sheet of bulk molybdenum as a reference.

The films were grown in a system pumped by diffusion pump (with LN_2 cold trap) to a base pressure near $1x10^{-6}$ Torr. A two-inch diameter target was used. A DC sputtering power source operating at 100 watts powered the deposition. The substrate-to-gun distance was 20 cm.

The general results are shown in Figure 2.27, with a close up of the (110) peak in Figure 2.28.
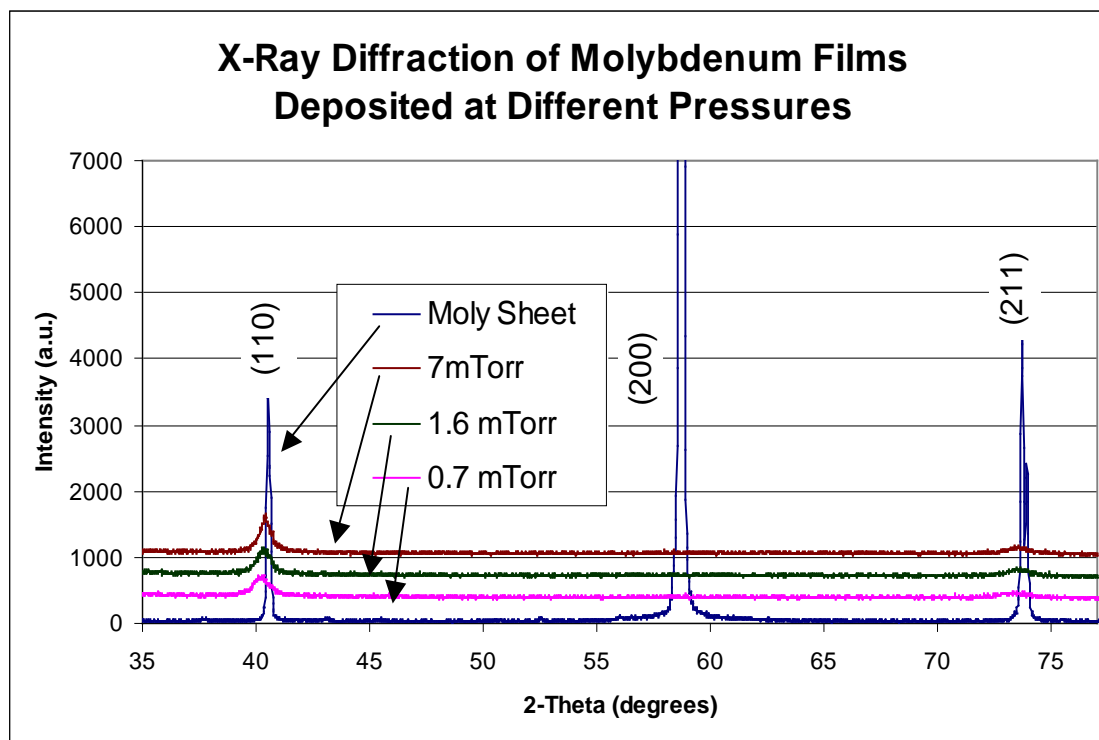
Figure 2.27. X Ray diffraction of molybdenum films grown at different pressure conditions. The (110) peak is most prominent in the sputtered films, whereas the (200) peak of the bulk sheet is not present at all in the sputtered films.
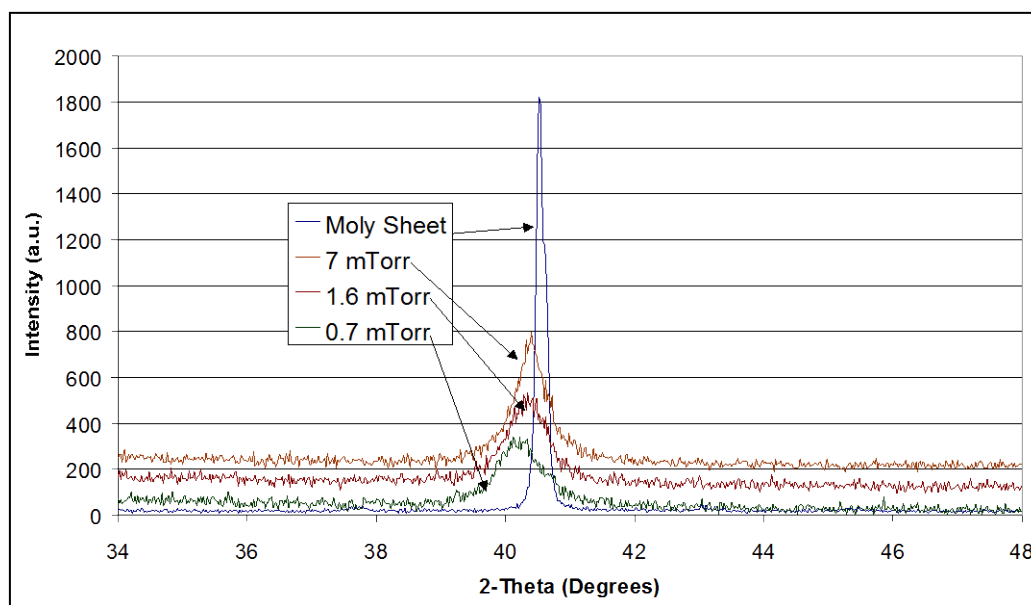
Figure 2.28. The (110) peak in sputtered molybdenum films is seen to shift to lower values of 2-theta with lower deposition pressures.

The (110) peak shifts to lower values of 2-theta with lower deposition pressures. This corresponds to *larger* values of <110> plane separation with lower deposition pressures. Those planes are perpendicular to the plane of the film. There is tensile strain perpendicular to the plane of the film. Molybdenum has a Poisson's ratio of 0.3 (0 would imply no cross section change for a transverse force, such as with cork; 0.5 would reflect an incompressible material whose cross section change would need to exactly compensate for any transverse elongation (so the volume does not change), as for rubber; and negative values, implying elongation in all directions, as low as -1 are possible)[30]. Therefore, by Poisson's effect, a tensile strain perpendicular to the plane of the film may be inferred to be the result of biaxial compressive strain in the plane of the film. This compressive strain at low deposition pressures may be understood to be the result of the increased film density due to atomic peening as described in the previous section.

The data from the Figure 2.28 is shown numerically in Table 2.1. The terminology is that a film that delaminates "immediately" means it has already delaminated when removed from the sputter chamber, or delaminates on the order of minutes upon removal. "Eventually" means the delamination may occur after several days. Films that "never" delaminate may exist for several years (and counting) without delaminating.

Table 2.1. Shift of lattice spacing in molybdenum films as a function of sputter pressure.

Sample	<110> spacing (Å)	<110> strain	Delaminates
Reference	3.1468		
Molybdenum Sheet	3.147	0.00 %	
7 mTorr Deposited	3.156	0.29 %	Never
1.6 mTorr Deposited	3.162	0.48 %	Eventually
0.7 mTorr Deposited	3.17	0.73 %	Immediately

2.13 Effect of growth rate

Growth rate is not an independent parameter, but may be influenced by RF power, pressure, and gun-substrate distance. It is normally not considered separate from those factors, but can play a role in certain cases. As an example, we have sputtered a titanium target using 100 W DC power, and with a substrate-gun distance of 20 cm (these films were grown in the same system as the previous molybdenum films). We obtained a transparent, insulating film – titanium oxide. By changing the substrate gun distance to 4 inches and increasing the power to the gun to 200 W, we increased the growth rate and obtained an opaque, conducting film – titanium. Titanium is known as a strong oxidizer, and the longer titanium atoms remain in a gaseous state before depositing, the greater the chance they have of reacting with any residual oxygen in a system.

2.14 Conclusions

Sputtering is a method for depositing films of various materials, some of which may be used in solar cells. The properties of these films may be controlled by adjusting sputtering parameters such as temperature and pressure. In the following chapters, we will describe how the parameters of zinc oxide in particular vary as a function of deposition conditions, and how those parameters influence the ultimate performance of solar cells.

Chapter 3 -- The Solar Cell Model

3.1 Introduction

Like batteries, solar cells have positive and negative terminals. Solar cells have a difficulty in that, to admit light, at least one terminal must be transparent as well as conductive. Certain oxides can be used for this purpose; they are called transparent conducting oxides (TCOs). Normally, transparency and conductivity are considered mutually exclusive: Transparent materials are semiconductors with a large bandgap and therefore low concentration of electrons in the conduction band, whereas conductors are metals with a partially filled conduction band. TCOs are degeneratively doped so that there are a high densityelectrons available in the conduction band; however, the density of states available for absorption is low.

For our cells in particular, our use of zinc oxide doped with aluminum (ZnO:Al, also AZO) as a TCO is notable as a novelty, as it is rarely used in CdTe solar cells, and our cells, to our knowledge, are the best that use ZnO as a TCO on a polymer substrate. ZnO is also less expensive than indium tin oxide (ITO), a competing TCO, due to the rarity of indium.

The need for transparency generally means the conductivity is compromised. Therefore, the TCO is generally the limiting resistive element. Properties of a TCO determine or can be used to control ultimate shunt and series resistance in a complete solar cell.

This chapter will first review the standard diode model for solar cells[31], describing how parasitic resistive effects affect solar cells in general and in a theoretical manner. At the end of this chapter, we present a simple model for very poor cells, which is neglected in standard treatments. The following chapters will present experimental data, explained by a model, on the series resistance parasitic effect, explanation of how a buffer layer will affect the shunt resistance parasitic effect, and will describe the properties of our ZnO that further influence these effects.

3.2 Solar Cell Model

Solar cells may be generically modeled as a current source and a diode. Parasitic effects are modeled as two lumped resistances, a series resistance and a shunt resistance (or shunt conductance, to emphasize that cell performance is maximum when both series resistance and shunt conductance are zero). See figure 3.1.
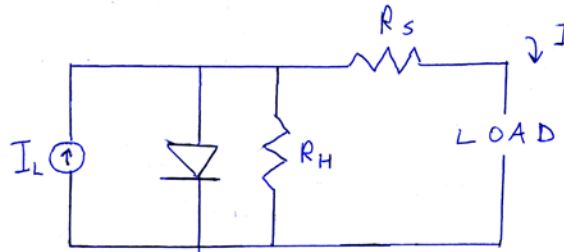
Figure 3.1. A solar cell may be modeled as a current source and a diode, and possible shunting (R_H) and series (R_S) resistances.

Applying Kirchoff's rules to the circuit model allows us to obtain the equation for describing a solar cell.

$$I = I_L - I_o\left(e^{\frac{q(V+IR_s)}{nkT}} - 1\right) - \left(\frac{V+IR_s}{R_H}\right) \tag{3.1}$$

In this equation, I and V are the current and voltage, respectively, through and on

the load; I_L is the light-induced current in the solar cell; I_O is a diode reverse saturation

current; q is the fundamental electron charge; n is a diode ideality factor, a unitless

number between 1 and 2, generally used as 2 for CdTe cells; k is Boltzmann's constant; T

is the operating temperature; R_S is the series resistance, and R_H is the shunt resistance.

The equation is transcendental; neither I nor V may be fully solved in elementary

terms of the other so long as both R_S and R_H are non-zero and finite.

In this equation, the convention is that the light-induced current is positive. This

is a result of the direction of current flow from the current source. It implies the power

quadrant is the first quadrant. That is, the power quadrant is the region on the IV curve

where the solar cell supplies power to the load rather than drawing power from it. A

different convention is that the light-induced current is negative, so that the power

quadrant is the fourth quadrant. The resulting current-voltage (IV) curves are identical

either way, aside from a reflection about the x-axis. It is therefore easy to determine

which convention is used, even when it is not specified. Regardless of equations, we will

always use the convention that the power quadrant is the fourth quadrant for clarity when

discussing regions of the IV curve.

Although the equation was derived in terms of current, the current should be

proportional to the active cell area. Therefore, the current is often divided by that area

and the cell's properties are expressed in terms of current density (a more intrinsic

property of the cell) rather than current. In the equation, all I's may be exchanged with

J's (and in that case, R_S and R_H must be given in ohm-cm^2).

In the ideal case, $R_S=0$ and $R_H=\infty$, and the JV curve is simply an exponential.

Figure 3.2 shows such a curve. In that case, J_L (and the current at short circuit, J_{SC})

=25.9mA, $J_O=1.18\times10^{-6}$mA, and $n=2$. This leads to an open circuit voltage (V_{OC}) of 845

mV. These parameters were chosen such that this ideal cell has the same J_{SC} and V_{OC} as the

world record CdTe cell. The power is maximized when the product of current density and

voltage is maximized; this occurs in this case at V=710 mV and J=24.15mA/cm^2, for a

maximum power of 17.1mW/cm^2 (and an efficiency of 17.1%). The maximum power

divided by the open-circuit voltage and the short-circuit current is known as the fill factor

(FF). The fill factor may be thought of simply as a measure of how rectangular the
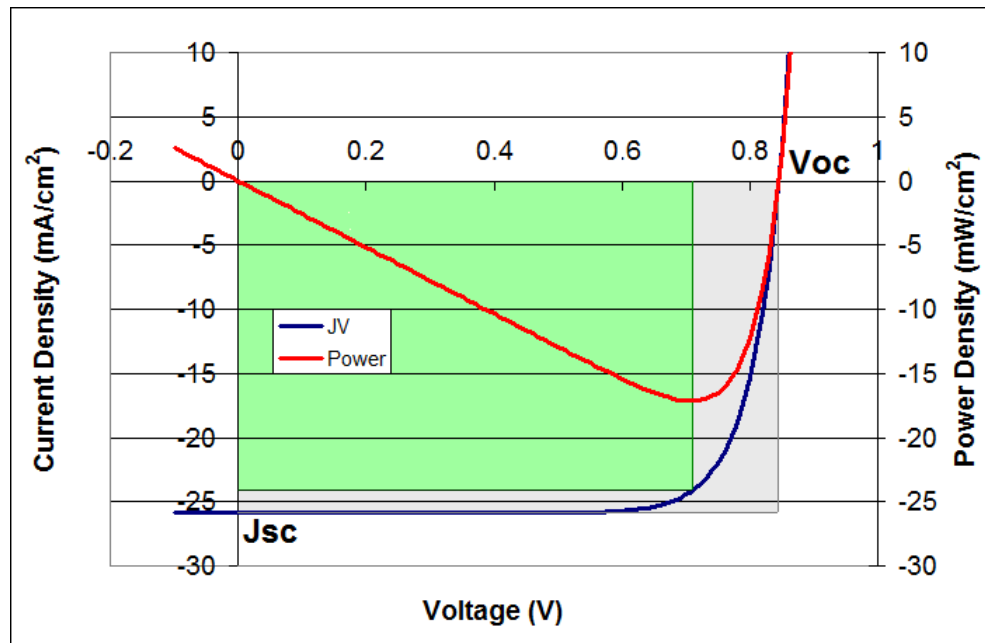
Figure 3.2. A model solar cell JV curve. The JV curve intercepts the y-axis at the value of the short circuit current (Jsc) and the x-axis at the value of the open circuit voltage (Voc). The power generated by the cell for a given voltage is shown by the red curve; it reaches a maximum where the green rectangle intersects the blue curve. The ratio of the areas of the green and gray rectangles is the fill factor.

JV curve is. In this case, the fill factor is 78.3%. The fill factor of the real world-record cell is 75.5%.

These numbers which characterize solar cell performance are often called **metrics**. The first level metric is the most important parameter: the cell efficiency. Efficiency can further be understood to result from the second level metrics J_{SC}, V_{OC}, and FF. Due to the power from the sun (AM1.5) being 1000 W/m^2, efficiency is conveniently given as a percentage simply by the product $J_{SC} * V_{OC} * FF$ (with units as in Figure 3.2). Second level metrics may be further analyzed as third level metrics, including series and shunt resistance.

The discrepancy between the real and modeled solar cell fill factor might suggest that the losses we have neglected in modeling reduce, in a real cell, the fill factor (at least, if not the other parameters as well). This is in fact the case.

3.3 Effect of Series Resistance

To consider the effect of series resistance alone, we remove the shunt resistor (equivalent to setting its resistance to infinity) from the model in figure 3.1. Figure 3.3 shows the resulting model in open circuit (left) and short circuit (right).
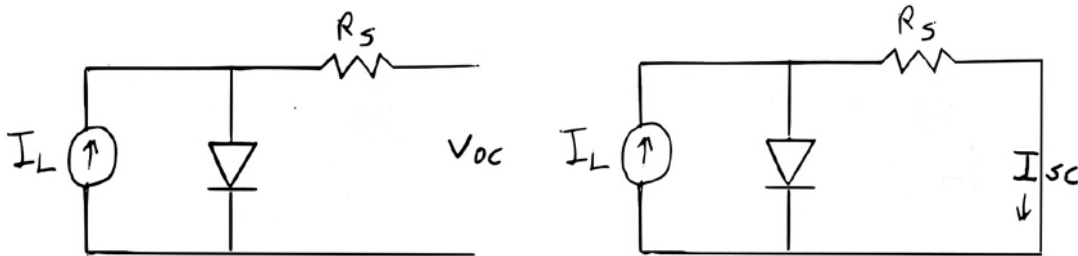
Figure 3.3. Model of a cell with series resistance but no shunt conductance effects at open circuit (left) and short circuit (right). In open circuit, no current flows through the series resistor, so V_{OC} is unaffected. In short circuit, so long as R_S is small compared to the diode's resistance, J_{SC} is unaffected. If R_S is comparable to or larger than the diode's resistance, current will flow through the diode, reducing J_{SC}.

In open circuit, no current flows through the series resistor. Therefore, the series resistance has no effect on the value of V_{OC}. In short circuit, the light induced current has two paths to flow, either through the diode, or through the series resistor (and on through the "load", though the load is zero at short circuit). At short circuit, the diode is in a high resistance regime of its current-voltage behavior, so little current flows through it. However, if the series resistance becomes high enough, it may become comparable to the resistance of the diode, and current may flow through the diode, reducing the current through the load.

We may summarize this by saying the series resistance, at low values, has little effect on the short circuit current, but at high values reduces it.

As the series resistance increases, even at low values, it reduces the fill factor. The series resistance is approximately the inverse of the slope of the JV curve at open circuit. As a slope at open circuit makes the JV curve shaped less like a rectangle, we see how the fill factor is reduced.

With $R_H=\infty$, equation 3.1 may be solved exactly for V in terms of I.

$$V = \frac{nkT}{q} \log\left[\frac{I_L - I}{I_o} + 1\right] - IR_S \qquad [3.2]$$

The second term on the right quantifies the effect of R_S as a voltage drop. Figure 3.4 shows what happens to the JV curve from figure 3.2 as various values of series resistance are introduced into the circuit.
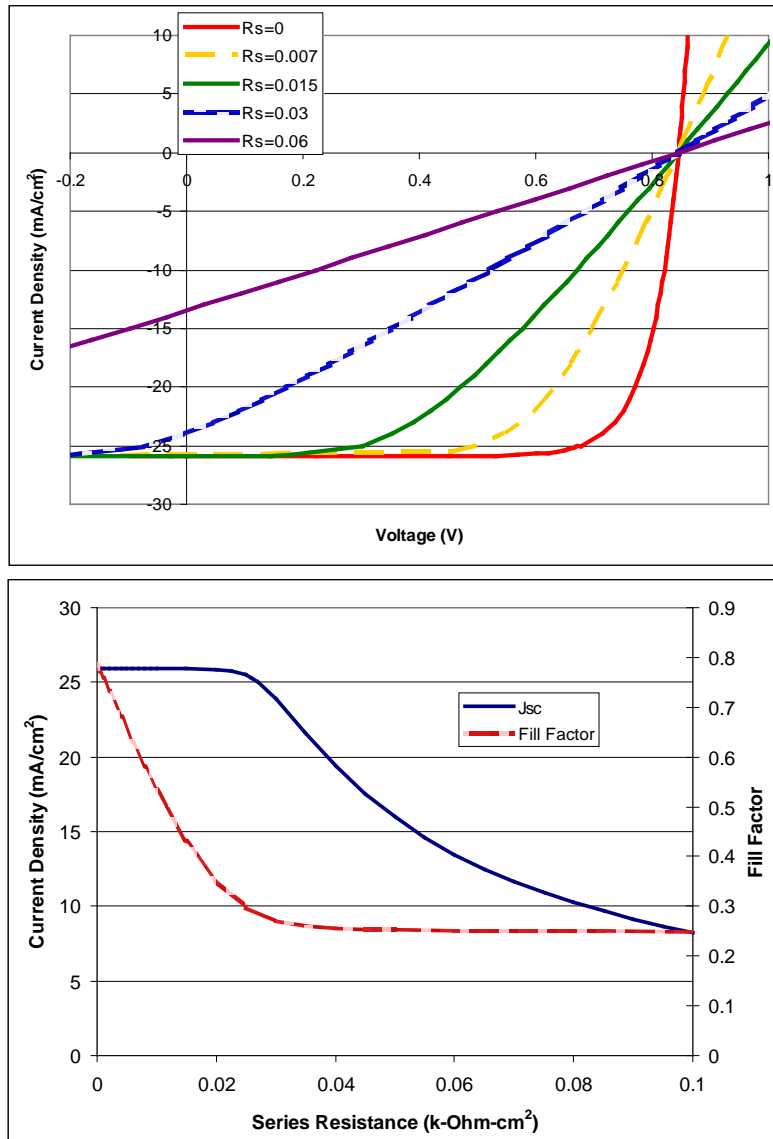
Figure 3.4. The effect of series resistance on solar cell performance. Top: JV curves for cells with the same diode parameters and light induced current as the cell in figure 3.2, but with series resistances of 0, 0.007, 0.015, 0.03, and 0.06 kOhm-cm^2. Bottom: The dependence of short circuit current and fill factor on a continuum of R_S values. V_{OC} is not graphed as it does not depend on R_S.

3.4 The Effect of Shunt Resistance

Figure 3.5 shows circuit models for a solar cell with a shunt resistance (but no series resistance) in open circuit (left) and short circuit (right).

77
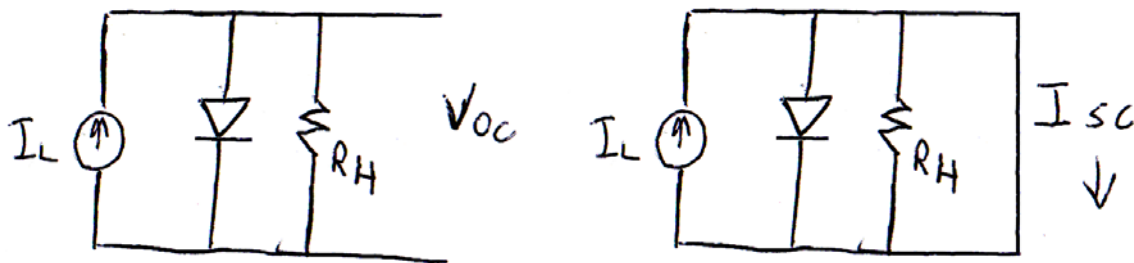
Figure 3.5. Model of a cell with shunt resistance but no series resistance effects at open circuit (left) and short circuit (right). In open circuit, if the shunt resistor is comparable to or less than the resistance of the diode, Voc may be reduced. In short circuit, the load has exactly zero resistance, which must be less than the shunt resistor, so all the current flows through the load; a shunt resistor alone cannot reduce short circuit current.

In short circuit, the shorted load will have infinite conductance. No matter how high the conductance of the shunt (or the diode, though that will usually be in a high resistance regime at short circuit anyway), the load's conductance is so high that the entirety of the light induced current will flow through it. In other words, the shunt resistance alone cannot reduce the short circuit current.

That argument is not true if there is a series resistor as well as a shunt resistor. In that case, even if the series resistance is low enough that it would alone not reduce the short circuit current, if the shunt has resistance less than or comparable to the series resistor, the shunt will divert current from the load. See the later section on very poor cells for more details.

In open circuit, the light induced current will flow through the diode and shunt. At open circuit, the diode is generally operating in a low resistance regime, so most of the current will flow through the diode, and the voltage across the diode (equal to the open circuit voltage) may be similar to the voltage if the shunt was not present. However, if

78

the resistance of the shunt becomes low enough to be comparable to the diode, current will be diverted through it, lowering the open circuit voltage.

Even at high values of shunt resistance, the shunt resistor will reduce the fill factor. The inverse of the slope of the JV curve at short circuit is approximately equal to the shunt resistance.

Figure 3.6 shows the effect on the JV curve from Figure 3.2 as a function of shunt resistance.
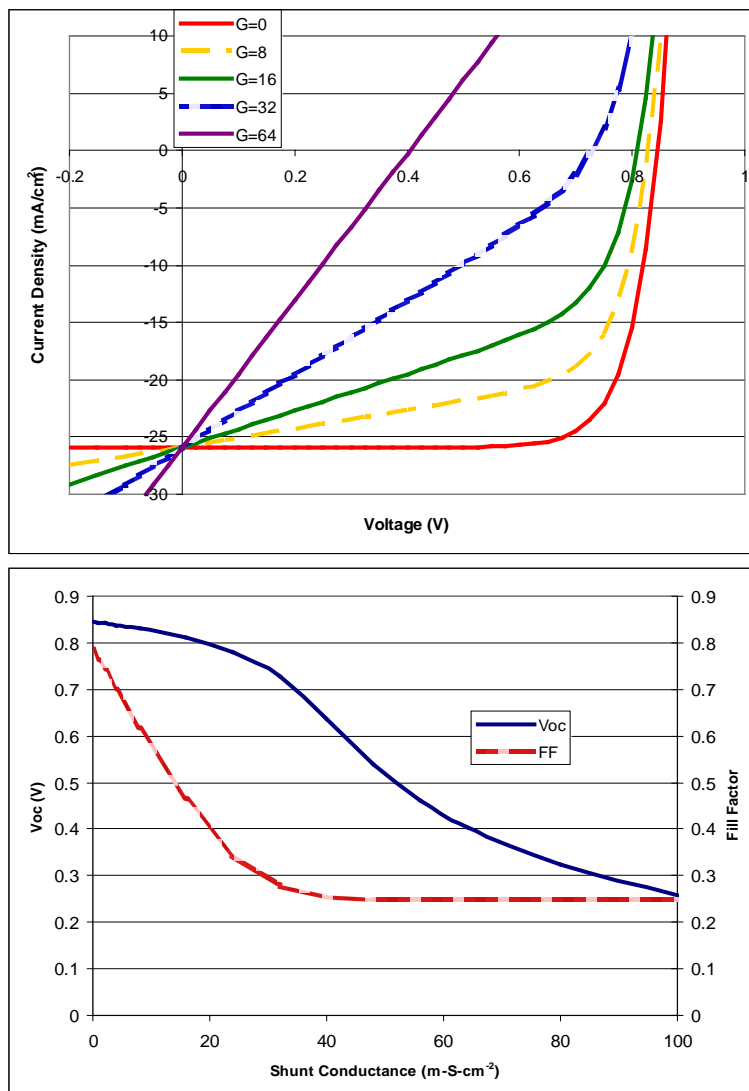
Figure 3.6. The effect of shunt resistance on solar cell performance. Top: JV curves for cells with the same diode parameters and light induced current as the cell in figure 3.2, but with shunt conductances of 0, 8, 16, 32, and 64 millisiemens-cm^2. Bottom: The dependence of short circuit current and fill factor on a continuum of R_H values.

3.5 Back Barriers

We will not model back barriers in this thesis as they have not been a major challenge in our development of superstrate CdTe cells on flexible substrates. However, perhaps we should briefly mention them for completeness. They can be seen in other CdTe cells, such as when they are in the substrate configuration.

A back diode is schematically modeled as shown in Figure 3.7.
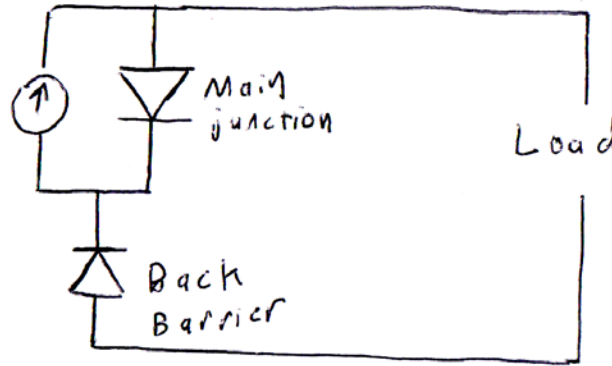
Figure 3.7. A schematic model of a solar cell with a back barrier. The back barrier and main junction diodes point in opposite directions.

The equation describing such a circuit is

$$V = \frac{kT}{q}\left(n_D \log\left[\frac{J_L - J}{J_O^D} + 1 \right] - n_B \log\left[\frac{J}{J_O^B} + 1 \right] \right)$$ [3.3]

with n_D and J_O^D describing parameters of the main junction, and n_B and J_O^B describing parameters of the back barrier.

Figure 3.8 shows example JV curves of a cell with a back barrier. J_O^D and J_L are as the cell in Figure 3.2. The ideality factor for the back diode is also 2. Various values for J_O^B are graphed.
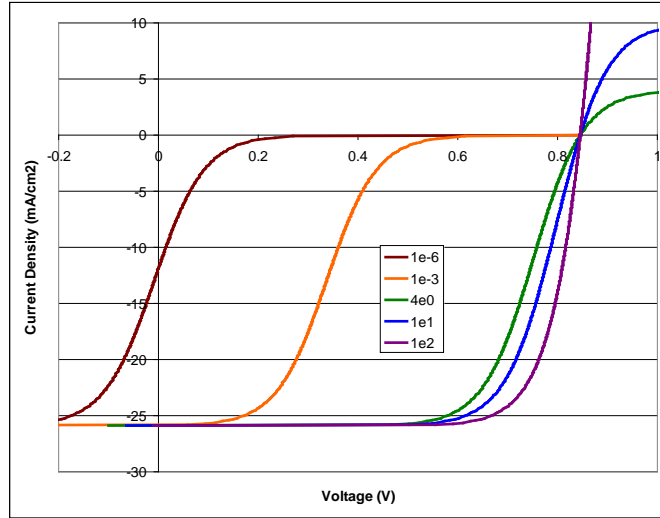
Figure 3.8. JV curves of cells with back barriers. Back barriers will cause "roll over" in the first quadrant and may drastically reduce fill factor. Graphed are back barriers described by $J_O^B=1x10^{-6}$, $1x10^{-3}$, 4, 10 and 100 mA/cm^2.

When the current is negative (using the convention of figure 3.8), the back diode is in forward bias and has low resistance. It therefore may have little effect on the JV curve in most of the power quadrant (at least qualitatively). However, when the current is negative, the diode becomes highly resistive, and will not allow current more negative than $-I_O^B$, the reverse saturation current of the back diode to flow (unless the back barrier breaks down). This causes the JV curve to "roll over" (have negative second derivative).

Those statements describe the situation where the back barrier is much weaker than the main junction (such as $J_O^B=4$, 10, or 100 mA/cm^2 in figure 3.8; recall for the main junction, $J_O=1.18x10^{-6}$mA/cm^2). The lower the value J_O for any diode, the stronger the junction; in the standard model (equation 3.1), the lower the value of J_O, the higher the open circuit voltage. If the back junction is of equivalent strength to the main

junction, then the JV curve throughout the power quandrant will be drastically effected (such as when $J_O{}^B=1x10^{-6}$ mA/cm^2).

The main effect of a back barrier in the power quadrant is to reduce fill factor. If we were simply to eye-ball figure 3.8, we might guess V_{OC} is unchanged in the case that $J_O{}^B=4$, 10, or 100 mA/cm^2, but is reduced to 0.6 V in the case that $J_{OB}=1e-3$ mA/cm^2, and is reduced to 0.4 V in the case that $J_O{}^B=1e-6$ mA/cm2. Based on equation 3.3, a back barrier will theoretically not reduce open circuit voltage; however, for cases of extreme roll over, the situation is so delicate (the JV curve is so nearly parallel to the x-axis for so long) that any further perturbation can greatly reduce V_{OC}.

3.6 The Very Poor Cell Model

In good or at least reasonably performing cells, some results can be obtained simply, without needing to apply the full diode solar cell model. The simple results are:

1. The slope at open circuit is approximately the inverse of the series resistance.

2. The slope at short circuit is approximate the inverse of the shunt resistance.

3. Series resistance primarily affects short circuit current and not open circuit voltage.

4. Shunt resistance primarily affects open circuit voltage and not short circuit current.

For a cell with large resistive parasitic effects, these may no longer be true. Of course, the full diode equation 3.1 still applies, but we would like to have results for very poor cells that are just as simple as for the reasonable performing cells. It may be just as

important to be able to progress from very poor to good cells as it is to progress from good to excellent.

We see in figures 3.4 and 3.6 that as the series resistance and shunt conductance become very large, the JV curves tend to become straight lines and the fill factor approaches 25%. That is not merely the case in those images, or with the parameters represented there; at their worst, parasitic resistances cause the JV curve in the power quadrant to be a straight line.

For any JV curve which is a straight line in the power quadrant, the fill factor is always 25%, regardless of the short circuit current or open circuit voltage (fill factor may, however, be reduced to below 25% by a reverse diode, as in the previous section). Figure 3.9 shows a derivation demonstrating that any straight line JV has a maximum power point at (Voc/2, Jsc/2), and a fill factor of 25%.

$$y = \frac{J_{sc}}{V_{oc}} x - J_{sc}$$

$$\text{Power} = xy = \frac{J_{sc}}{V_{oc}} x^2 - J_{sc} x$$

$$\frac{dP}{dx} = 2 \frac{J_{sc}}{V_{oc}} x - J_{sc} = 0 \rightarrow V_{max} = \frac{V_{oc}}{2}$$

$$J_{max} = J_{sc}/2$$

$$FF = \frac{V_{max} J_{max}}{V_{oc} J_{sc}} = \frac{1}{4}$$
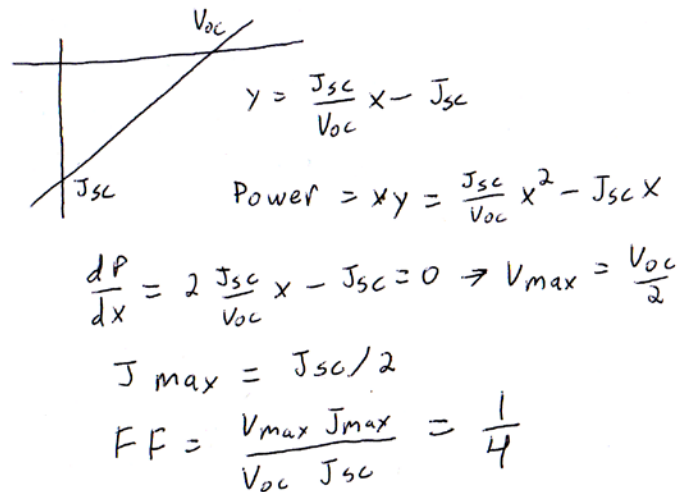
Figure 3.9 Derivation of the properties of a straight line JV. The maximum power point is at (Voc/2,Jsc/2) and the fill factor is 25%.

The solar cell model described above is somewhat idealized, but it may be idealized even further by treating the diode not as displaying exponential behavior, but

rectifying behavior. At low and negative voltages, a diode has large resistance. Past a certain voltage, a diode has very small resistance. It can be modeled therefore as having the JV characteristics shown in Figure 3.10. We will use this simplification to diode behavior again later.
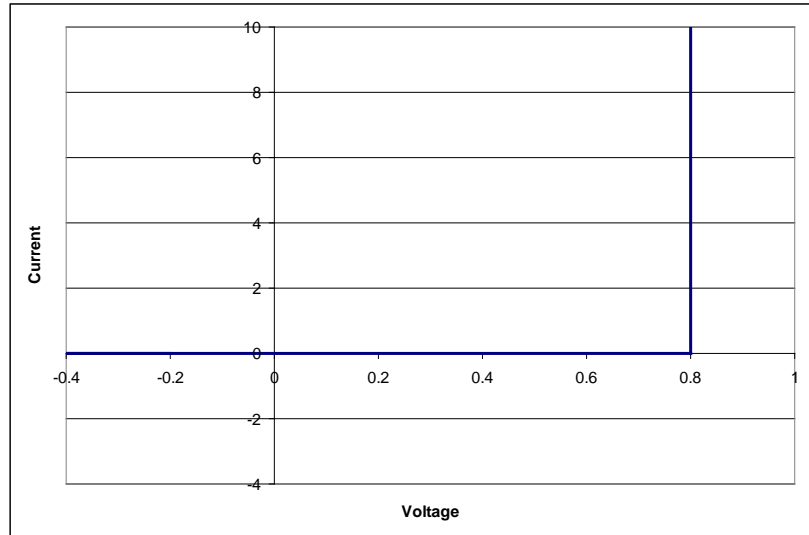
Figure 3.10. A simplified (rectifying) model of a diode. Below a certain voltage W (in this case, 0.8), no current may flow through the diode. After a voltage drop of W is across the diode, any current may flow in the forward biased direction.

We assume that in a very poor cell, the diode is acting in the high resistance regime. This allows us to simply remove the diode from the solar cell model. We are left with the model shown in Figure 3.11.
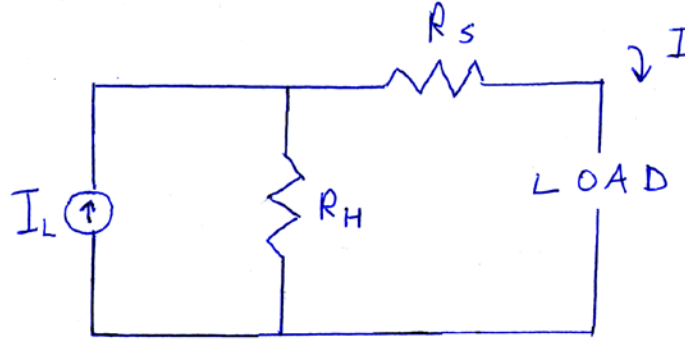
Figure 3.11. The very poor cell model. By applying the simplified diode model of Figure 3.10, we may simply remove altogether the diode from Figure 3.1.

By applying Kirchoff's rules to that model, we can obtain

$$R_H = \frac{V_{OC}}{J_L} \qquad\qquad [3.4]$$

$$R_S = \frac{(J_L - J_{SC})}{J_{SC}} R_H = \frac{(J_L - J_{SC})}{J_L J_{SC}} V_{OC} \qquad\qquad [3.5]$$

These equations may also be inverted to see the dependence of the second level metrics

on the resistances

$$V_{OC} = R_H \cdot J_L \qquad\qquad [3.6]$$

$$J_{SC} = \left(\frac{R_H}{R_H + R_S} \right) J_L \qquad\qquad [3.7]$$

Obviously, Equation 3.6 only applies if $R_H J_L$ is less than the ideal cell's V_{OC}.

Even in the case of very poor cells, only R_H affects V_{OC}. For reasonable cells, J_{SC} may be affected by R_S, but in the case of very poor cells, both R_H and R_S may have an influence.

We see by adding equations 3.4 and 3.5 together that the slope (which is now equal at short and open circuit) still has meaning

$$\frac{V_{OC}}{J_{SC}} = R_H + R_S \qquad\qquad [3.8]$$

We can call these equations collectively the very poor cell model. It is probably easiest to quickly reconstruct these equations from memory by memorizing Equations 3.6 and 3.8.

In those equations, J_L is the light induced current of a good (or ideal) cell, not the short circuit current of a real cell under consideration. For a CdTe cell, we might use a number similar to or slightly greater than 20 mA/cm^2, depending on the transmission of the substrate, the CdS thickness, and so on. V_{OC} and J_{SC}, however, are the parameters of the real cell, which are, for a very poor cell, presumed to be significantly lower than J_{SC}=20 mA/cm^2 and V_{OC}=800 mV.

It is also important in applying these equations to real cells to remember the assumption that parasitic resistance effects alone are decreasing J_{SC} and V_{OC}. In reality, as an example, poor light transmission in a substrate or TCO could reduce J_{SC} (and J_L) below what is expected. If the proper J_L is not used, R_S and R_H will not be estimated correctly.

What is the limit of these simple equations? Using the diode model, R_H may be solved exactly:

$$R_H = \frac{V_{OC}}{J_L - J_O(e^{\frac{qV_{OC}}{nkT}} - 1)} \qquad\qquad [3.9]$$

For our approximation to be valid, the second term in the denominator must be small in comparison to the first. Suppose J_L=20 mA/cm^2, n=2, and J_O was such that in a cell with no parasitic effects, V_{OC} would be 800mV. We would have a 5% error in R_H if the second term in the denominator was 1 mA/cm^2. This would be the case if, in the real

cell, V_{OC} would equal 650 mV. So, if V_{OC} would be less than 650 mV, we can treat the diode in the solar cell model as operating in the high resistance regime and our simple equations are valid. As a general rule of thumb, we can use the very poor cell equations when V_{OC} and J_{SC} are less than three-quarters of a good value and the fill factor equals 25%. This would take a decent CdTe cell of 11% to a very poor cell of 2%.

Incidentally, while R_H may be solved exactly from the diode equation, we are not so lucky with R_S, which requires (in the case of finite R_H) numerically solving a transcendental equation to obtain.

3.7 Further Reading

The section "Current-Voltage Analysis" in a paper by Hegedus and Shafarman[32] describes the solar cell equation and how to extract the various parameters (R_S, R_H, J_O, the ideality factor, etc.) from real solar cell data. Their method relies on a series of clever tricks and approximations, which are useful as it is difficult to directly fit (as with least-squares) the diode equation. However, they implicitly neglect R_S/R_H in our Equation 3.1 (giving their Equation 9), so their analysis does not completely apply to very poor cells.

The website http://pvcdrom.pveducation.org/ has various information on the solar cell circuit and equations, and the specific page

http://pvcdrom.pveducation.org/CELLOPER/BOTH.HTM

has an online Java simulator that calculates JV curves for a specific cell (ie., specific values of I_L, I_O, and n) but with various (user controlled) series and shunt resistances.

Chapter 4 – Series Resistance Theory and Experiment

4.1 Introduction

Though series resistance is an established metric for characterizing solar cells, the connection between sheet resistance and series resistance is still a subject for study[33]. The connection is often studied through simulations[34] or other complicated calculations.

To fully understand how series resistance affects real cells, not merely theoretical JV curves, and how it depends on transparent contact sheet resistance, we performed an experiment which showed a series resistance effect, and derived a simplified model that fit the data, but which is easier to work with than the full diode model,.

4.2 Experimental

Aluminosilicate glass (ASG) was used as a substrate. Zinc oxide doped with 2% by weight with aluminum (AZO), a transparent conducting oxide (TCO), was sputter deposited at 300°C and was used for the transparent top contact. CdS/CdTe layers were sputter deposited at 260°C. A CdCl$_2$ treatment was performed at 387°C for 30 minutes. Cu/Au layers were deposited as a back contact through evaporation. A heat treatment to diffuse the copper was performed at 150°C for 45 minutes, in air. The cell structure and layer thicknesses are shown in Figure 4.1.
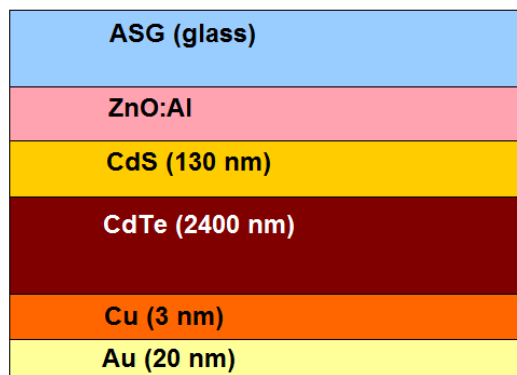
Figure 4.1. This is the cell structure used in this experiment. Light enters from above, through the glass. This is a typical cell structure used by our laboratory, and has given cell performance up to 14%.

All of those details are typical for our laboratory's solar cells. The key to this experiment is that half of the 3x3 inch substrate was completely coated with Cu/Au (the remainder of the substrate was used for small dot cells as a control in the event that the scribed cells did not function, which turned out not to be an issue). Within that region, cell areas were defined by laser scribing. The cells within that region were made to have areas in roughly geometric series (some large cells were measured first, then later divided into smaller cells). Indium was applied around the circumference of the cell as a negative electrode. The resulting cell in its final state is shown in Figure 4.2.
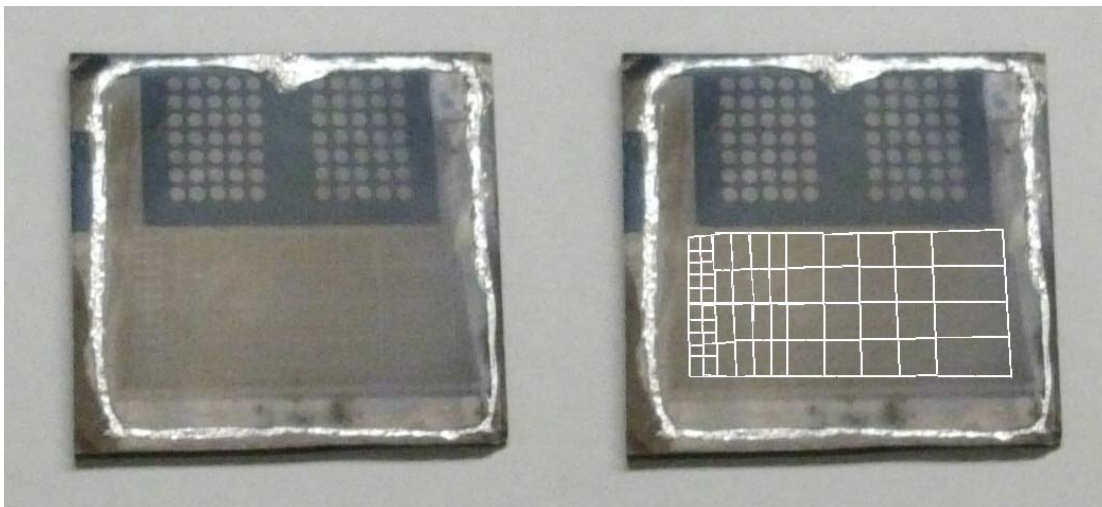
Figure 4.2 (left) The actual device used in this experiment. The upper half of the substrate has small circular cells which could be used as a control. The bottom half is completely coated with Cu/Au, which was then laser scribed to define the cell areas. (right) Because it is difficult to see the scribe lines in the image on the left, they have been traced over on a computer for the sake of visibility. Indium is soldered around the edge of the cell as a negative electrode.

4.3 Data

The resulting cells were measured, and their performance was quantified in terms of efficiency, open circuit voltage, short circuit current, and fill factor. These parameters were then plotted as a function of cell area. This data is summarized in Figure 4.3.
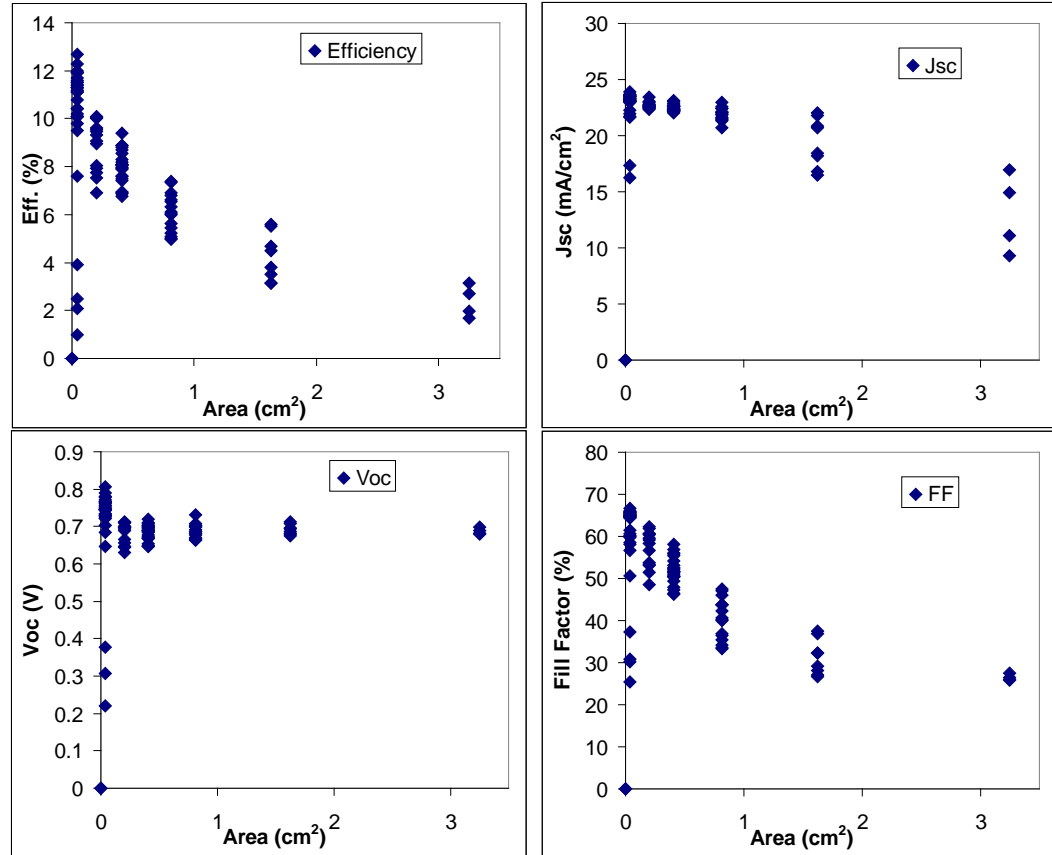
Figure 4.3. The performance of the scribed cells of variable areas, in terms of efficiency, short circuit current, open circuit voltage, and fill factor, as a function of cell area. Each data point represents a cell.

4.4 Discussion of Data

We see that open circuit voltage is nearly independent of cell area. Short circuit current shows little dependence on cell area for small cell areas, but decreases at large cell areas. Fill factor decreases immediately with increasing cell area until it reaches the straight line value of 25%.

By the previous chapter, these effects are indicative of a series resistance effect (if the series resistance increases with cell area). We will now attempt to explain the data

quantitatively, particularly fill factor, as the fill factor is the most strongly correlated

second level metric.

4.5 A Simplified Model for Series Resistance

As we have seen in the previous chapter, the full diode equation is difficult to

apply to experimental data as no closed form elementary expression for various

parameters, such as fill factor, may be derived from it. We therefore try to find a very

simple model.

A good solar cell should have low series resistance and therefore be very steep at

open circuit. However, a cell with significant series resistance will be sloped. This leads

us to consider a model JV that is flat, with J = -J$_{SC}$, until it hits a "knee" at V=M, then is a

straight line until V=Voc. See Figure 4.4.
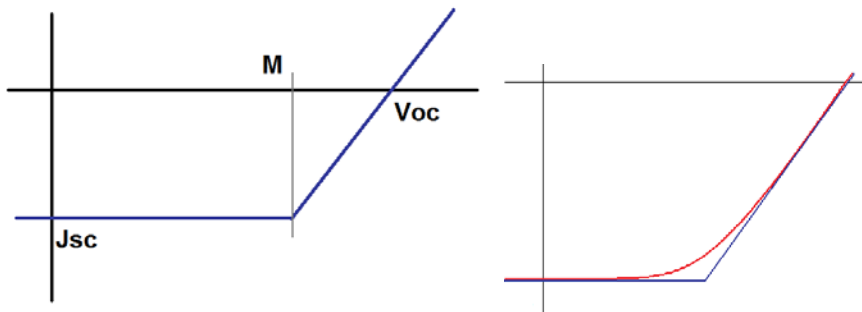
Figure 4.4. (Left) A simplified model of a JV curve. (Right) How our model
(blue) might compare to a real JV curve (red).

We note, first of all, that this model will usually represent a "best case scenario".

The fill factor predicted from this model will generally be less in reality because of the

curvature of the JV curve. We can worry about correcting for this later. In any case, the

first thing we want to derive is the maximum power point.

It is obvious that the maximum power point can *never* be left of the knee. See Figure 4.5. If we assumed the maximum power point was at the bottom right of the red rectangle, moving to the right adds the area of the pink rectangle. No area is subtracted. So, area (and power) continues to increase until we hit the knee.
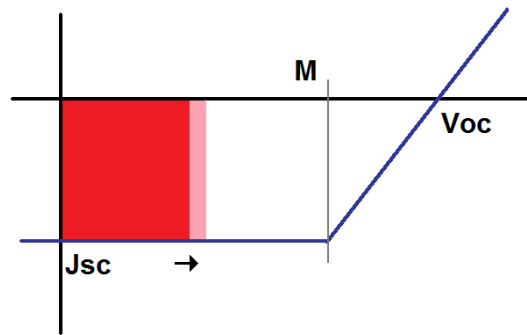
Figure 4.5. For any spot to the left of the knee, power can be increased by moving to the right.

However, it is possible the maximum power point could be to the right of the knee, on the sloped part of the curve. See Figure 4.6. As we move up the slope, we add the red area to the power, but subtract the orange. Whether a new point generates more power depends on the relative areas of the red and orange rectangles.
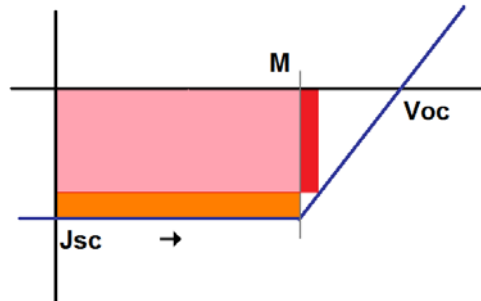
Figure 4.6 Past the knee, power may increase or decrease as we move towards open circuit.

93

In the previous chapter, we considered straight line JV curves, concluding that they have maximum power point always at Voc/2. We can apply this knowledge to our current model by extending the sloped section of the JV curve. See Figure 4.7.
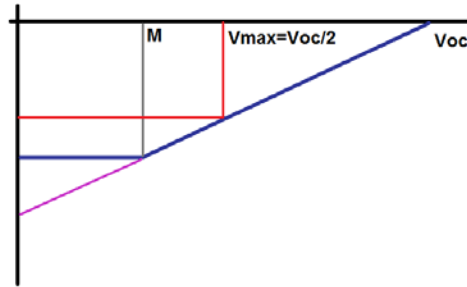
Figure 4.7. The model JV curve (blue) with hypothetical extension (purple). The maximum power point of the hypothetical curve is Voc/2, and with M<Voc/2, the maximum power rectangle (red) is completely contained in the model JV curve.

Though this extension may have different short circuit current and fill factor from our model curve, it still shares points in common.

The hypothetical extension has maximum power point at Voc/2. If this is greater than M, then it must have greater power than M (since M also exists on the sloped line). No other point on the sloped (or flat) part of the curve can generate greater power. Since the entire maximum power rectangle is contained within the model JV curve, this is also the maximum power point for our model curve.

If Voc/2 is less than M, then the maximum power rectangle (as well as simply the maximum power point) of the extended straight line JV curve would lie outside of our model curve. In that case, the maximum power point of our model curve would be M.

To summarize, the maximum power point is either Voc/2 or M, whichever is greater.

From that, we can calculate the fill factor.

$$FF = \frac{M}{Voc} \qquad\qquad , M > Voc/2 \qquad\qquad\qquad [4.1]$$

$$FF = \frac{Voc}{4(Voc - M)} \qquad , M < Voc/2 \qquad\qquad\qquad [4.2]$$

In the case that Voc/2=M, both expressions give FF=50%.

We can call the inverse of the slope of the sloped part of the curve the series resistance, and use that to eliminate M from the equations.

$$R = \frac{Voc - M}{Jsc} \qquad\qquad\qquad\qquad\qquad\qquad\qquad [4.3]$$

So

$$FF = 1 - \frac{J_{SC}}{V_{OC}} R_S, \qquad R_S \leq \frac{V_{OC}}{2J_{SC}} \qquad\qquad [4.4]$$

$$FF = \frac{V_{OC}}{4J_{SC}R_S}, \qquad R_S \geq \frac{V_{OC}}{2J_{SC}} \qquad\qquad [4.5]$$

We can improve these estimates by noting that, due to JV curve curvature, fill factor does not equal 1.0 when Rs=0. Rather, it might equal 0.7. On the other hand, 0.25 is the minimum fill factor predicted by those equations and in reality (so long as we use the real, not ideal, value of J_{SC} if R_S>=V_{OC}/J_{SC}). We can use the linear map that includes the points (0.25,0.25) and (1.0,0.7) (ie., $FF_{Corrected}$ = 0.6 $FF_{Original}$ +0.1) to correct the above equations. They then become

$$FF = 0.7 - 0.6 \frac{J_{SC}}{V_{OC}} R_S \qquad\qquad\qquad\qquad [4.6]$$

$$FF = 0.15 \frac{V_{OC}}{J_{SC}R_S} + 0.1 \qquad\qquad\qquad\qquad [4.7]$$

The equation for a solar cell with a series resistance but no shunt resistor (ie., infinite shunt resistance) is, again, in terms of current density

$$V = \frac{nkT}{q} \log\left[\frac{J_L - J}{J_O} + 1\right] - JR_S \qquad [4.8]$$

with the last term, $-JR_S$, the voltage drop caused by the series resistor. R_S is measured in ohm-cm^2. In terms of current (not current density), the voltage drop is equal to $-IR_{Eff}$, with R_{Eff} an effective resistance measured in ohms. $I=AJ$, with A the cell area, so the voltage drop $-IR_{Eff}=-(JA)R_{Eff}=-JR_S$, so $R_S=R_{EFF}A$. Now we need to find the effective resistance for dot cells.

4.6 The Effective Resistance for Dot Cells

First, we make a simplification. In the actual situation, the negative contact was square, the cell was square or rectangular, and the cell was positioned randomly. To simplify the situation, we assume a circular negative contact, a circular cell, and the negative contact and cell share centers. The circles have similar linear dimensions as the rectangles. See Figure 4.8.
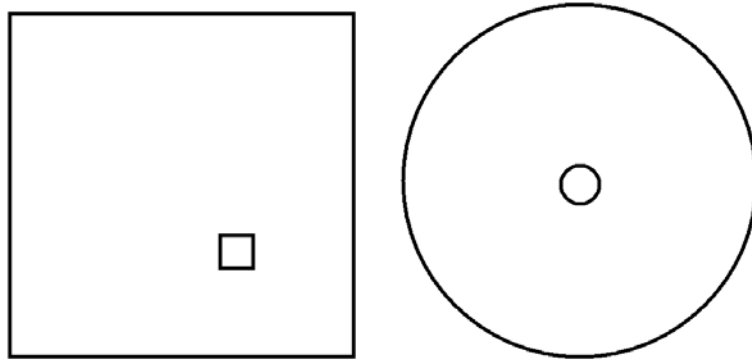
Figure 4.8. In reality (left), the cells are squares and randomly positioned on the substrate. In our model (right), everything is circular and share centers.

The series resistance is controlled by the TCO; presumably, the metal bottom

contact is much more conductive. The TCO could be described by two parameters: The

resistivity ρ, or the sheet resistance, R_{SHEET}, which is the resistivity divided by the film

thickness, $R_{SHEET}=\rho/t$. The correct unit for sheet resistance is ohms; however, it is often

written as "ohms per square", "square" being sort of a pseudo-unit like radians or

"cycles" when using hertz (that is, it is like a pure number that carries no units). The

reason ohms/sqr. are often used is that the resistance of any *square* (regardless of

dimensions) on a film has constant value equal to the sheet resistance. See Figure 4.9 for

a derivation.
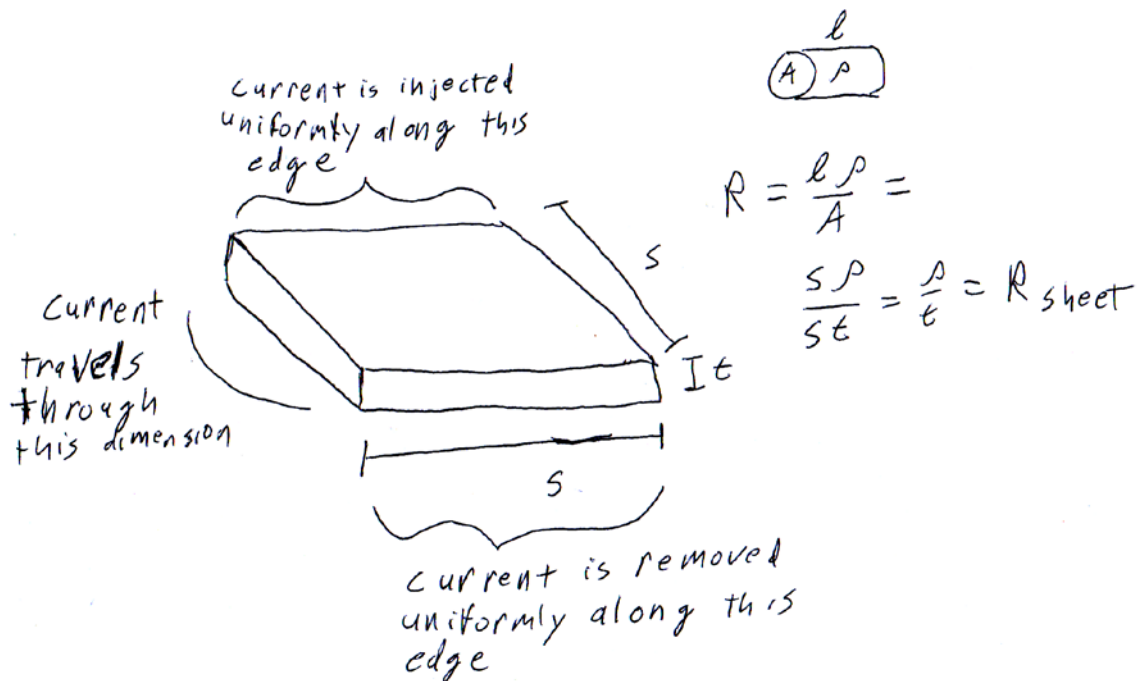
Figure 4.9. Derivation of the resistance of a square. Current is uniformly injected and removed from opposite edges of a square This could be done by using linear contacts of length s that are much more conductive than the underlying film. The resistance of any wire of length l and cross sectional area is the resistivity times the length and divided by the area. For this case, the length is s and the area is st. s cancels and we are left with the sheet resistance.

If current is injected at a point in a thin TCO film that is large in lateral dimensions, then at a distance from the injection point that is large in comparison with the thickness of the film the current will (by symmetry) spread out cylindrically (with height equal to the film thickness t) so that points equidistance away from the injection point have equal current density. See Figure 4.9.
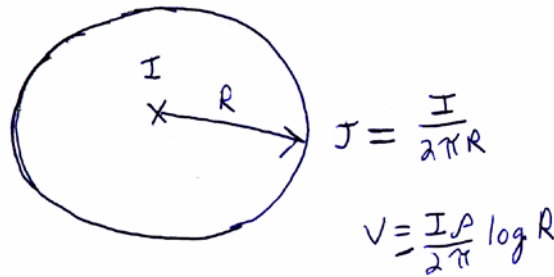
Figure 4.10. In two dimensions (which represents a thin film with large lateral dimensions), current injected at a point will spread circularly.

By using the same considerations that are used when using Gauss's law in undergraduate physics courses, the current density is

$$J(R) = \frac{I}{2\pi R t} \tag{4.9}$$

The fundamental definition of resistivity is

$$\vec{E} = \rho \vec{J} \tag{4.10}$$

We can integrate that to find the voltage as a function of distance from the injection point.

$$V(R) = -\frac{IR_{SHEET}}{2\pi} \log(R) \tag{4.11}$$

Although that is the true sign for the voltage, we can afford to be cavalier with our minus signs on such voltages in this chapter, as we will eventually divide them all by current to get resistances, which will always be positive.

As a side note, this is the principle that is used to measure sheet resistance with the four-point-probe measurement. Four probes are in a straight line, with a distance s between consecutive probes. A current I is injected at the far left (for example) probe and is removed by injecting a current –I at the far right probe. Then the potential at the middle left probe will be $-\frac{IR_{SHEET}}{2\pi}\log(s) + \frac{IR_{SHEET}}{2\pi}\log(2s) = \frac{IR}{2\pi}\log(2)$, which is independent of the probe spacing. Similarly, the potential at the middle right probe will be the negative of that value. The voltage difference between the middle probes is then

$$V = \frac{I\rho}{\pi t}\log(2) = \frac{IR}{\pi}\log(2).$$ [4.12]

That voltage difference divided by the current (which can be found by measuring the voltage across a resistor in series with the current injecting circuit) is the sheet resistance times a geometrical factor.

In any case, we can apply similar principles and equation 4.11 to our geometry.

We assume that the cells are uniform, so that equal current density is injected at every point within the cell. This current density is of course $\frac{I}{\pi x^2}$, with I the total current generated by the cell and x the cell radius. We first consider the voltage drop inside the cell. In reality, because the TCO will be at different voltages at different locations under the cell, the single diode model from the previous chapter may not apply. A distributed diode model with distributed series resistances might be more appropriate. We ignore

this for now in the interest of simplicity. We will briefly discuss a distributed diode

model later.

Consider a point at radius y inside the cell. See Figure 4.9. The total current

inside the cell up to that point is $I\dfrac{y^2}{x^2}$. To find the current density at that point, we

assume that total contained current was injected at a concentrated point at the center of

the cell; then the current density is $I\dfrac{y}{2\pi x^2}$. By integrating that from zero to x and

dividing by the current, we find the effective resistance for moving current from the

inside of the cell to the edge is $\dfrac{R_{SHEET}}{4\pi}$. It is perhaps surprising that this does not depend

on the dimension of the circle, though it is maybe less surprising when we remember that

squares also have resistance independent of dimension.

$$I_{in}(y) = \frac{I\pi y^2}{\pi x^2} = I\frac{y^2}{x^2}$$

$$J_{at}(y) = \frac{I_{in}}{2\pi y} = \frac{I y}{2\pi x^2}$$

$$V(y) = \int_0^Y \rho\, J_{at}(t)\,dt = \frac{I \rho y^2}{4\pi x^2}$$
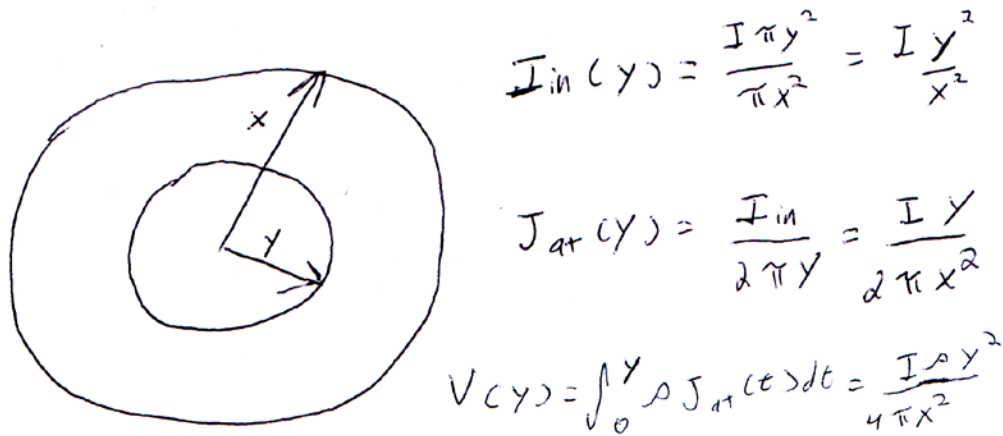
Figure 4.11. A derivation of the effective resistance in moving current
which is uniformly injected in a circle to the edge of the circle.

To find the resistance from the edge of the cell to the edge of the negative

electrode (which we say is a distance D from the center of the cell) is easy. Since we can

100

treat the current as though it is centered at the center of the cell, the potential at the

negative contact is $I\dfrac{R_{SHEET}}{2\pi}\log(D)$ and the potential at the cell edge is $I\dfrac{R_{SHEET}}{2\pi}\log(x)$

and the effective resistance between the two points is $\dfrac{R_{SHEET}}{2\pi}\log(\dfrac{D}{x})$. Note that the

effective resistance between the cell edge and negative electrode *decreases* with

increasing cell size, simply because the two points are getting closer. Even though the

effective resistance may decrease, the resistive losses will increase with increasing cell

size, because the current that passes through that resistor will increase.

The total effective resistance in our system is then

$$R_{EFF} = \frac{R_{SHEET}}{2\pi}(\log(\frac{D}{x})+\frac{1}{2})$$
[4.13]

Because the dependence on cell size is logarithmic and slowly varying, it may sometimes

be possible to use a constant value of effective resistance. In our situation, where the

contact is several centimeters in diameter while the cells are on the order of millimeters

in diameter, the effective resistance may often be about half the sheet resistance.

However, since we took the trouble to derive the full equation, we might as well use it.

4.7 First Comparison of Theory to Experiment

We compare the fill factor data from Figure 4.3 to the model in Figure 4.12. As

seen, the agreement between the performance of the best cells for given area and the

model is excellent. In the model, we used a sheet resistance value of 30 ohms/sqr. to

describe the ZnO. We used that value as a parameter rather than an experimental value

due to the sheet resistance change in ZnO during cell fabrication, which will be described later.

We do not, at this time, attempt to explain the performance of cells which are not the best. Other parasitic effects, which may be stochastic, can reduce cell performance below the point that series resistance has.
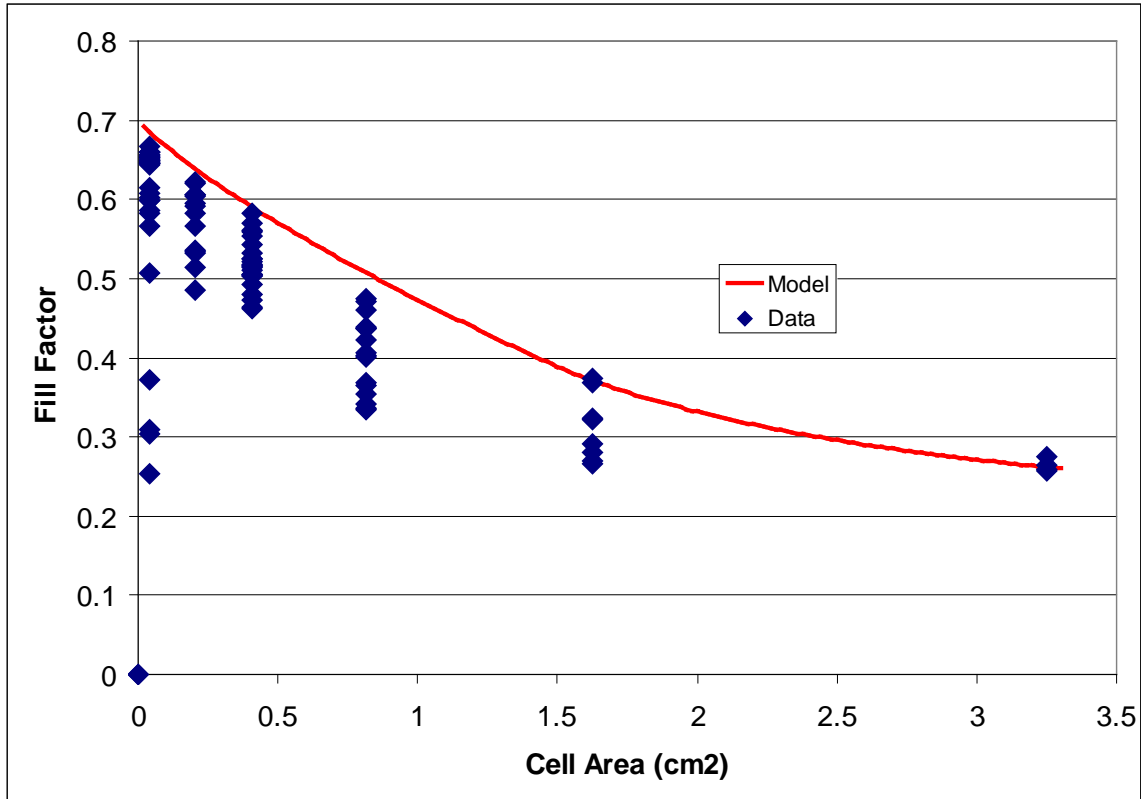
Figure 4.12. A comparison of the data from Figure 4.3 to the model we derived. It is seen that the model describes the best cells of a given area excellently.

4.8 Second Comparison of Theory to Experiment

Due to using the sheet resistance as a parameter in the previous section, we desired also to test Equation 4.13, the dependence of effective resistance on sheet

resistance. To that end, rather than using ASG with AZO, we fabricated cells on

Pilkington Tec15 which has, as its name implies, a nominal sheet resistance of 15

ohm/sqr. (This value may vary by a few ohms; we measured with four point probe one

piece of Tec15 as having 13.5 ohm/sqr. sheet resistance). To have cells of different area,

we simply used, when depositing the Cu/Au bottom contacts, a mask with different areas

cut in it.

The basic cell parameters are shown in Figure 4.13.
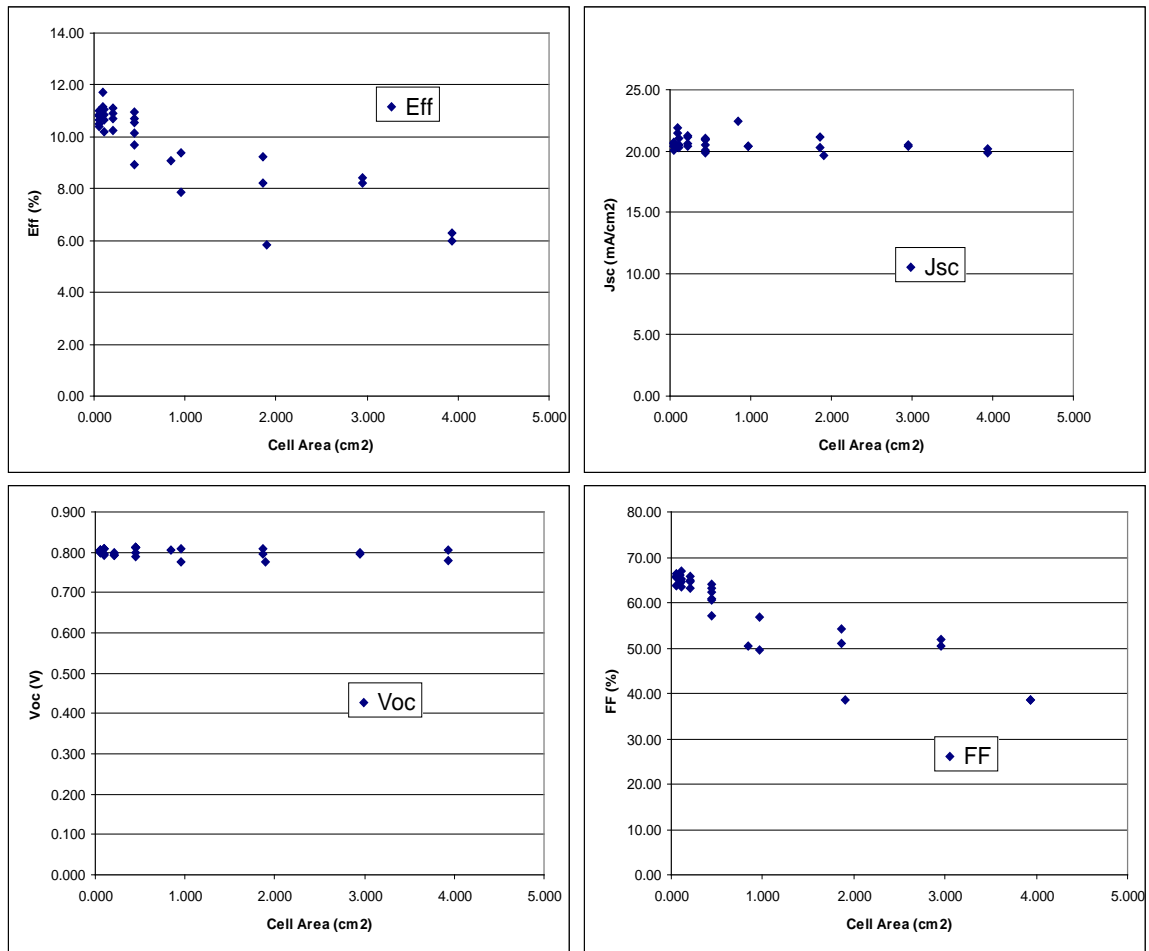
Figure 4.13. The first and second metrics of the second series
resistance experiment, on Tec15.

The general traits in Figure 4.13 are similar to the traits in Figure 4.3. The biggest difference is that apparently the series resistance effect is smaller (which makes sense, comparing 15 ohm/sqr. to 30 ohm/sqr.) as Jsc is not noticeably decreasing even for large cells, and the slope of the decrease of fill factor with cell area is less steep.

We compare the fill factor data with our model in Figure 4.14.
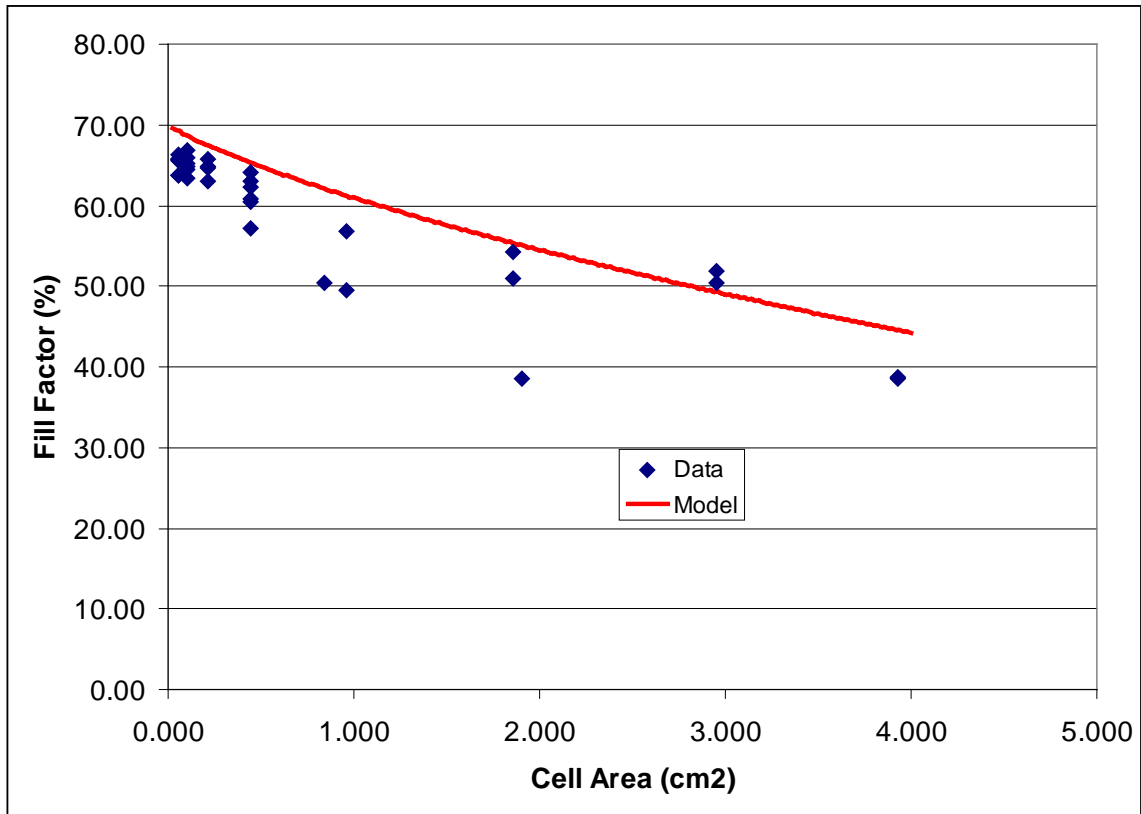
Figure 4.14. The comparison of our model to data for the second series resistance experiment, on Tec15.

The slope of the model corresponds well to the slope shown in the data, indicating that our calculations to determine effective resistance from sheet resistance are applicable.

4.9 Comparison to a Different Model for Fill Factor

When our data were first taken, we derived a model to explain it. However, Martin Green had already proposed a closed form formula for the dependence of fill factor on series resistance:

$$FF = FF_O(1 - 1.1r_S) + \frac{r_S^2}{5.4}$$

[4.14]

FF_O is the original fill factor, without any resistive losses. r_S is the series resistance made unitless by dividing by the cell's "characteristic resistance"

$$r_S = R_{SERIES} \frac{I_{SC}}{V_{OC}}$$

[4.15]

The odd factors like 5.4 are semi-empirical.

Figure 4.15 compares both models to the fill factor obtained numerically from the full diode equation, using the parameters to create Figure 3.2 (and most of the figures from the previous chapter). Because the ideal cell had fill factor 78.4% rather than 70%, we adjust the linear map correction for our fill factor model accordingly.
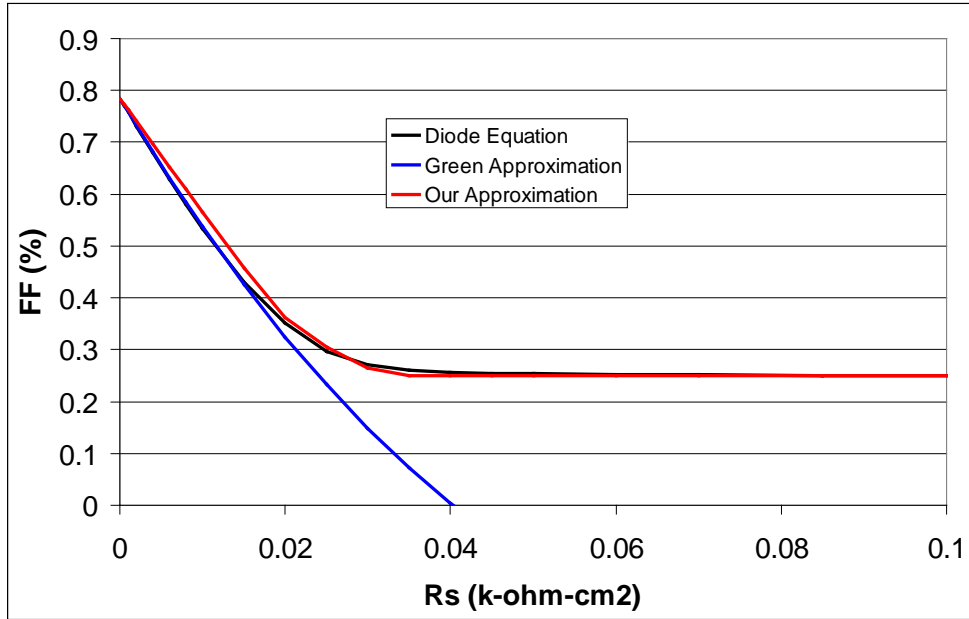
Figure 4.15. Comparison of our model to another model and the results from the exact diode model.

Our model follows the results from the diode equation fairly well over the full range (of course, it is a form of extrapolation between two exact limits). However, Green's model, with the flexibility afforded by semi-empirical parameters, fits the diode equation results almost perfectly down to a fill factor of about 40%, at which point it fails completely.

4.10 Distributed Cell Elements

We mentioned that since the TCO under the cell is not at the same potential, the notion of treating the entire cell by a single diode is a simplification. We'll explore that idea qualitatively a little bit here. We still wish, however, to keep things as simple as possible.

We can imagine dividing the cell into two regions (probably based on radius – of course, we could also simply imagine a cell with extent in one dimension). Figure 4.16 (left) shows a physical model of the situation. The light induced currents I_L^1 and I_L^2 will be proportional to the areas of the two regions, based on where we decided to put the dividing radius. The resistance between the center of the cell and the negative electrode is R_1+R_2, but we can divide the total resistance into resistances between the various regions.
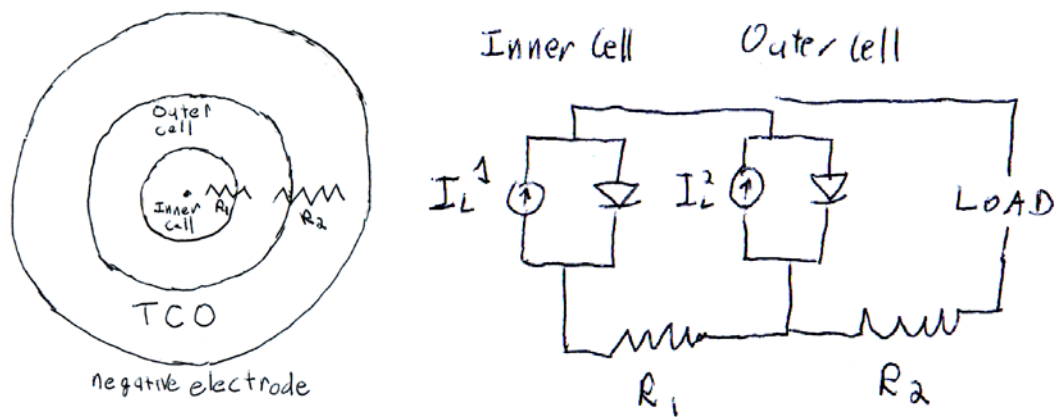
Figure 4.16. A model for considering a solar cell as distributed diodes, as a consequence of the TCO under the cell being at different potentials. (Left) A physical model. (Right) A schematic model based on the physical model.

In the interest of keeping things simple, we will not treat the diodes in Fgure 4.14 as having exponential behavior. Rather, we will treat them as rectifying: They may either be "off" and have infinite resistance, or be "on" and have a voltage drop of W across them, and allow any amount of current to flow through them, so long as the current is in the forward bias direction (as in Fgure 3.10). We will assume both diodes are identical (that is, both have equal voltage drops of W when on).

There are three regimes for this model:

1) Both diodes are "off". In this case, the current through the load is $I_L = I_L{}^1 +$ $I_L{}^2$, independent of the voltage on the load. This is the flat part of the current-voltage curve, and is identical to the single diode model.

2) The inner diode is "on" and the outer diode is "off". We find that the equation describing this regime is

$$I = \frac{\left(W + I_L^2 R_1 - V\right)}{\left(R_1 + R_2\right)}$$

3) The outer diode is "on". The equation describing this regime is

$$I = \frac{\left(W - V\right)}{R_2}$$

This is similar to the sloped region of our model, if we used only R_2 as the series resistance. Perhaps initially surprisingly, this equation will be followed if the outer diode is on, regardless of any details of the inner diode. We can partially understand the lack of dependence on the inner diode by considering that open circuit voltage, unlike short circuit current, does not depend on cell area (at least in an ideal case).

For the sake of building intuition, we demonstrate two examples. Both use diodes with $I_O=1 \times 10^{-14}$ A and n = 1, and $I_L{}^1=I_L{}^2=0.01$ A. These numbers are chosen simply due to the ease of working with them and are not necessarily intended to represent CdTe cells. For our model, these diodes would correspond to W=0.69 volts.

Figure 4.15 shows the case that $R_1=R_2=25$ ohms. The exact diode curves were calculated with the analog circuit simulator at http://www.falstad.com/circuit/. Due to our calculation treating the light induced current as positive, this graph is plotted with the convention that power is generated in the first quadrant.
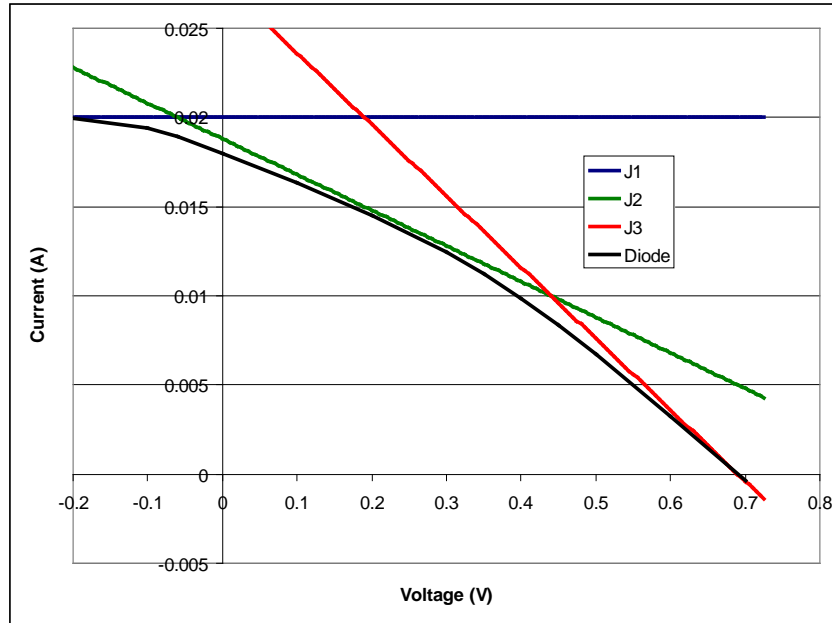
Figure 4.17. The distributed diode model in the case that W=.69V, $I_L^1=I_L^2$=10mA, and $R_1=R_2$=25 ohms. This graph uses the convention that light induced current is positive and power is generated in the first quadrant.

What is interesting about that example is that the JV curve (including the "real" diode curve) seems to have two distinct slopes, at short and open circuit. If one did not know what model was used to generate the curves, one might suppose the two distinct slopes imply the cell has both a series and shunt resistance problem. In fact, when the inner diode is on while the outer is off, the inner diode does act kind of like a shunt for the cell.

Figure 4.16 shows the case that $R_1=R_2$=10 ohms. In this case, if one were to look merely at the exact diode curve, one would probably suppose that this was simply a case of a cell that could be characterized by a single diode and single series resistance. We believe this is the case for the cells we have described in this chapter, which is why the model fit the data so well without considering distributed cells.

109
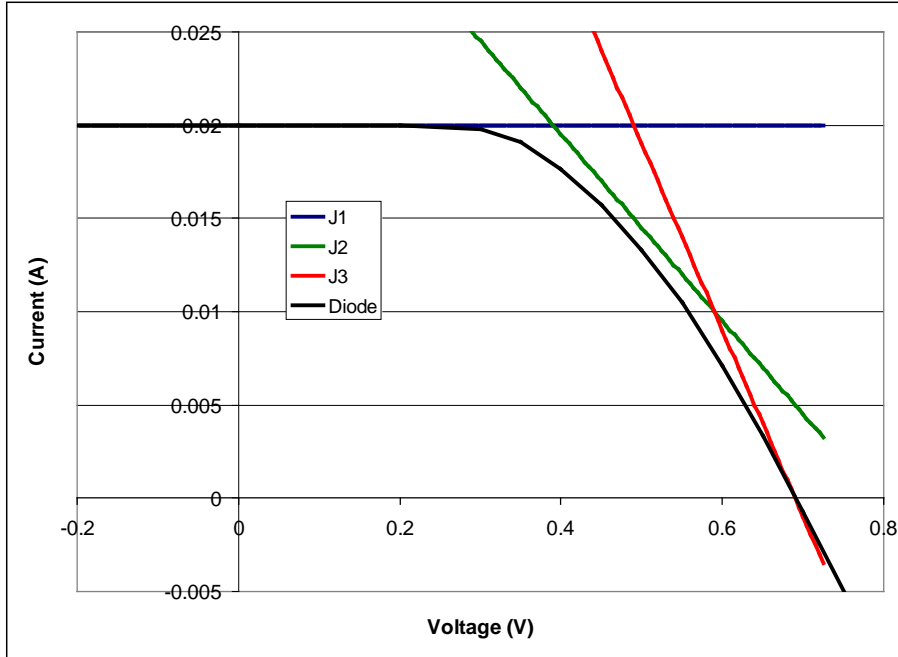
Figure 4.18. The distributed diode model in the case that W=0.69V, $I_L^1=I_L^2=10mA$, and $R_1=R_2=10$ ohms. As in Figure 4.15, this graph uses the convention that light induced current is positive and power is generated in the first quadrant.

Presumably for more resistive TCO layers, effects caused by the TCO under the cell being at different potentials would have a larger effect.

Our treatment here has been simple and qualitative. The distribution effect was treated comprehensively by Karpov et al.[35], who defined a screening length $L = \sqrt{\dfrac{2V_{OC}}{\rho J_{SC}}}$. In a small cell regime, in which the cell's linear dimensions are small compared to the screening length, distributed effects may be ignored so long as the cell is below open circuit voltage (which will be the case where fill factor is determined). For the data in Figure 4.12, the screening length would correspond to a cell dimension of 2.8cm^2. As most of the data in Figure 4.12 is for cells of smaller areas, we see why we were able to ignore the variable potential of the TCO under the cell.

110

The examples shown are not the only possible ones. For example, with the other numbers the same, if $R_1=R_2>70$ ohms, then the curve $I=(W-V)/R_2$ would be the only one that would apply anywhere in the power quadrant.

4.11 Conclusion

There is excellent agreement between our models and data. This agreement shows we have the understanding needed to control final device performance in terms of series resistance. It also may deserve emphasis that the model herein can be applied to dot cells in a geometry as we typically make them; a special cell geometry to make the calculation more convenient was not used.

We also suggest that this method has potential utility as a routine diagnostic. It provides extra information on cells from JV measurements with little extra effort. It would be simple to always use masks with a selection of cell areas, and to use a negative contact which is a ring around the entire device. Graphing cell area versus fill factor is usually trivial. The mathematics in this chapter is fairly simple, with most being able to derive on scrap paper (especially if the approximation $R_{EFF} \sim R_{SHEET}/2$ is used rather than Equation 4.13), which also lends this method to use as a routine diagnostic.

We would expect if this method were to be used routinely with Tec15 that it might result in similar results each time. However, there are at least two circumstances where this routine would be especially useful: If the TCO is unstable, or if direct measurement of TCO properties would be difficult. Both of these may apply to flexible cells. The instability of our TCO is discussed in Chapter 6. Direct measurement of TCO sheet resistance by four point probe can be difficult on polymer, as the probes may puncture the polymer and TCO.

Chapter 5 -- HRT Model

5.1 Introduction

Highly resistive and transparent (HRT) layers have been used experimentally to counteract the effect of shunts and to improve device uniformity and yield[36,37]. These layers, in the cell structure, are generally between the TCO and the n-type heterojunction partner (which would be CdS for either CIGS or CdTe). In this chapter, we consider a model of an HRT layer that allows determination of the optimal parameters of the layer to counteract particular shunts.

5.2 First Considerations

We imagine a model of a solar cell with an HRT in Figure 5.1. The left side is a rough physical model of the cell. The active part of the solar cell is in position A. There is a shunt at B. We could imagine that some of the CdTe has flaked off there or a pinhole has developed and gold (which is represented by the wire at the top of the image) has contacted the HRT directly. C is the TCO below the HRT (the image is inverted with regards to the usual convention that sunlight enters from above). We assume that the TCO is so conductive, at least compared to the HRT, that it can be modeled by an equipotential wire like the gold.

Obviously, simplifications have been made here, particularly, again, that the entire active cell is represented by a single diode and current source, when we would realistically expect areas of the cell closest to the shunt to be most affected by the shunt.
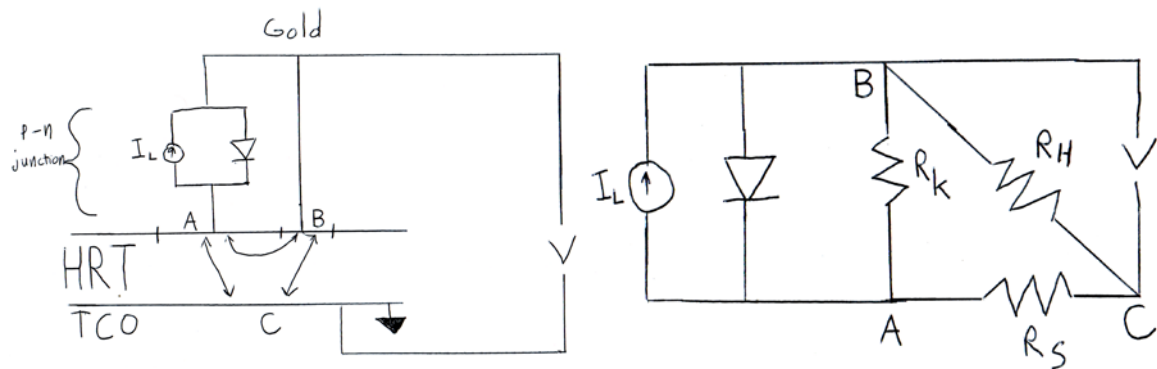
Figure 5.1. A model of an HRT in a solar cell. (Left) A semi-physical model of a solar cell with a shunt. (Right) The model on the left converted to a purely schematic model.

We see that there are three paths for current to flow within the HRT: From the cell to the shunt (A to B), from the cell to the TCO / load (A to C), and from the shunt to the TCO / load (B to C). Therefore, we can model the HRT schematically as three resistors, as shown on the right of figure 5.1. If the three resistors were specified, the solar cell performance could be exactly characterized.

5.3 Boundary Conditions

If we had the Green's function of the HRT, we could in principle calculate any desired electrical property of it.

We remember that the continuity equation is

$$\frac{\partial \rho}{\partial t} + \nabla \bullet J = 0 \qquad \qquad [5.1]$$

The time derivative of the charge density is zero (no charge will accumulate anywhere

when current is injected), so the divergence of the current density is zero.

$$\nabla \bullet J = 0 \qquad \qquad [5.2]$$

This is Gauss's Law, with current density substituted for electric field. This means we

can use methods we already know from electrostatics. We do, however, need to find the

new boundary conditions when using J rather than E.

To that end, we imagine material made of a two layers of two different materials

put in series with a voltage. See Figure 5.2. If the boundary between the two materials is

perpendicular to the path of current flow, then the two materials act like two resistors in

series. The current that flows through both materials must be the same. Therefore, the

component of current density that is perpendicular to an interface is continuous.
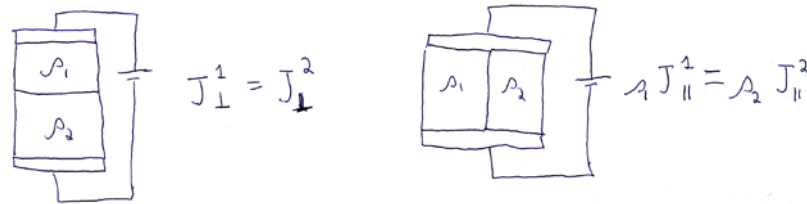
Figure 5.2. Derivation of the boundary conditions for
current.

If the boundary between the materials is parallel to the path of current flow, the

two materials act like resistors in parallel. The current through a resistor in parallel is

inversely proportional to the resistance of the resistor. If the two regions were of equal

dimensions, this would obvious imply the current densities would also be inversely

proportional to the resistances. If one region had a larger cross sectional area, then the current through it would increase, but the current density would correspondingly decrease by the same factor. Therefore, for all situations, the current density components obey the boundary conditions:

$$J_1^{\perp} = J_2^{\perp} \tag{5.3a}$$

$$\rho_1 J_1^{II} = \rho_2 J_2^{II} \tag{5.3b}$$

5.4 Green's Function of a Thin Conducting Film

Now that we have a path for finding Green's functions, we apply our methods to a situation similar to an HRT, but slightly different – one that is easier to confirm the final results with intuition to verify our calculation methods: A thin conducting film. We could imagine a two- or three-dimensional case. In either, the film is of finite thickness t in one dimension, but of infinite extent in the remaining one or two dimensions. We suppose a current is injected into some point (which we might as well consider the origin) at the top of the film.

No current can flow out of the film. For a real-life comparison, a conducting film could be deposited on an insulated substrate such as glass. No current will flow into the glass, or, on the other side of the film, into the air.

Since the current is zero on the other side of the boundary, by the boundary conditions derived in the previous section, the component of the current density perpendicular to the boundaries must be zero. In other words, the current density J must be parallel to the boundaries. See Figure 5.3.
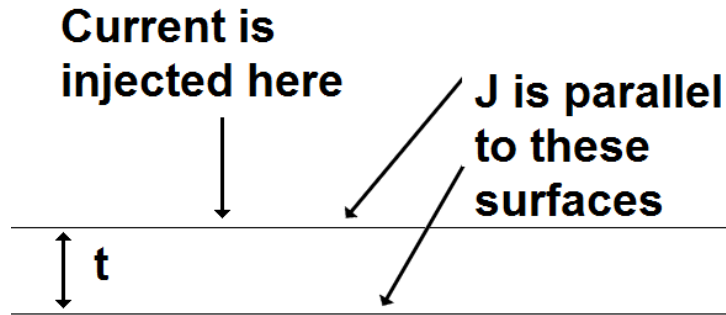
Figure 5.3. The boundary conditions as applied to a thin conducting film. The film is viewed edge on.

The boundary condition on the upper surface is already satisfied with current injected at one point on it. The current will spread radially from the injection point.

We can satisfy the boundary condition on the other surface with an "image current", just like an image charge in electrostatics. Use of image currents to correct boundary conditions has precedence in the theories relating to four point probe measurement[38]. Current is parallel to a plane if two current sources are of equal magnitude and equal distance from the plane. See figure 5.4. What is physically happening is the law of reflection. If current seems to come from the upper source, it will reflect off the interface and from then on seem to come from the bottom source. Compare to electrostatics and a grounded plane: In that case, the different boundary conditions will have image charges also of equal distance from the plane, but of opposite signs.
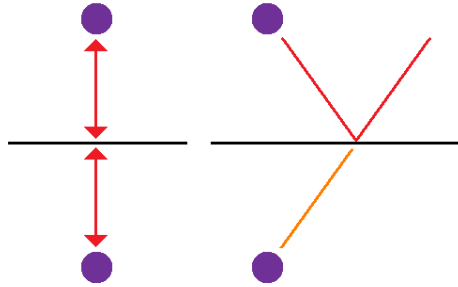
Figure 5.4. (left) If two point current sources (balls) are of equal magnitude and of equal distance from a plane (or line in 2D), the resulting current density will be parallel to the plane at the plane. (right) A physical interpretation would be, if the interface was real and current seemed to come from the upper current source, after reflection, the current will seem to come from the lower current source.

We need to develop a series of image currents. See Figure 5.5. As we remarked, with merely the original current source, the boundary condition is satisfied on the top surface. With one image current, the boundary condition is satisfied on the bottom surface, but is no longer satisfied on the top surface. With an additional image current, the condition is satisfied on the top but not bottom. However, although the surface the condition is satisfied on alternates, each time a new image current is added, the boundary with the "wrong" condition becomes less wrong with each new image, as the images become farther away and have less of an impact.
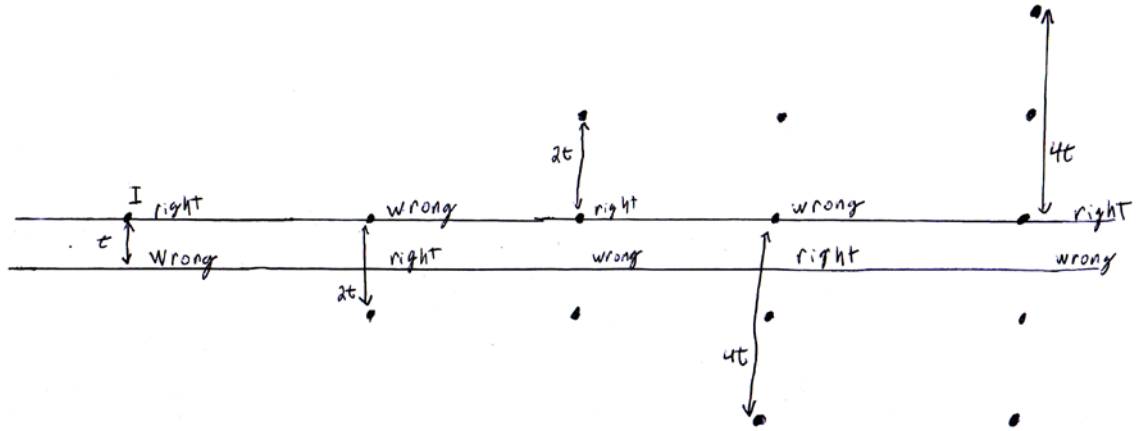
Figure 5.5. Development of image currents for a thin conductive film. Each point current source is represented by a point. The words "right" or "wrong" applied to a surface indicate whether the boundary conditions are met on that surface with the given configuration of current sources (real and image). As mentioned, with only the original current source (far left), the boundary condition is met on the top surface. As image currents are added (moving to the right), the surface that has correct boundary conditions alternates. Though the bottom surface has the wrong boundary conditions on both the far left and far right, they are less "wrong" on the far right since the perturbing sources are farther away.

In 3D, the current injected in semi-infinite space will expand in that space like a semi-sphere (similar, of course, to the electric field emanating from a point charge). This tells us the current density goes as the reciprocal of the surface area of the semi-sphere, 1 over r-squared. The potential will go as 1 over r. We can immediately try to write the potential from the series of image currents.

$$V = \frac{I\rho}{2\pi}(\frac{1}{\sqrt{z^2+r^2}} + \frac{1}{\sqrt{(2t+z)^2+r^2}} + \frac{1}{\sqrt{(4t+z)^2+r^2}} + ...$$

$$+ \frac{1}{\sqrt{(2t-z)^2+r^2}} + \frac{1}{\sqrt{(4t-z)^2+r^2}} + \frac{1}{\sqrt{(6t-z)^2+r^2}} + ...$$

[5.4]

z is the coordinate along the finite dimension; r is along the infinite dimension. The situation has cylindrical symmetry around the injection point.

However, at z=t, r=0 (the face opposite the current injection point) this becomes

118

$$V = \frac{I\rho}{2\pi}(\frac{1}{t} + \frac{1}{3t} + \frac{1}{5t} + ... + \frac{1}{t} + \frac{1}{3t} + \frac{1}{5t} + ...)$$

[5.5]

In other words, it becomes the harmonic series, which diverges. This is an unphysical

result. We can correct this by remembering that V can be adjusted by a constant, so we

may add a constant of integration to each term to make each term (and thus the sum) zero

at z=t, r=0.

$$V = \frac{I\rho}{2\pi}\sum_{a=0}^{\infty}\left(\frac{1}{\sqrt{(2at+z)^2 + r^2}} + \frac{1}{\sqrt{(2(a+1)t - z)^2 + r^2}} - \frac{2}{(2a+1)t}\right)$$

[5.6]

As r tends to infinity, this becomes

$$V = \frac{I\rho}{2\pi}\left(-\frac{2}{t} - \frac{2}{3t} - \frac{2}{5t} - \frac{2}{7t} - ...\right)$$

[5.7]

Again the harmonic series; V again diverges. Is *this* physical?

   Far from the injection point, the situation as we described it is basically two

dimensional. The current will no longer be expanding like a semisphere, but will be like

a cylinder of height t. This means the current density will go as 1/r, so the potential will

go as the logarithm. For the potential to be finite at any finite point, the potential must

diverge as r goes to infinity.

   Figure 5.6 shows a trace of the potential, calculated numerically from the infinite

series, at z=0. The x-axis is the r dimension. t was set equal to 1. It may be seen how

the exact potential has a 1/r form when r<<t, near the injection point, but behaves like a

logarithm when r>>t.
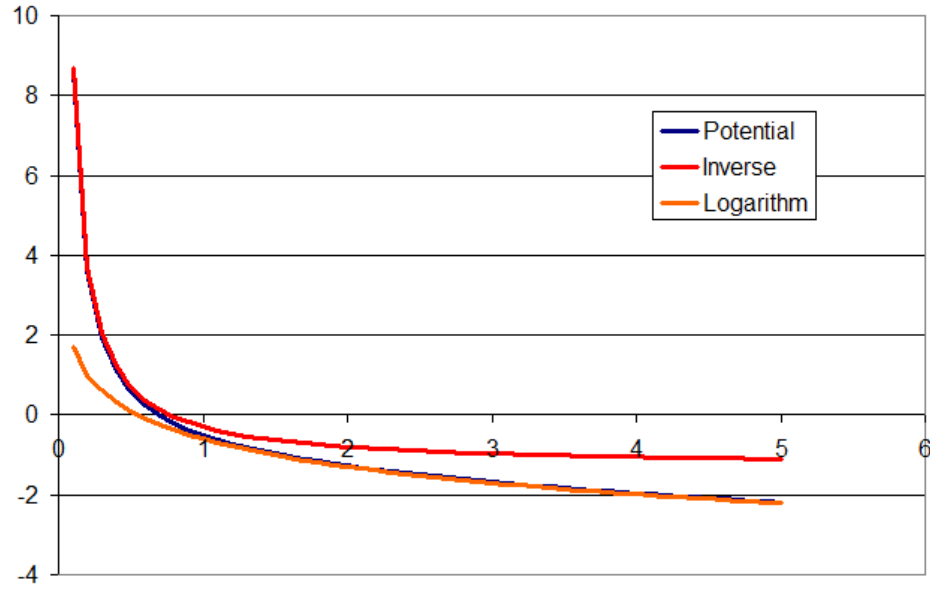
Figure 5.6. The potential at z=0 as a function of r for a thin conducting film. When r<<t, the potential has 1/r behavior; when r>>t the potential has logarithmic behavior.

Although we used an infinite series to calculate the potential, that does not tell us *a priori* that the potential couldn't be calculated in terms of elementary functions. However, if the potential could be calculated, so could the current density, at all points. But for the special condition that r=0, z=1, t=2

$$J(r = 0, z = 1, t = 2) = \frac{I\rho}{2\pi}(\frac{1}{1^2} - \frac{1}{3^2} + \frac{1}{5^2} - \frac{1}{7^2} + ...) = \frac{I\rho}{2\pi}K \qquad [5.8]$$

Where K is Catalan's Constant, which has resisted simplification to elementary constants and functions for over 200 years, at least since Euler found the sum in the case that the odd reciprocal squares were all added rather than alternatingly added and subtracted.

Our method for calculating the potential of a thin conducting film has led to a result which may be verified as reasonable through intuition. Thus emboldened, we now proceed to an HRT.

5.5 An Arbitrary Bilayer

We can start by first considering any arbitrary bilayer. See Figure 5.7. The situation is very similar to the classic electrostatics problem of finding an electric field caused by a point charge near a planar dielectric discontinuity.
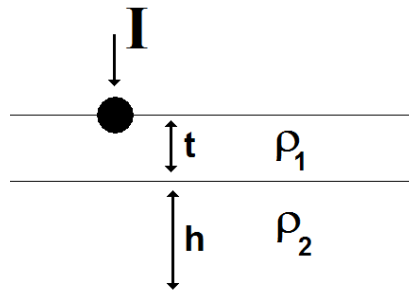
Figure 5.7. The situation of current injected into a bilayer. The top layer has thickness t and resistivity ρ_1 while the bottom layer has thickness h and resistivity ρ_2. The resistivity of whatever is above and below these layers (probably air on top and an insulating substrate on the bottom) is considered infinite.

We again use the image current method. We first try to "fix" the boundary between the two materials. See Figure 5.8. To describe region 1, we introduce an image charge in region 2, but equidistant from the boundary as the original current. To describe region 2, we alter the value of the original current.
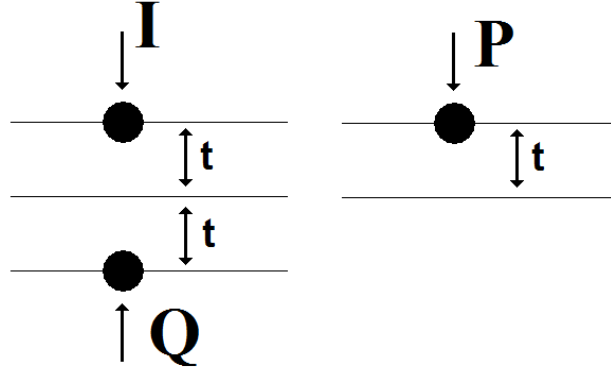
Figure 5.8. Applying the method of images to a bilayer. The first step, for region 1 (left), is to introduce an image current Q in region 2. For region 2 (right), we alter the value of the original current.

We can apply the boundary conditions in Equation 5.3 to the situation in Figure 5.8. Remember that the method of images causes us to consider region 1 as entirely filled with ρ_1 while region 2 is entirely filled with ρ_2. Applying the boundary conditions gives

$$I - Q = P \qquad [5.9a]$$

$$\rho_1(I + Q) = \rho_2(P) \qquad [5.9b]$$

These equations may be solved to give

$$Q = \left[\frac{\rho_2 - \rho_1}{\rho_2 + \rho_1}\right] I \qquad [5.10a]$$

$$P = \left[\frac{2\rho_1}{\rho_2 + \rho_1}\right] I \qquad [5.10b]$$

We could continue to develop more and more image charges to correct the various boundaries. However, in this case, each time we correct a boundary, the quantity of the image charges multiply. Therefore, we find that trying to find the Green's function for a bilayer to be tedious and not worthwhile. To make the problem easier for the HRT

case, we assume the TCO under the HRT is so much less resistive that we may set ρ_2

equal to zero. Then

$$Q = -I \qquad\qquad [5.11]$$

We don't care much what P is, since we won't bother finding the potential inside the

TCO (since it has zero resistivity, it's an equipotential), but it has the convenient value

that P=0. This prevents the image currents from multiplying.

5.6 The HRT Green's Function

When we find the Green's function for an HRT, we have two boundaries. The

material above the upper boundary has infinite resistivity, and so is "corrected" with

image currents as in the section on thin conducting films (ie., an image current with the

same value as the current it is correcting for). The material below the lower boundary

has zero resistivity, and so is fixed in the manner just described in the previous section

(ie., the image current has opposite sign as the current it is correcting for).

The development of image currents is shown in figure 5.9.
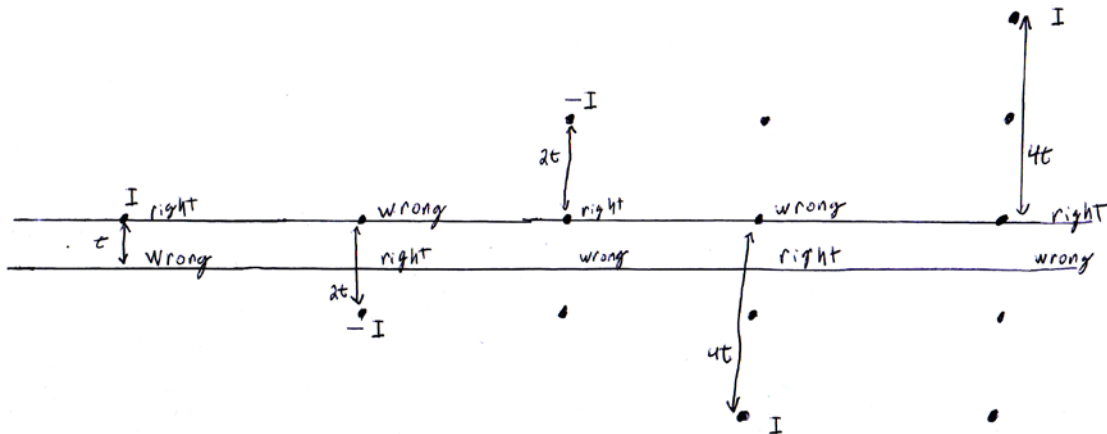
Figure 5.9. Development of image currents for an HRT. After the original
current, the signs of the images changes with every two images added.

We can write the potential for the 3D case:

$$V = \frac{I\rho}{2\pi} \left(\frac{1}{\sqrt{z^2 + r^2}} + \sum_{a=1}^{\infty} (-1)^a \left(\frac{1}{\sqrt{(2at - z)^2 + r^2}} + \frac{1}{\sqrt{(2at + z)^2 + r^2}} \right) \right)$$ [5.12]

Unlike the thin conducting film case, the terms here alternate sign. Since they also tend to zero as **a** tends to infinity, the potential sum automatically converges; we do not need to consider constants of integration. The potential is also automatically zero for all r at z=t.

Having the Green's function for the layer could be quite powerful. We could, in principle, find the potential created by any distribution of current sources. However, equation 5.12 is rather complicated, and we really would like a simplification.

Let's consider the *current* (not potential) for a *two* dimensional case, at z=0. Current would normally be more difficult to deal with than potential, since potential is a scalar while current density is a vector. However, thanks to the boundary conditions at z=0, the current there has only a component parallel to the interface. It might as well be a scalar there.

The infinite series for the current density is

$$J(r, z = 0) = \frac{I}{2\pi} \left(\frac{1}{r} - \frac{2r}{\left(r^2 + (2t)^2\right)} + \frac{2r}{\left(r^2 + (4t)^2\right)} - \frac{2r}{\left(r^2 + (6t)^2\right)} + \frac{2r}{\left(r^2 + (8t)^2\right)} - \ldots \right)$$ [5.13]

We take inspiration from Euler's method for summing powers of the reciprocal odd integers (the so-called Basel problem in the case that n=2). He found sums of the form $1/1^n + 1/(-3)^n + 1/(5)^n + 1/(-7)^n + 1/(9)^n + \ldots$ by considering the function

$$y = -\sqrt{2} \sin\left(\frac{\pi}{4} x - \frac{\pi}{4} \right)$$ [5.14]

124

That function equals 1 when x=0, and has simple roots at x=+1,-3,+5,-7,+9,….

Therefore, it may be expressed as an infinite product

$$y = (1-\frac{x}{1})(1+\frac{x}{3})(1-\frac{x}{5})(1+\frac{x}{7})(1-\frac{x}{9})...$$ [5.15]

It also can be expressed as a Taylor series.

$$y = 1 - \frac{\pi}{4}x - \frac{\pi^2}{32}x^2 + \frac{\pi^3}{384}x^3 + \frac{\pi^4}{6144}x^4 - \frac{\pi^5}{122880}x^5 - \frac{\pi^6}{2949120}x^6 + ...$$ [5.16]

By expanding the product and collecting terms of a given power of x, and matching to the

Taylor series, the sums are found.

$$\frac{1}{1} - \frac{1}{3} + \frac{1}{5} - \frac{1}{7} + ... = \frac{\pi}{4}$$

$$\frac{1}{1^2} + \frac{1}{3^2} + \frac{1}{5^2} + \frac{1}{7^2} + ... = \frac{\pi^2}{8}$$

$$\frac{1}{1^3} - \frac{1}{3^3} + \frac{1}{5^3} - \frac{1}{7^3} + ... = \frac{\pi^3}{32}$$ [5.17]

Anyway, the important point, or at least the one that is relevant for us, is that an analytic function that equals 1 when x=0 and with roots a, b, c, d… may be expressed as (1-x/a)(1-x/b)(1-x/c)(1-x/d)…. (To be completely rigorous, it is also possible that the function could include a factor of an exponential, which has no zeroes, of an analytic function, but that is rather nitpicky from a physics perspective)

Similarly, Euler also stated $\cos(\pi x/2) = (1-(x/1)^2)(1-(x/3)^2)(1-(x/5)^2)(1-(x/7)^2)…$ The point in this case being that if the roots are paired as +/-a, +/-b, +/-c, the function may be expressed as a product of difference of squares.

We also note

$$\frac{d}{dx} \log[1 + (\frac{x}{a})^2] = \frac{2x}{a^2 + x^2}$$ [5.18]

But the expression for current density is nothing but a sum of terms of that form!

By examining equation 5.13, we see we want a function with zeroes x=+/-2*t*i*n, and also x=+/-4*t*i*n, to take care of the alternating signs. The functions are

$$\sinh\left[\frac{\pi}{2t}x\right] = x\left(1 + \left(\frac{x}{2t}\right)^2\right)\left(1 + \left(\frac{x}{4t}\right)^2\right)\left(1 + \left(\frac{x}{6t}\right)^2\right)...$$

$$\sinh\left[\frac{\pi}{4t}x\right] = x\left(1 + \left(\frac{x}{4t}\right)^2\right)\left(1 + \left(\frac{x}{8t}\right)^2\right)\left(1 + \left(\frac{x}{12t}\right)^2\right)...$$ [5.19]

Therefore,

$$J(r, z = 0) = \frac{I}{2\pi}\left(-\frac{d}{dr}\log\left[\sinh\left(\frac{\pi}{2t}r\right)\right] + 2\frac{d}{dr}\log\left[\sinh\left(\frac{\pi}{4t}r\right)\right]\right)$$ [5.20]

Which evaluates to

$$J(r, z = 0) = \frac{I}{2t}\left(\frac{1}{e^{\frac{\pi r}{2t}} - 1} - \frac{1}{e^{\frac{\pi r}{t}} - 1}\right)$$ [5.21]

and also

$$J(r, z = 0) \approx \frac{I}{2t}e^{-\frac{\pi r}{2t}} \qquad \text{, if r>>t}$$ [5.22]

Of course, if the TCO resistivity is not exactly zero, the current density in the HRT will not exponentially decay indefinitely. In this two dimensional case, it will exponentially decay until it reaches a constant value determined by the boundary conditions.

$$J = \frac{I\rho_{TCO}}{2(\rho_{TCO}t_{HRT} + t_{TCO}\rho_{HRT})}, \quad \text{if} \quad r \gg \frac{2t_{TCO}}{\pi}\log\left[\frac{t_{HRT}\rho_{TCO} + t_{TCO}\rho_{HRT}}{t_{HRT}\rho_{TCO}}\right] \quad [5.22b]$$

5.7 A Transmission Line Approach (An Aside)

Our modeled two dimensional HRT has one dimension of finite and one dimension of infinite extent. Far from the point of current injection, therefore, a two dimensional HRT appears to be one dimensional. An alternative approach for modeling it would be as a ladder of resistors. See Figure 5.10. This mathematical problem is discussed in [39].
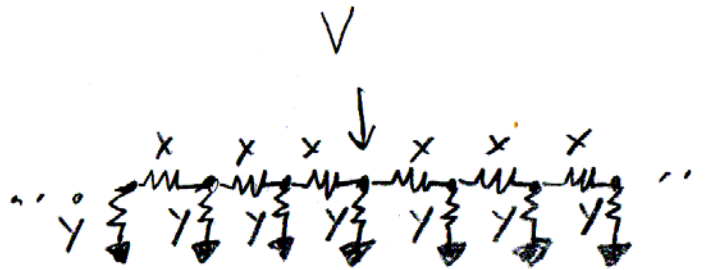
Figure 5.10. An "infinite ladder" of resistors. If voltage is applied at one node, and the effective resistance of the ladder is known, the current that flows through that node could be found.

We can focus on the right side of the ladder. See Figure 5.11.

$$R = x + y \qquad R = x + \cfrac{y}{1 + \cfrac{y}{x+y}} \qquad R = x + \cfrac{y}{1 + \cfrac{y}{x + \cfrac{y}{1 + \cfrac{y}{x+y}}}}$$
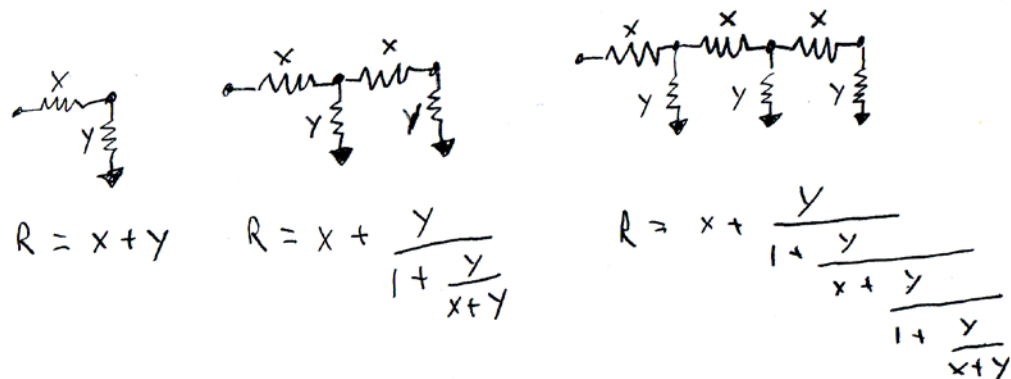
Figure 5.11. The effective resistance for the first few resistors may be found directly.

127

The resistance of the first few set of resistors can be found directly in a straight forward manner. After the series of the first few has been found, we see by induction that the effective resistance for the right side of the ladder can be expressed as a continued fraction.

$$R = x + \cfrac{y}{1 + \cfrac{y}{x + \cfrac{y}{1 + \cfrac{y}{x + \cfrac{y}{1 + \cfrac{y}{x + \cfrac{y}{1+...}}}}}}}$$ [5.23]

Because the continued fraction is periodic, it can be expressed as a solution of a quadratic equation. If the continued fraction (R minus the initial x term) is z, then we see

$$z = \cfrac{y}{1 + \cfrac{y}{x + z}}$$

This leads to a quadratic equation

$$(x + z)y = z(x + z) + yz \qquad \text{or} \qquad z^2 + (x)z - xy = 0$$

which has solution

$$z = \frac{-x + \sqrt{x^2 + 4xy}}{2}$$ [5.24]

The total resistance of the right side of the ladder is z+x. The total resistance of the entire ladder is made of the right and left sides (which have equal values) in parallel with y. Therefore, the total resistance is

$$\frac{1}{R_{Total}} = \frac{1}{y} + \frac{4}{x + \sqrt{x^2 + 4xy}} \quad \text{or} \quad R_{TOTAL} = \frac{xy}{\sqrt{x^2 + 4xy}} \qquad [5.25]$$

Assume the node where voltage is applied is n=0. Then the voltage there is of course V(0)=V and I(0)=V/R$_{TOTAL}$. Suppose n=1 is the node to the right of n=0. Then the current that flows into that node is I(0) - V/y+V//(z+x). Alternatively, it is V/(z+x). So,

$$I(1) = \frac{2V}{x + \sqrt{x^2 + 4xy}} \qquad [5.26a]$$

$$V(1) = V\left(1 - \frac{2x}{x + \sqrt{x^2 + 4xy}}\right) \qquad [5.26b]$$

From that point on (see Figure 5.12),
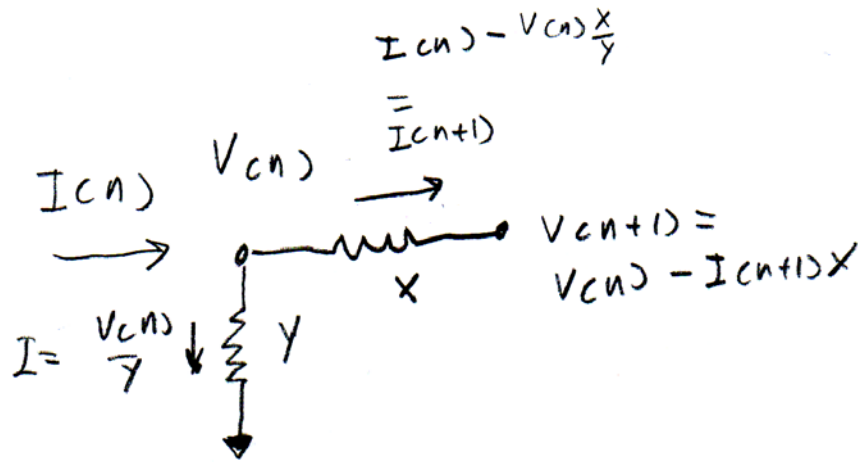
Figure 5.12. Derivation of Equations 5.27.

$$I(n+1) = I(n) - \frac{V(n)}{y} \qquad [5.27a]$$

$$V(n+1) = V(n) - I(n+1)x \qquad [5.27b]$$

129

Let us assume I(n+1)=αI(n) and V(n+1)=βV(n). Substituting that into Equations 5.27, we obtain

$$
\begin{bmatrix} I_n & 0 \\ xI_n & V_n \end{bmatrix} \begin{bmatrix} \alpha \\ \beta \end{bmatrix} = \begin{bmatrix} I_n - \dfrac{V_n}{y} \\ V_n \end{bmatrix}
$$

Or

$$
\begin{bmatrix} \alpha \\ \beta \end{bmatrix} = \begin{bmatrix} 1 - \dfrac{V_n}{I_n}\dfrac{1}{y} \\ 1 - \dfrac{I_n}{V_n}x + \dfrac{x}{y} \end{bmatrix}
$$ [5.28]

Now we can substitute in I(1) and V(1) from Equations 5.26. This gives

$$
\begin{bmatrix} \alpha \\ \beta \end{bmatrix} = \begin{bmatrix} \dfrac{x + 2y - \sqrt{x^2 + 4xy}}{2y} \\ 1 + \dfrac{x}{y} - \dfrac{2x}{\sqrt{x^2 + 4xy} - x} \end{bmatrix}
$$

With a bit of algebra, it is possible to show that those two expressions, for α and β, are equal. Because they are equal for n=1, they must be equal for *all* n. (Consider 5.28: α and β depend on the ratio of V and I. If V and I maintain the same ratio after the first increase in n, they will always maintain the same ratio).

This means

$$
I(n+1) = I(n)\left(1 - \dfrac{2x}{x + \sqrt{x^2 + 4xy}} \right), \text{ for all } n>1
$$ [5.29]

In other words, the one dimensional infinite ladder of resistors is shown to exhibit exponential current decay, just as the two dimensional HRT. We can even make this model continuous. We can substitute x=x/m, and y = y*m, and consider what happens at a node m points away (which we call an increment of 1 in the n coordinate). Then

130

$$I(n+1) = I(n)\left(1 - \frac{2x}{x + \sqrt{x^2 + 4m^2 xy}}\right)^m \qquad [5.30]$$

If we now take the limit as m tends to infinity (which can easily be done on a modern

graphing calculator, such as the HP50g or TI-89), then we find

$$I(n+1) = I(n)e^{-\sqrt{\frac{x}{y}}} \qquad [5.31]$$

It is also possible to convert Equations 5.27 to a continuous differential form

$$\frac{dI}{dn} = -\frac{V}{y}$$

$$\frac{dV}{dn} = -xI$$

Combining those gives

$$\frac{d^2 I}{dn^2} = \frac{x}{y}I$$

which is a standard form of the telegrapher's equation, and directly leads to 5.31.

This model does not show the 1/r dependence that appears in Equation 5.21 when

r is very small, as that is an inherently two dimensional phenomenon, whereas this model

is entirely one dimensional.

5.8 HRT Model

Although it was a fair amount of work to get to Equation 5.22, it can be used to

justify a simple HRT model. The exponential decay of current laterally in the layer

means that there is little lateral flow from the cell to the shunt. In other words, in Figure

5.1, we make the simplification of getting rid of resistor R_K (by setting its value equal to infinity).

Because current does not flow laterally, it flows predominantly transversely through the HRT. Suppose the area of the cell is A_C while the area of the shunt (say, if the shunt was caused by a pinhole) is A_H. Then, simply by using the equation for the resistance of a wire, we find

$$R_S = \frac{\rho t}{A_C} \tag{5.32a}$$

$$R_H = \frac{\rho t}{A_H} \tag{5.32b}$$

ρ is the resistivity of the HRT layer. The idea is that we can increase ρt to make R_H large, at the expense of also increasing R_S; however, since the area of the shunt is presumably much smaller than the area of the total cell, there may be a value of ρt for which R_S is small while R_H is large.

We again use a rectifying diode model. See Figure 5.10, which shows the model in both regimes of operation and the equations that describes those regimes.
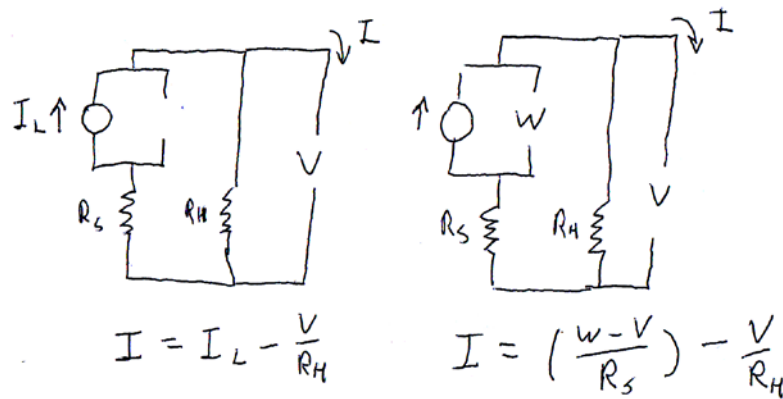
$$I = I_L - \frac{V}{R_H} \qquad\qquad I = \left(\frac{w - V}{R_s}\right) - \frac{V}{R_H}$$

Figure 5.13. HRT schematic model. Left, when the diode is "off"; right, when the diode is "on".

132

The equations describing the model are

$$I = I_L - \frac{V}{R_H}$$

[5.33a]

$$I = \left(\frac{W-V}{R_S}\right) - \frac{V}{R_H}$$

[5.33b]

For the cell to be any good, the maximum power point must be at the intersection of those two curves. This should be fairly obvious, especially if you think about the simple series resistance model from the previous chapter. The curves intersect at

$$V = W - I_L R_S$$

[5.34a]

$$I = \left(1 + \frac{R_S}{R_H}\right) I_L - \frac{W}{R_H}$$

[5.34b]

We multiply those equations together to find the maximum power point, substituting in the values of R_S and R_H from equations 5.32, and also substituting $x=\rho t$. After taking the derivative with respect to x and setting to zero (and making the substitution that $W=V_{OC}$), we find

$$(\rho t)_{OPTIMUM} = \frac{A_C A_H}{\sqrt{A_C A_H + A_H^2}} \frac{V_{OC}}{I_L}$$

[5.35a]

Since A_H is presumably much smaller than A_C, with $s=A_H/A_C$, we can use the approximation (and substitute $J_{SC}=I_L/A_C$)

$$(pt)_{OPTIMUM} \approx \sqrt{s} \frac{V_{OC}}{J_{SC}}$$

[5.35b]

Equation 5.35 gives the value for the optimal HRT parameters in terms of the product ρt. It might be interesting to see that the optimal value depends on the product,

133

and not the sheet resistance, or that, for example, the thickness alone has no optimum value.

Of course, the thickness does enter in through Equation 5.22. In making the assumption that there is no lateral current flow, we assumed that the thickness of the HRT layer is very small. (We also assumed $\rho_{HRT} >> \rho_{TCO}$ when deriving equation 5.11) If t is fairly small but not small in comparison to a shunt's linear dimensions, we would suppose Equation 5.22 implies that the shunt's effective radius is increased by order t. We would therefore generally desire to make t as small as possible while simultaneously allowing the product ρt to satisfy Equation 5.35.

There are practical limits to that, of course. HRT materials may only be available in a certain range of resistivities. Also, when depositing a thin layer, if the layer is so thin that its thickness is comparable to the mean variations in the thickness (due to, for example, shadowing of the deposition), then there might be gaps in the HRT where it offers no protection at all.

Another important point to make regarding Equation 5.35 is that I_L (or J_L) and V_{OC} are "ideal" values that would be obtained if there was no shunt.

To give an example of using Equation 5.35, suppose we had a cell of area $0.031cm^2$ (a typical laboratory cell size) and a pinhole of area $7.1 \times 10^{-6} cm^2$ (about 30 microns in diameter, a rather large pinhole, large enough to completely kill the cell if no HRT was present), $V_{OC}=0.8V$, and $J_{SC}=20mA/cm^2$. Then the ideal $\rho t=0.6ohm\text{-}cm^2$. It is easy to find an equation that exactly describes Figure 5.13, which is

$$I = I_L - I_O \left(e^{\frac{q\left(V\left(1+\frac{R_S}{R_H}\right)+IR_S\right)}{nkT}} - 1 \right) - \frac{V}{R_H} \qquad [5.36]$$

Figure 5.14 shows the theoretical JV curve of a cell with the shunt as described, but with an HRT as predicted from Equation 5.35, as well as an "ideal" JV curve with no shunt or HRT. It is seen that the HRT is predicted to almost completely salvage the cell. The ideal efficiency of 12.4% is reduced only to 12.0%.
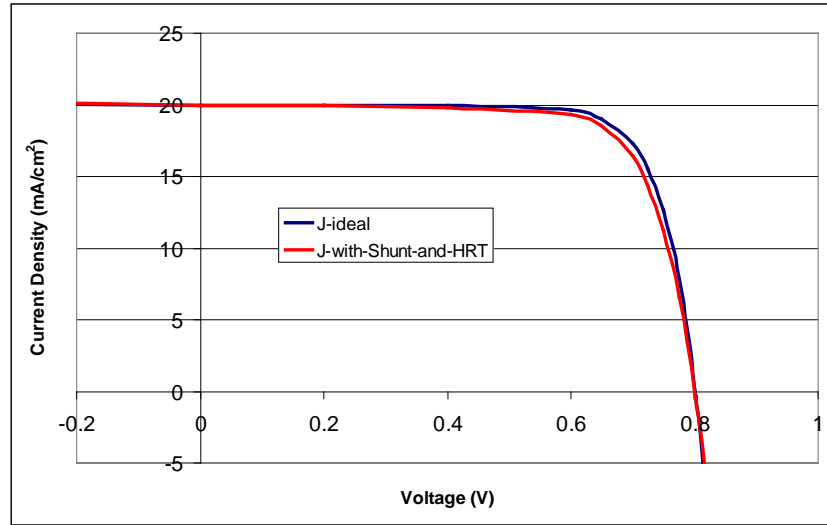
Figure 5.14. Theoretical comparison of an ideal cell's JV to a JV of a cell with a shunt but also an optimal HRT.

Of course, in reality, we might not be able to customize an HRT layer for each cell that is fabricated (especially since the CdTe is generally deposited after the HRT – pinholes would develop after the HRT was deposited). However, if a certain process tends to produce cells with shunts of a certain statistical nature, then perhaps an HRT layer could be designed based on the statistics. We can also imagine an iterative process.

Suppose that an original non-optimal HRT_1 is used which still results in shunt resistance R_H, but which also is at least good enough to prevent lateral current flow so that the shunt resistance provides an estimate of the shunt size. Then another HRT_2 could be tried with parameters

$$(\rho t)_2 \approx \sqrt{\frac{(\rho t)_1}{R_H}} \frac{V_{OC}}{J_{SC}} \qquad\qquad [5.37]$$

Shunt size could also be determined in finished cells using techniques such as thermography[40]. Also, we gave an example of finding an optimal HRT for a given shunt size, but, if the effective series resistance and efficiency was considered acceptable, it would work at least as well for shunts of smaller size as well. It also may offer some protection against even larger shunts, even if it is not ideal.

This might lead us to wonder if we can estimate just how large a shunt may be dealt with by using an HRT layer. In the absence of a shunt, the model of Figure 5.13 and Equation 5.36 simply becomes a cell with a series resistance. The series resistance from the HRT is (from Equation 5.35)

$$R_{SERIES} = \frac{1}{\sqrt{1+\frac{1}{s}}} \frac{V_{OC}}{J_{SC}} \approx \sqrt{s}\frac{V_{OC}}{J_{SC}}$$

where s is the ratio of the shunt area to the active cell area. (Also, as a note,

$$R_{SHUNT} = \frac{1}{\sqrt{s+s^2}} \frac{V_{OC}}{J_{SC}} \approx \frac{1}{\sqrt{s}}\frac{V_{OC}}{J_{SC}})$$ Let's suppose we would consider a fill factor of 60%

in the absence of a shunt to be acceptable. If we use Figure 4.13 to determine what the acceptable series resistance from the HRT would be for that fill factor, we find it to be about 8ohm-cm^2=8x10^{8}ohm-μm^2. This gives s=0.04, ie., an area of 4 percent of the total

cell area (or, more exactly, s/(1+s)=3.8%). Of course, for an HRT thickness of 0.1μm,

we would need to find a material of resistivity 8×10^9ohm-μm.

Figure 5.15 shows the predicted results of using such an HRT. We again used the

parameters such that the "ideal" cell has V_{OC}=800mV and Jsc=20mA/cm^2. With no HRT

and no shunt, the efficiency is 12.4%. With the HRT but no shunt, the efficiency is

reduced to 9.7%. With the HRT and the shunt the HRT is optimized for, the efficiency is

still 8.2%. Finally, we consider a shunt with value s=0.16 (in other words,

s/(1+s)=13.8% of the total cell area; at this point, the correct is more significant. We also

correct the current density by considering that a significant portion of the total cell is not

generating current). Though the HRT is not ideal for this shunt, the performance is still

4.1%! It is sort of amazing that the performance is so high for such a large shunt.
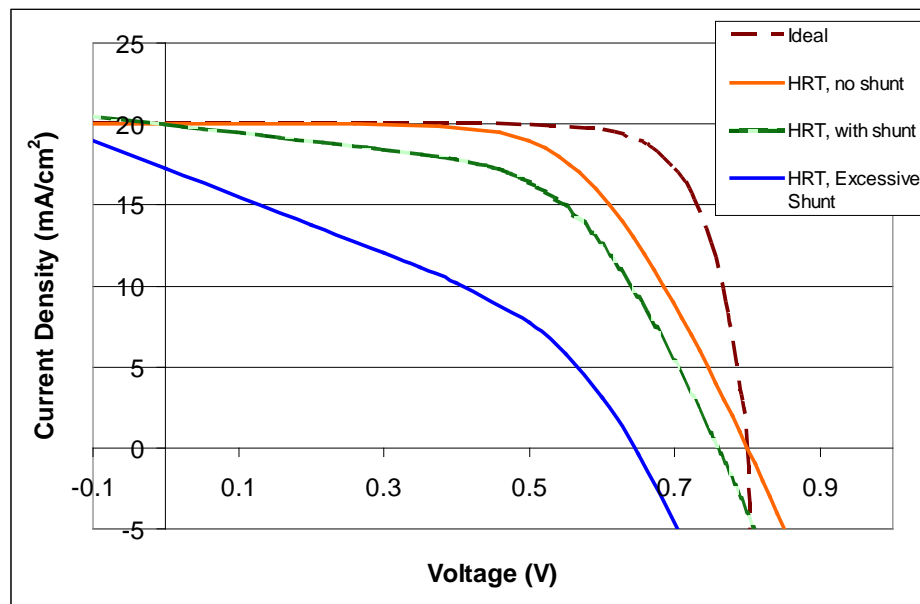
Figure 5.15. Pushing the possibilities of an HRT. The "ideal" curve
shows the JV for a cell with the same diode parameters as the other
curves, but no HRT and no shunt. The "HRT, no shunt" curve is for a
cell with no shunt but an HRT optimized for a pinhole that is ~4% the
size of the cell, and the "HRT, with shunt" curve is for a cell with the
HRT and the shunt. The "Excessive Shunt" curve uses the same
HRT (optimized for a pinhole that is 4% the size of the cell) but in
that case the pinhole is 13.8% of the cell.

Realistically, for especially large shunts or nonuniform cells, techniques that specifically target shunts rather than the entire cell may be needed[41].

We had wished to have experimental confirmation of the model presented in this chapter. However, the experiment had more difficulties than the series resistance experiment and no results are yet available.

5.9 The Distributed Cell Model Reconsidered

We can also consider the effect of an HRT on a distributed cell, similar to what we considered in Section 4.10. A model of a distributed cell with an HRT is shown in Figure 5.13. We are now having a more general model, where the two diodes have *different* voltage drops U and W when "on", and all the resistors are different.
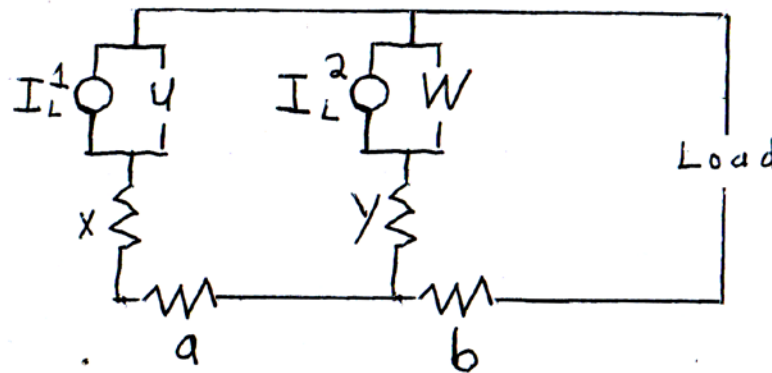
Figure 5.16. Model of a distributed cell with HRT.

There are now four regimes of operation:

1) Both diodes are "off". In this case, the current through the load is $I = I_L = I_L^1 + I_L^2$, independent of the voltage on the load. This is the flat part of the current-voltage curve, as before.

2) The inner diode is "on" and the outer diode is "off".

$$I = \frac{U - V + I_L^2(x+a)}{x+a+b}$$ [5.38a]

3) The outer diode is "on" and the inner diode is "off".

$$I = \frac{W - V + yI_L^1}{y+b}$$ [5.38b]

4) Both diodes are on.

$$I = \frac{Uy + W(x+a) - V(x+y+a)}{x(y+b) + (a+b)y + ab}$$ [5.38c]

As this situation is more complicated than before, and subject to many more parameters, we will only consider one point on the JV curve, that of open-circuit. There are three possible values of open-circuit voltage, depending on which regime applies.

$$V_{OC}^1 = U + I_L^2(x+a)$$ [5.39a]

$$V_{OC}^2 = W + I_L^1(y)$$ [5.39b]

$$V_{OC}^3 = \frac{Uy + W(x+a)}{(x+y+a)}$$ [5.39c]

Note that if W=0, Equation 5.39b is essentially the very poor cell model Equation 3.6 (in other words, diode W has become so bad it *is* a shunt).

The open-circuit voltage that will result will be whichever expression from Equations 5.39 gives the *lowest* result.

We note that the voltages in Equations 5.39a and 5.39b, however, can be made arbitrarily large (so long as the relevant I_L is not zero) by increasing the value of x and y (which could be achieved in reality by using an HRT of arbitrarily large ρt). Therefore, there must be some HRT for which equation 5.39c *must* apply.

In the case that x=y=0 (no HRT), Equation 5.39c gives the result from Section 4.10, that the open circuit voltage is the voltage drop across the outer diode (W here), regardless of the inner diode (however, if U is less than W, then Equation 5.39a might give the true V_{OC}). Now suppose that x and y are determined by the formula for the resistance of a wire as before.

$$x = \frac{(\rho t)_{HRT}}{A_U}$$

$$y = \frac{(\rho t)_{HRT}}{A_V}$$

A_U and A_V are the areas of the cell with voltage drops U and V, respectively. Now suppose $(\rho t)_{HRT}$ tends to infinity (realistically, since we don't want the HRT to introduce high series resistance, this could still apply so long as x and y are large in comparison to a). Then we have the result

$$V_{OC} = \frac{A_U U + A_V V}{A_U + A_V} \qquad [5.40]$$

In words: An HRT can cause the open circuit voltage to be the weighted (by area) average of the voltage drops of the component elements of the cell, regardless of their distribution.

Chapter 6 – Zinc Oxide

6.1 Introduction

We have used zinc oxide doped with aluminum (ZnO:Al, or AZO) in our solar cells. As our solar cells are, to our knowledge, the current best CdTe cells on polymers that use AZO as a top contact, it is important to understand this layer. We will in this chapter discuss basic properties of conductive AZO, fabricating high resistance zinc oxide that may be used as a high-resistive transparent (HRT) buffer layer, and the stability of AZO during $CdCl_2$ treatment.

6.2 Basic Parameters

Basic parameters of AZO may be determined by growing a film, then finding the transmission of the film (as in a double beam spectrometer) and the sheet resistance. These two characteristics are the most important when using AZO as a solar cell contact.

The films in this section were grown in the chamber shown in Figure 2.11. A ZnO target doped 2% by weight with Al_2O_3 was used. Base pressure was on the order of $1x10^{-7}$ Torr, substrate-gun distance was about 6cm, RF power was 50W with negligible reflected power, and argon pressure was 10 mTorr.

Figure 6.1 shows resistivity of a few AZO films grown at different temperatures. This data is intended to be representative but not a comprehensive study of resistivity versus temperature.
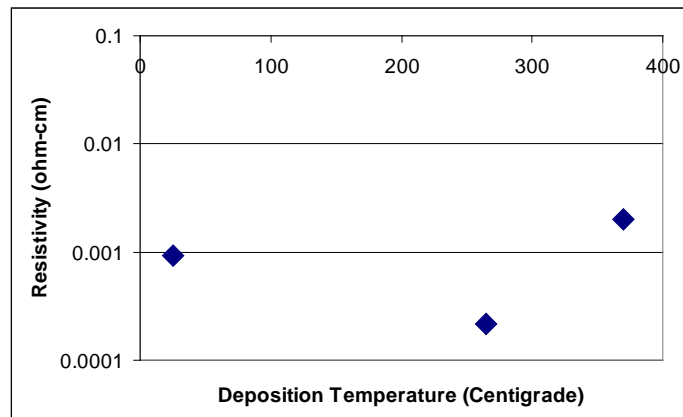
Figure 6.1. Resistivity of AZO as a function of deposition temperature.

The dependence of resistivity on temperature is weak, but it is quite possible to grow films of good (low) resistivity, between 10^{-4} and 10^{-3} ohm-cm. There appears to be a minimum in resistivity around 260°C, which is where we usually grow our ZnO films.

Figure 6.2 shows a transmission curve of a representative AZO film.
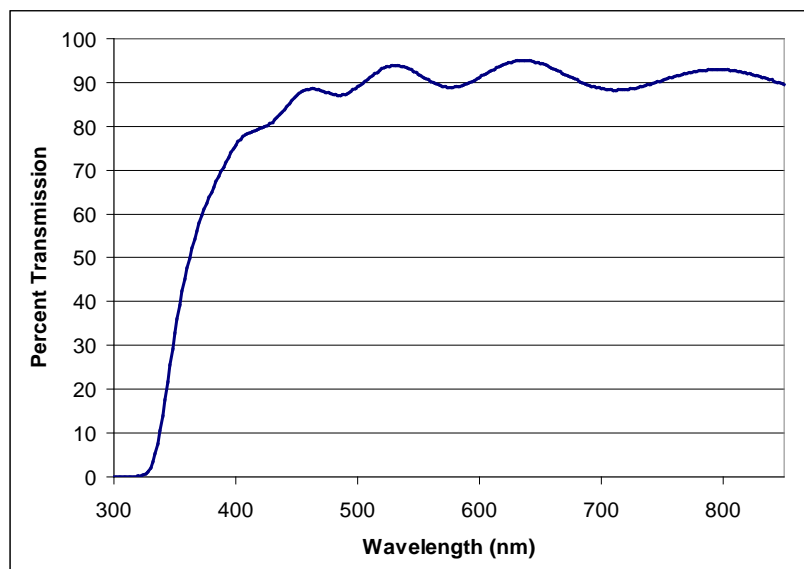
Figure 6.2. Transmission of a representative AZO film. This particular film is about 720 nm thick and has a sheet resistance of about 6 ohms/square.

The transmission is near or above 90% for a wide range, from over 850 nm down to about 450 nm. This makes AZO a good TCO for CdTe cells, which absorb from about 850nm (slightly redshifted from CdTe's bandgap, due to alloying with CdS and bandbowing) down to at least 515 nm (where CdS begins absorbing), though, by thinning the CdS, decent quantum efficiency has been observed down to at least 400nm in excellent cells.

Transmission data such as in Figure 6.2 allows calculation of film thickness, index of refraction, and absorption coefficient. It is commonly remembered by solar cell workers that a thin film is anti-reflecting at a given wavelength if the film's thickness is one-quarter the wavelength of light in the material. This is true for any odd multiple of one-quarter the wavelength. So, if consecutive peaks in transmission are λ_1 and λ_2, then they are anti-reflecting of order m and m+1, and

$$t = \frac{(2m+1)\lambda_1}{4n} \hspace{5cm} [6.1a]$$

$$t = \frac{(2m+3)\lambda_2}{4n} \hspace{5cm} [6.1b]$$

or

$$t = \frac{\lambda_1 \lambda_2}{2n(\lambda_1 - \lambda_2)} \hspace{5cm} [6.2]$$

The index of refraction can be estimated from the difference in maxima and minima in the transmission data, on the basis of the result from the Fresnel equations that the fraction of light reflected at an interface is

$$R = \left[\frac{n_1 - n_2}{n_1 + n_2} \right]^2 \hspace{5cm} [6.3]$$

143

Multiple reflections will occur within the film. We have written a simple program in QuickBasic, based on a paper by Manifacier et al.[42], that does the repetitive calculations necessary to extract the thickness, index of refraction, and the absorption coefficient. The source code for the program is listed in the appendix. The theory behind the paper assumes that the film is weakly absorbing (which is satisfied by ZnO). A practical consideration is that the film must be of uniform thickness. This is not necessarily the case with sputtered ZnO films; in our systems, we have observed center-to-edge thickness variations of up to 30%. Measuring the center of the film and using small apertures in the spectrometer can lead to better results. An indication that the film is not uniform enough and that the program's calculations are unreliable is if different sets of extremes in the transmission curve imply drastically different thicknesses. In cases where the various extrema have implied a consistent thickness, the calculated thickness agrees with profilometer measurements. There are difficulties with using profilometer measurements exclusively. We usually measure CdTe films with a profilometer by using a razor to mechanically scratch a region in the film for the profilometer to trace. However, our ZnO films are not scribed with a razor. Masking part of the deposition with Kapton tape has been successful for measuring thickness; however, the adhesive outgases at 200°C, and can lead to film contamination, making other measurements (such as of optical or electrical properties) suspect. ZnO is also only weakly absorbing at the wavelength (355nm) our laser used for scribing operates. To ensure complete scribing requires at least a reasonable estimate of what we expect the thickness to be.

In any case, transmission data consistently predicts that the index of refraction of our ZnO films is about 1.7. This is less than the single crystal value of 2.0, probably due to sputtered films being less dense.

The bandgap of our AZO films is calculated in figure 6.3. ZnO is a direct bandgap material, so it obeys[43]

$$\alpha h\upsilon = A\sqrt{h\nu - E_g}$$ [6.4]

Where α is the absorption coefficient, $h\upsilon$ is the photon energy, and E_g is the material bandgap. Therefore, plotting $(\alpha h\upsilon)^2$ versus photon energy should give a straight line that intersects the x-axis at the bandgap. Such a graph is shown in Figure 6.3.
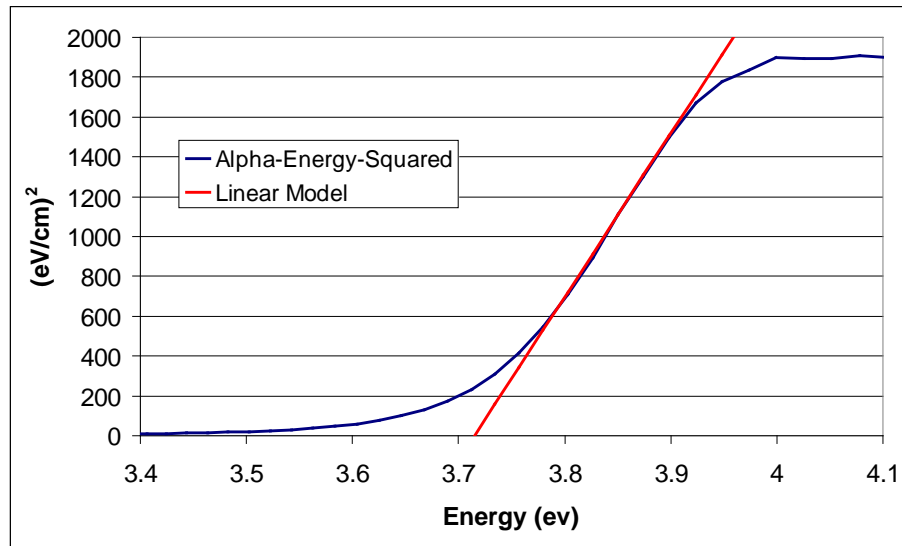
Figure 6.3. Determination of the bandgap of an AZO film.

At energies higher than 3.9eV, the absorption seems to roll off. This is an experimental artifact due to signal-to-noise limitations of the spectrometer. At energies below the bandgap, photons may still be absorbed if isolated (eg., defect) states exist in the bandgap.

The measured bandgap is about 3.71eV. This is higher than the single crystal

ZnO bandgap of 3.3eV. The blue shift is due to the Burstein–Moss effect[44]. In an

insulating semiconductor, the onset of absorption is the difference in energy from the

bottom of the conduction band to the top of the valence band. However, for a material

that is doped to the point of being a conductor, as is the case for AZO, the bottom of the

conduction band is filled, and by the Pauli principle, no further electrons may be added to

those states. The apparent bandgap, therefore, is between the top of the valence band and

the top of the filled states in the conduction band[45]. This is illustrated in Figure 6.4.

Figure 6.4. The Burnstein-Moss Effect. In semiconductors that are doped to the point of having high electron concentration in the conduction band, the apparent optical bandgap is not from the bottom of the conduction band to the top of the valence band, but from the top of the valence band to the top of the filled states in the conduction band.

6.3 Oxygen Doping and HRT Fabrication

High resistance zinc oxide has been used as an HRT buffer layer in CdTe and

CIGS cells[46]. Other buffer layers have been used, such as zinc stannate (Zn_2SnO_4) in

the world record CdTe cell.

ZnO is natively doped n-type by a relative deficiency of oxygen (or, equivalently,

a relative excess of zinc). Two mechanisms for this have been proposed[47]. An ionized

zinc atom could fit in an interstitial lattice position, and could donate two conduction electrons per ion from its outer shell. Alternatively, each oxygen atom has two "holes" in its outer shell. An oxygen vacancy could subtract those two holes, essentially adding two electrons.

In either case, adding excess oxygen, such as by flowing oxygen as well as argon during the sputter deposition, could decrease the relative deficiency of oxygen and the doping mechanics and hence cause the resulting film to be more intrinsic and of higher resistivity[48,49]. As we saw in the previous chapter, being able to control resistivity could be a great boon for HRT design.

Experimentally, ZnO films were grown on glass at 260°C. Two tanks of process gas were used, a 100% argon tank, and a 0.47% tank of oxygen with the balance argon. (The reason such a funny number like 0.47% was used is that 0.5% was the target when filling the tank, and 0.47% was the actual analysis result afterwards). Mass flow controllers were used to adjust the relative amount of each gas, and thus the partial pressure of oxygen, within the chamber. The sputter target used was a ZnO target doped 2% by weight with Al_2O_3 – the same target that could be used for depositing conductive AZO films. Being able to deposit both TCO and HRT from one target is in some cases a convenience.

The results are shown in Figure 6.5. As seen, resistivity varies over 5 orders of magnitude within the range of oxygen used.
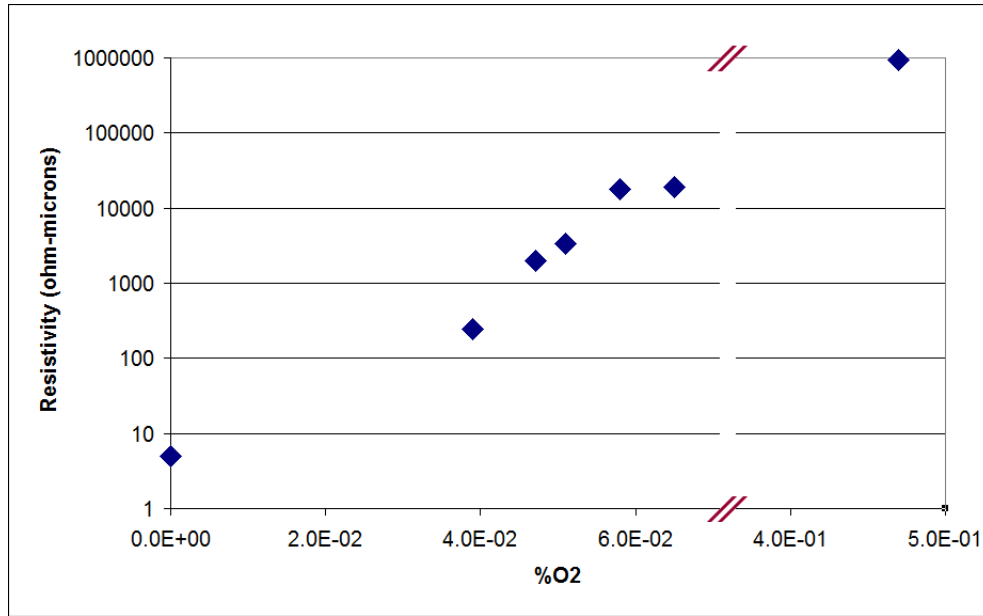
Figure 6.5. The resistivity of ZnO films grown from a ZnO:Al target, as a function of oxygen in the sputter gas.

We remember that in the previous chapter we found that a good HRT for a particular application would have $\rho t=0.6$ohm-cm$^2=6$x10^7ohm-μm^2. Even for the most resistive material in Figure 6.5, a film 60 microns thick would be needed to reach that ρt value. That is a ridiculous thickness (both in terms of the time needed to deposit it, and also in terms of what a small thickness is, as relates to the discussion in section 5.7). We therefore desired to be able to grow ZnO films of even greater resistivity.

6.4 HRT Made from an Undoped ZnO Target

To achieve higher resistivity, we also grew films from an undoped target in a different chamber, with different gas tanks. These films were grown at room temperature.

148

The films grown in pure argon, with no oxygen added, had a resistivity of 9.3×10^5 ohm-µm. This value compares to the result from films grown from a doped target with about 0.5% oxygen in the sputter gas.

We also grew films using the undoped target and 1% oxygen in the sputter gas. This film was too resistive to measure with our standard four point probe system. We instead used a strip line measurement procedure.

A mask with quarter inch strips of gold, separated by 20, 30, 40, etc. thousandths of an inch apart, was used to deposit gold on our HRT film. The resistance between those strips was measured with two probes. See Figure 6.6. The region between the strips is a rectangle, or, in other words, a fraction of a square. The resistance between the strips divided by the fraction of a square should be the sheet resistance of the film in ohms per square.
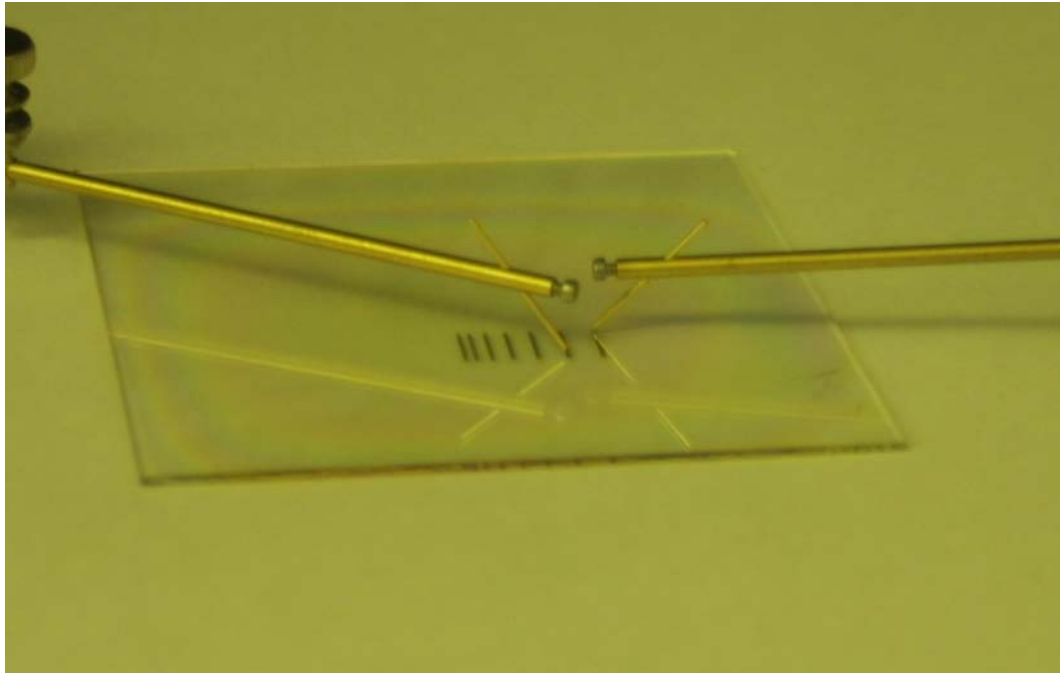
Figure 6.6. The stripline resistance measurement. Parallel strips of gold of linearly increasing spacing are deposited on our HRT film. Probes are contacted to the strips to measure the resistance between them.

The reason a four point probe measurement is usually used rather than a two point probe is that various other resistances might be in series with the film resistance, particularly contact resistance between the probes and the film. This of course is an issue with this measurement procedure. However, such resistances are presumably constant. By using multiple strips, a linear function of resistance versus "squares" should be obtained. The y-intercept of this line will contain any resistances (such as contact resistance) that are in series with the film. The slope will be the true sheet resistance.

Based on what we have said so far, what is an advantage of using a strip line measurement? The resulting current based on the voltage applied is

$$I = \frac{V}{R_{SHEET}\#} \hspace{4cm} [6.5]$$

where # is the number of squares. R_{SHEET} is very large for a resistive sample, so the current might be small and difficult to measure. If # is small, it will increase the current. For our set up, if we assume we need two data points for determination of the sheet resistance (so a linear fit may be used), the largest value of # would be (40"/1000)/0.25"=0.16 squares.

Also important for this measurement is a high quality multimeter. We have used a Keithley 617 programmable electrometer. This machine allows voltage to be set as high as 100V, and can read currents as low as $2x10^{-12}$ A. This means it can be used to measure resistances as high as $5x10^{13}$ohms. Based on the previous paragraph, this means this procedure can be used to measure sheet resistances as high as $5/0.16=3.12x10^{14}\Omega$/square.

One other refinement is used in measurement (from [50]). After applying the voltage, current is measured as a function of time. Due to the large resistance of the film, an RC time constant could be large. Another issue is that, with a highly resistive sample, there might be background currents which could be large in comparison with the current stimulated by the applied voltage. The situation is as in Figure 6.7.
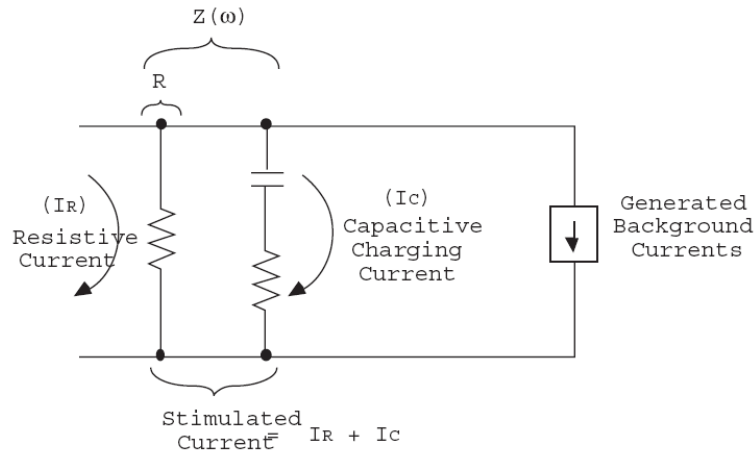
Figure 6.7. When applying a voltage to measure a highly resisting sample, three currents (the desired resistive current, a capacitive charging current, and background currents) may result.[51]

If the background current was equal in magnitude but of opposite sign as the stimulated current, the total current would be zero, implying infinite resistance, regardless of whatever the true resistance would be.

To deal with that, the applied voltage is alternated from +100V to -100V. The resistive current will change sign with applied voltage the background current will not (though it might drift with time). If I_1 is obtained with +100V and I_2 with -100V, then $(I_1-I_2)/2$ will cancel the background current and represent the absolute value of resistive current obtained with an absolute potential of 100V. Further current measurements may be taken to average out noise. If the voltage alternates with each I, and the currents are I_1, I_2, I_3, I_4, etc., then the average currents will be

$$I = \frac{(I_1 - I_2)}{2}$$

$$I = \frac{(I_1 - 2 \cdot I_2 + I_3)}{4}$$

$$I = \frac{(I_1 - 3 \cdot I_2 + 3 \cdot I_3 + I_4)}{8}$$

$$I = \frac{\sum_{j=1}^{n} \binom{n-1}{j-1} \cdot (-1)^{(j-1)} \cdot I_j}{2^{n-1}} \qquad [6.7]$$

An example of the data from such a measurement is given in Figure 6.8. The blue diamonds are the values of current measured as a function of time. It should be fairly obvious where the voltage polarity changes occur. The *charge* on the capacitive element would normally change continuously, even when voltage is changed discontinuously. However, the *current* on a capacitive element will change discontinuously with a discontinuous change in voltage, explaining the discontinuous changes in current with polarity charge. The final data points before the polarity change are the End Values (pink rectangles) and are the values I_1, I_2, etc. By waiting enough time before recording the end values, the capacitive charging current I_C will presumably have decayed to zero (which can of course be confirmed by measuring for longer periods of time). Also shown is a simple average of the currents as well as the binomial average from Equation 6.7.
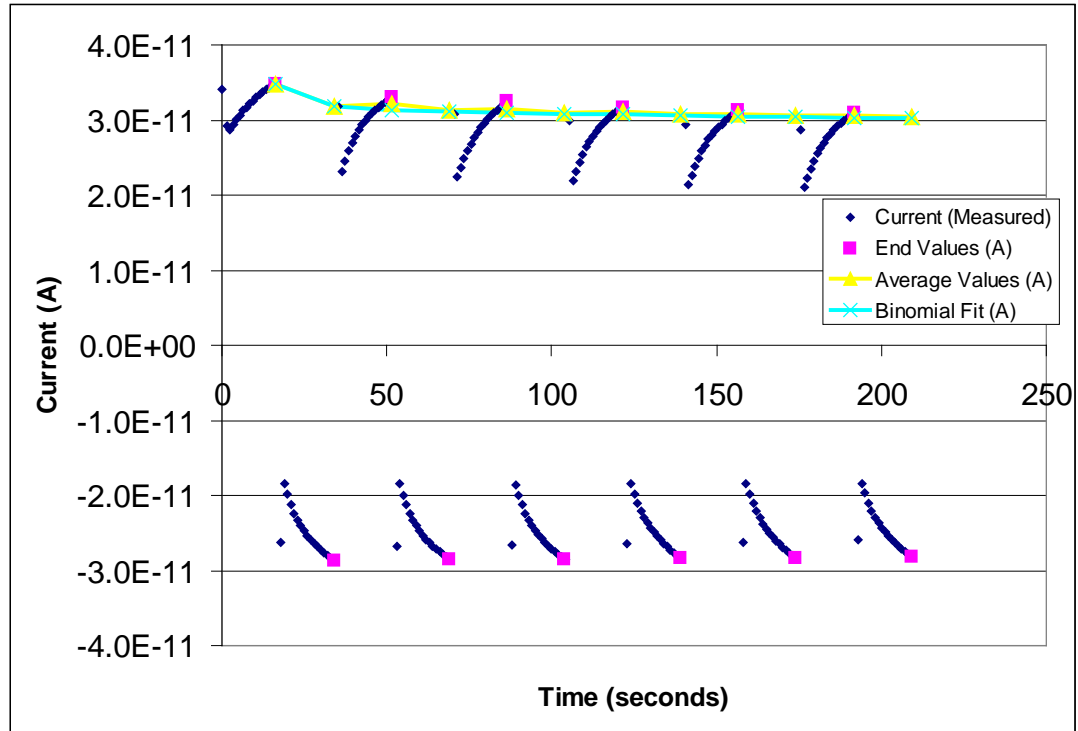
Figure 6.8. Current between a pair of strips in an example of a strip line resistance measurement.

Figure 6.9 shows the average values and binomial averages zoomed in. For our particular sample and experiment, background currents were not comparable to the stimulated current. Also, as seen in Figure 6.9, the simple averages and binomial averages converge to the same value, so Equation 6.7 was not strictly necessary. However, even in these data, the binomial average shows less noise than the simple average.
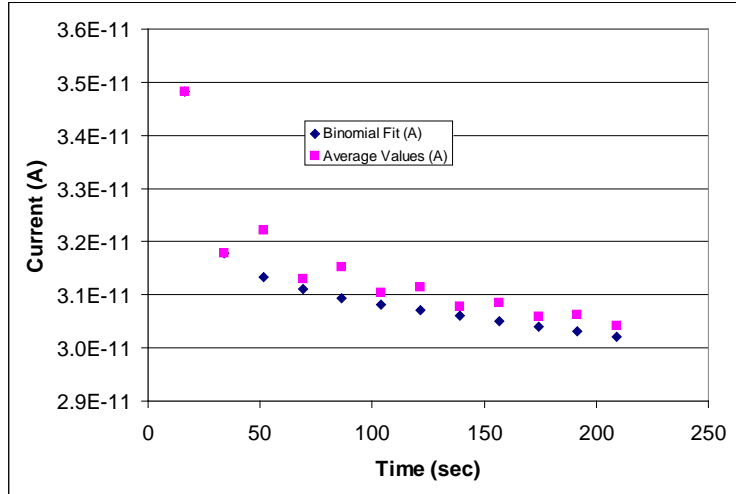
Figure 6.9. The currents in Figure 6.8 converge to a value of about 3.06×10^{-11} regardless of whether a binominal weighted average or a simple average is used.

Figure 6.10 shows the result of resistance versus "squares" for a sample that is 1.7 microns thick. The data are indeed linear. The slope is 6.3×10^{12} ohms/square. Consequently, the resistivity is 1.07×10^{13} ohm-microns. This is 7 orders of magnitude more resistive than any of the films shown in Figure 6.5.
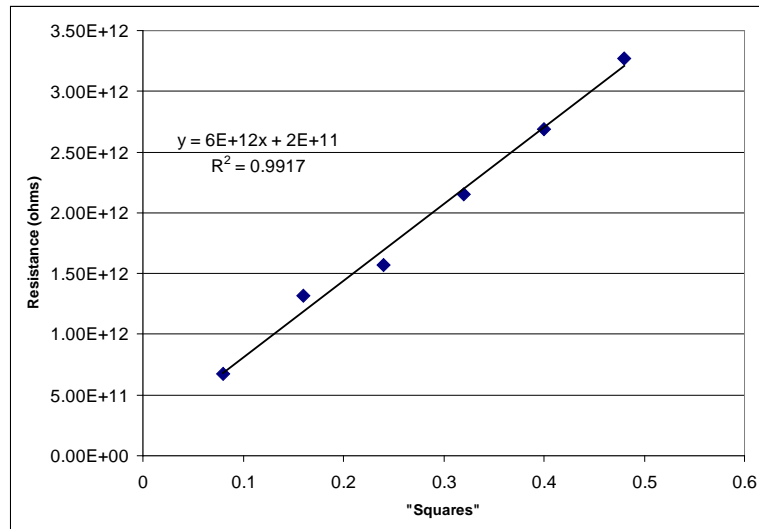
Figure 6.10. The sheet resistance of our sample. Each measurement of the type from Figure 6.8 contributes one data point to this graph. The data are linear. The conclusion is that the film has a sheet resistance of 6.3×10^{12} ohms/square.

We also grew films with 6% oxygen in the sputter gas. The resulting films were too resistive to measure, even with the previous procedure. However, based on our estimates in the previous chapter, we do not really need more resistive films. It would be more useful to fill in the gap between 0% and 1% O_2 in the sputter gas for undoped ZnO targets.

The results are summarized in Table 6.1.

Table 6.1. Resistivity as a function of oxygen in sputter gas when using an undoped ZnO target.

Percent O_2 in sputter gas	Resistivity (ohm-μm)	Resistivity (ohm-cm)
0	9.3×10^5	93
1	1.0×10^{13}	1.0×10^9
6	$>10^{15}$	$>10^{11}$

6.5 AZO Change With Chloride Treatment

Being able to deposit AZO films of good conductivity is of course important, but it is most important that the film is of good conductivity in the finished cell. However, we have observed changes in the sheet resistance of AZO films after $CdCl_2$ treatment.

There had been some knowledge of the instability of AZO. For example, work by Pern et al.[52] showed AZO degraded in the presence of damp heat (which is typically defined to be 80°C and 80% relative humidity) with drastic morphological changes.

We have taken SEM images of as-grown as well as $CdCl_2$ treated AZO films. Representative images are shown in Figure 6.11. No obvious morphological changes were observed.
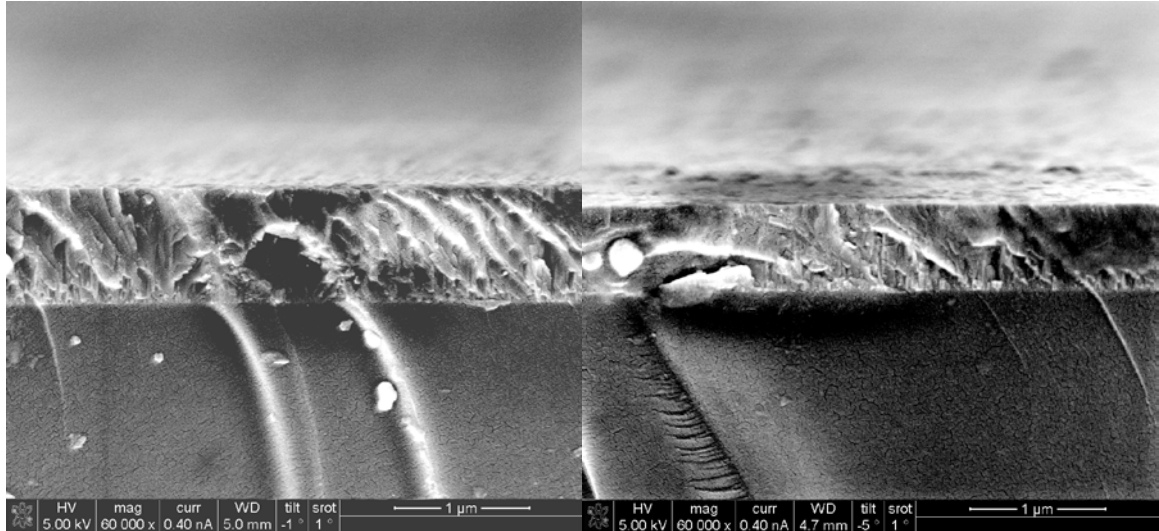
Figure 6.11. SEM images of AZO films (shown above the glass substrate) before (left) and after (right) $CdCl_2$ treatment. No obvious morphological changes are seen.

The lack of morphological changes could suggest a different degradation mechanism than damp heat. The damp heat studies were different, however, in that they involved hundreds of hours of stress and more than two orders of magnitude changes in sheet resistance.

In any case, we desired to study the sheet resistance change systematically. This was done by growing AZO films of different thicknesses and subjecting them each to a 15 minute wet $CdCl_2$ treatment at 387°C. (This anticipates a result later in the thesis; this was found to be an optimum chloride treatment). The data of as-grown sheet resistance versus sheet resistance after treatment is shown in Figure 6.12, along with the curve y=x (the curve that would be followed if no change occurred) for reference, and a model.

Bear in mind that thicker films have less sheet resistance; on the x-axis, film thickness decreases to the right.
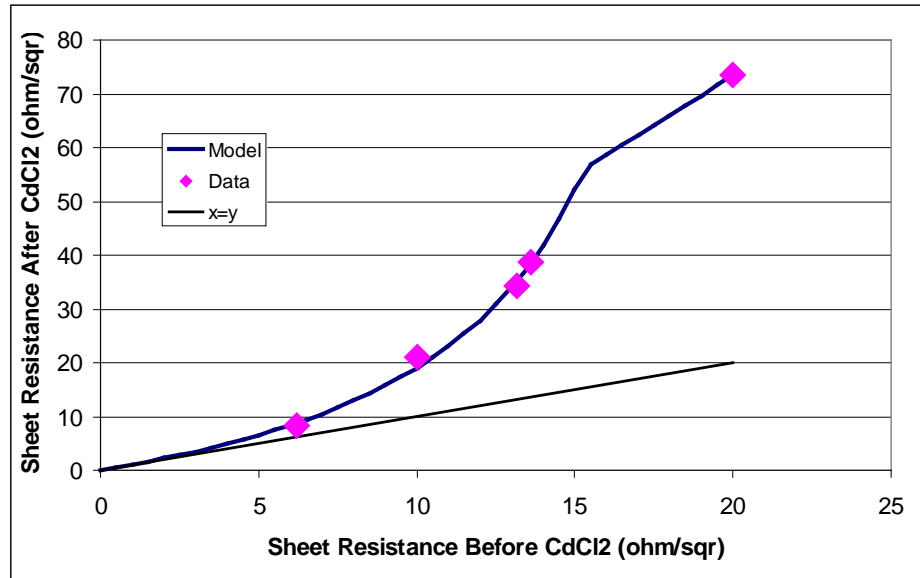
Figure 6.12. The sheet resistance change of AZO films with $CdCl_2$ treatment.

Consider, for example, the far right data point. 20 ohms/sqr. is not so bad, and is sort of close to Tec15 which is often used to make good solar cells. However, as we saw in chapter 4, with 80 ohms/sqr., the fill factor will sharply decrease with increasing cell size. On the other hand, by using a thicker film, a 6 ohm/sqr. film may become a 9 ohm/sqr. film, which is still quite good.

We modeled the change by assuming a fixed (due to the same time being used for all films) thickness L was changed after $CdCl_2$ treatment to a resistivity of ρ_C from an original value of ρ_O. The original film thickness is T. See Figure 6.13.
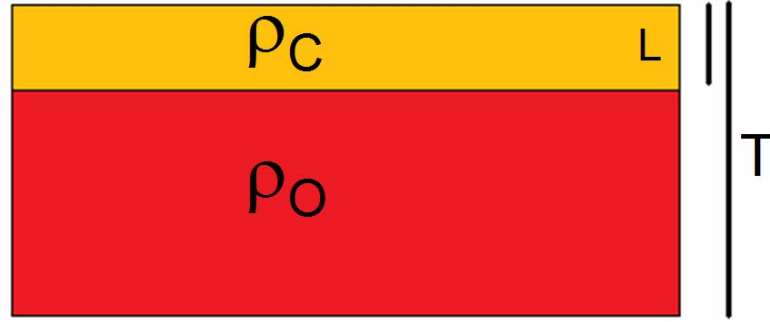
Figure 6.13. A model of the AZO change as shown in figure 6.12. The original film thickness is T. After CdCl2 treatment, a fixed thickness L changes resistivity.

What happens when we make a four-point-probe measurement? The outer probes inject current, and near those probes, the current will spread out (if the probes truly contacted the film at a point, then the current density would initially be proportional to $1/r^2$ in region 1, as in previous chapters, and then would have complicated reflections at the boundaries, as suggested in the previous chapter on the section on bilayers). However, far from the probes, in comparison to the thickness of the film, the current again will spread cylindrically.

However, unlike before, the current density cylinder in the top region will have a different value than the current density in the bottom region.

Because the probes measuring voltage only contact the top of region c, we can first consider region c alone. The current that passes through region c will be some value I_C. Since the layer has thickness L and resitivity ρ_C, the voltage measured is

$$V = \frac{I_c \rho_c}{\pi L} \log(2) \tag{6.8}$$

This is just a modification of equation 4.12. When we find the sheet resistance, we divide that voltage by the total current I, not just I_C. The current densities in the two regions are different, but they obey the boundary condition of equation 5.3.

$$\rho_c J_c = \rho_o J_o \qquad [6.9]$$

To get J from I, we divide by the thickness of the layer (and also $2\pi r$, which is the same in both cases), so

$$\frac{\rho_c I_c}{L} = \frac{\rho_o I_o}{T - L} \qquad [6.10]$$

And of course

$$I_C + I_O = I \qquad [6.11]$$

Those two equations can be solved for I in terms of I_C.

$$I = \left[\frac{\rho_C (T - L) + \rho_o L}{\rho_o L} \right] I_C \qquad [6.12]$$

So, the voltage between the inner probes divided by the current flowing through the outer probes times the correction factor $\pi/\log(2)$ gives the sheet resistance.

$$R_{SHEET}^{AFTER} = \frac{\rho_o \rho_c}{L\rho_o + (T - L)\rho_c} \qquad [6.13]$$

If T<L, we would simply use

$$R_{SHEET}^{AFTER} = \frac{\rho_c}{T} \qquad [6.14]$$

Let's think about whether equation 6.13 is reasonable. If $\rho_O = \rho_C$, then we would have a simple single layer and the equation indeed predicts $R_{SHEET} = \rho_O / T$. If either ρ_O or ρ_C tends to infinity, then the equation predicts that we would measure the sheet resistance of the other layer. This makes sense if the conductive layer is on top and is measured by

the probes, but might be more confusing if the insulating layer is on top. However, remember that the four point probe measurement works by injecting a current into a film and measuring the voltage produced as a consequence. If the upper layer was infinitely insulating, no current should be injected and the voltage consequently produced would also be zero, so the sheet resistance would be 0/0, which *could* be the sheet resistance of the other layer. In reality, there would probably be a stray voltage V, so the measurement would be V/0, implying infinity, but of course the stray voltage isn't *caused* by the injected current. Anyway, the equation is compatible with intuition.

We apply equations 6.13 and 6.14 to the data. ρ_O and T are measured from the original films. ρ_C and L are found from least squares fitting. With ρ_O=5 ohm-μm, we find ρ_C=20 ohm-μm and L=0.3μm. As shown in figure 6.11, there is good agreement between the model and the data.

The data were taken long before any model was proposed to explain it. The kink in the curve indicates that the original material is completely converted to the higher resistive material around 15 ohms/sqr.; only one data point so happened to be past that point on the curve. The data points to the left of the kink can be fit to the model fairly well even if ρ_C was set to infinity (with L adjusted only slightly to 0.24μm). However, even an order of magnitude value for ρ_C explains the important point. If ρ_C truly was infinite, or at least very large, we might wonder if this effect could be beneficial, if the converted layer of AZO could act as a sort of "automatic" HRT layer. ρ_C is large enough to significantly change the sheet resistance of our films, but is not close to the resistivity desired by an HRT layer (which would be at least greater than 1000 ohm-μm). This is

160

consistent with our experience, which is that intentional HRT layers must be added to see

any benefits like they are supposed to provide.

We also conducted an experiment of testing one thick film of AZO repeatedly to

determine the sheet resistance as a function of time. We hypothesized that the thickness

L of the converted layer could be the result of, very generally, something diffusing into

the film. We would have expected L then to have a square root dependence on time, as

predicted by Fick's Law with an infinite source. Very generic models (the axes are not

given units because they are not important) of the result of such behavior is shown in

Figure 6.14.   R1 shows the case that ρ_C would be infinite, while R2 shows the case that

ρ_C is four times the initial value. The important detail is that for either curve, the second

derivative eventually becomes positive as the curve bends upwards.
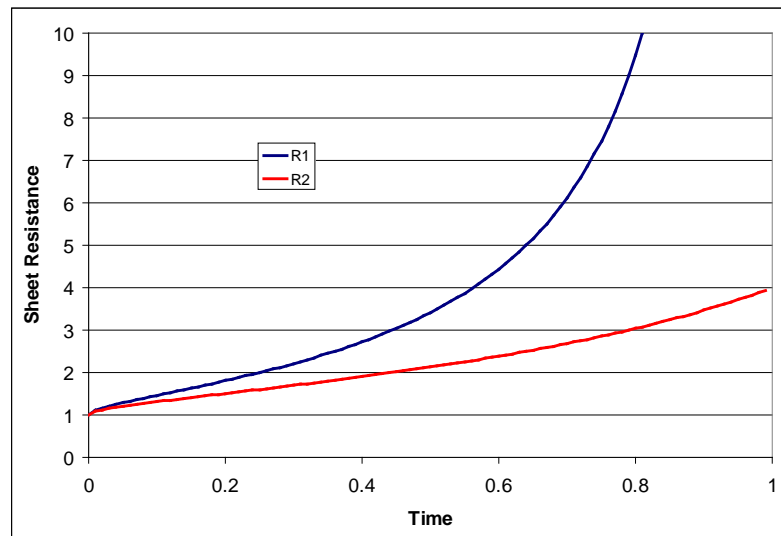
Figure 6.14. Generic traits of sheet resistance versus
treatment time if L in the model shown in Figure 6.12 were
assumed to have a square root dependence on time. One
curve assumes the converted layer has four times the
resistivity of the original layer; the other curve assumes the
converted layer has infinite resistivity.

161

Our actual data of sheet resistance as a function of CdCl2 treatment time is shown in Figure 6.15. As seen, the data do not bend upwards but tends to saturate. A practical conclusion from these data is that since there is not an especially strong treatment time dependence (there is certainly not as wide a range as exhibited by R1 in Figure 6.14!), we would expect different treatment times to have similar behavior as the basic result from Figure 6.12.
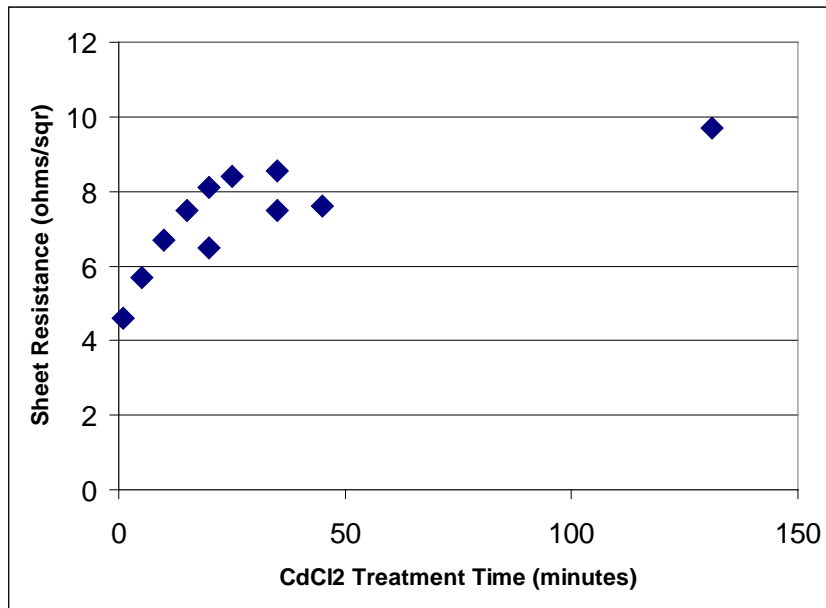
Figure 6.15. Sheet resistance of a single AZO film after repeated CdCl$_2$ treatments.

6.6 Conclusions

We have grown good quality AZO films with resistivities on the order of 10^{-4}ohm-cm and high transparency. We have also grown ZnO films whose resistivities vary over 17 orders of magnitude, some of which may be suitable for use as HRT buffer layers in solar cells. We have also identified a sheet resistance change in AZO with

CdCl$_2$ treatment. Systematically studying this change has allowed deposition of films

whose sheet resistance will remain of good value even in finished cells.

Chapter 7 – Development of All-Sputtered AZO/CdS/CdTe Solar Cells on Polyimide

7.1 Introduction

In this chapter, we will present a series of case study cells we have fabricated on polymers that were landmarks in our understanding and development of higher efficiency cells.

7.2 Initial Results

The naïve approach to growing flexible solar cells would be to simply copy a method that has given good results for cells on glass. Of course, one immediate difficulty with even that approach is that our laboratory usually grows CdTe cells on Pilkington Tec glass (usually Tec7 or Tec15). Such glass is intended for energy efficient windows, so it is supplied to us with a low emissivity coating of fluorine doped tin oxide, which reflects infrared light. This is to help keep a house warmer in the winter and cooler in the summer. As a bonus for us, it also works as a TCO for solar cells. However, polyimide is not supplied with a TCO coating; we have to grow our own.

Nevertheless, we can proceed. The cell structure is shown in Figure 7.1.
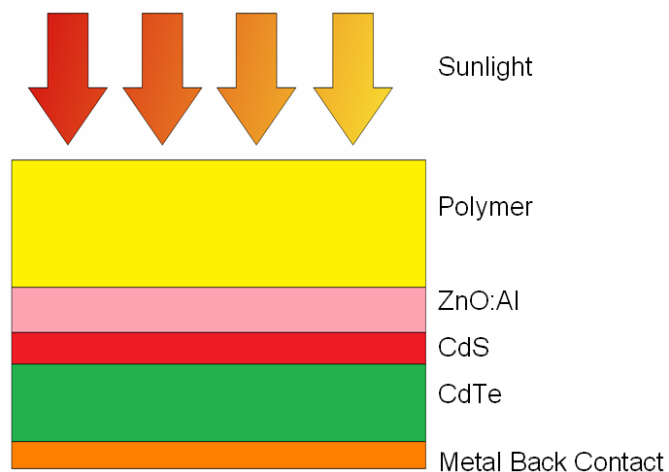
Figure 7.1. A flexible cell structure.

A polymer is used as a substrate. The cell is grown in the "superstrate" configuration so that the substrate faces up towards the sun and light enters the cell through it. The semiconductor layers are sputtered at 260°C. AZO would be deposited to have a sheet resistance of about 15Ω/□ (about 0.3μm). CdS is deposited 130nm thick; CdTe is deposited 2.4mm thick. All sputtered layers were deposited in systems with base pressure of 1×10^{-6} Torr or less and substrate to target distances of 6 cm. 50W RF power was used for AZO, 35W RF power for CdS, and 20W RF power for CdTe. AZO was grown at 10mTorr; CdS and CdTe were grown at 18mTorr. A vapor $CdCl_2$ treatment is performed at 387°C for 30 minutes. 3nm of copper followed by 20nm of gold are evaporated. The cell is then heat treated at 150°C for 45 minutes to diffuse the copper and improve the back contact.

This process is nearly identical to that used for our cells on glass. The main difference is that, of course, the substrate used for glass cells is Tec glass and AZO need not be deposited.

We may be disappointed to find that this process do not translate so easily to cells on polymer. Figure 7.2 shows Jsc, Voc, and fill factor data for 49 cells grown on 12.5μm Upilex (a brand of polyimide made by Ube). The JV curve for the best cell is shown in Figure 7.3. The cell efficiencies vary from 0 to 1.4%. The fill factor is nearly uniformly 25%. Even the best cell is fairly representative.
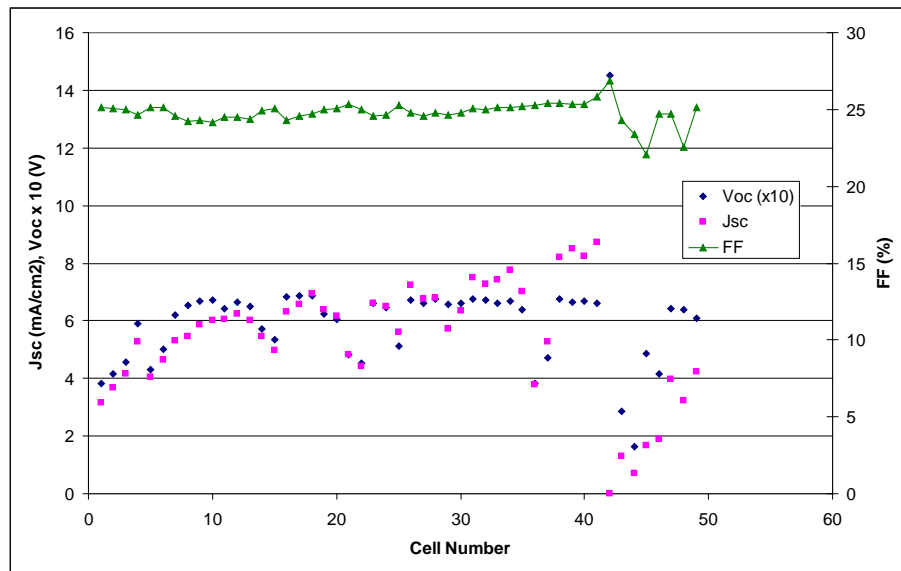
Figure 7.2. Summary of 49 cells made on 12.5μm Upilex.
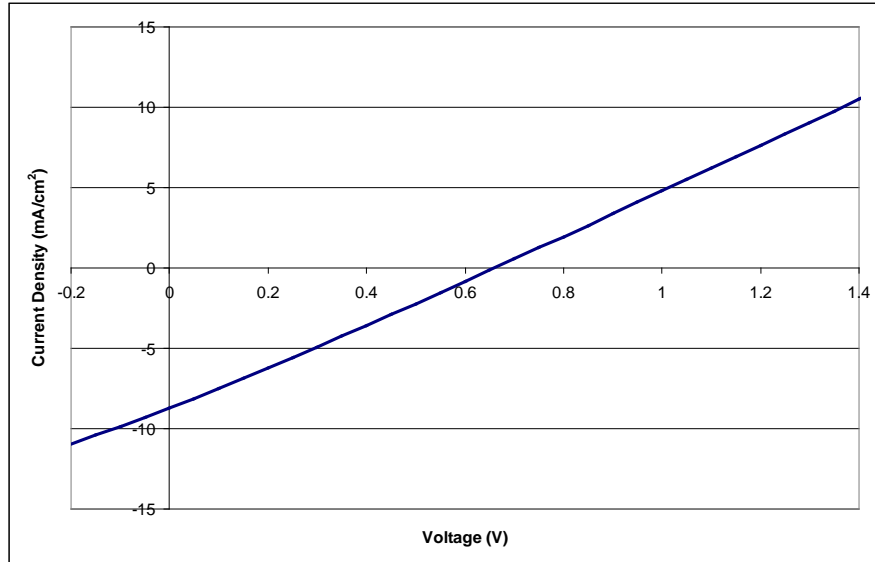
Figure 7.3. JV curve of the best cell of those summarized in Figure 7.2. Efficiency=1.4%

Rather than simply despair at the poor performance of these cells, we may use the very poor cell model from 3.6 to attempt to analyze them. We can use the best cell as an example. For the best cell, Voc=0.66V and Jsc=8.7mA/cm^2 and Eff=1.4%. Since the substrate is a polyimide, not glass, we will low ball our estimate of J_L as 15mA/cm^2. Through equations 3.4 and 3.8, we find R_{SHUNT}=44 Ω-cm^2 and R_{SERIES}=31 Ω-cm^2.

If there was no shunt resistance problem (but the same series resistance), we estimate the cell performace would be 4.5%. If there was no series resistance problem (but the same shunt resistance), we estimate the cell performace would be 2.5%. The shunt resistance is a greater problem, but the cell has both series and shunt resistance issues. This could have been an early indication, apart from the study in Section 6.5, that there was a problem with AZO stability in further steps of cell fabrication.

The cell size is 0.071cm^2, so the effective resistance is R_{EFF}=440 Ω. Equation 4.13 does not quite apply for these cells, because when they were made we did not use a

167

ring of indium around the periphery of the plate as a contact, but rather a single spot of indium. For the situation where the negative contact and cell have about the same linear dimension, we can estimate the effective resistance as about twice predicted by equation 4.13. This lets us estimate the sheet resistance of the final TCO as about 300Ω/square. This is larger than expected from Figure 6.11, but the study in 6.11 used 15 minutes of CdCl$_2$ treatment time while this cell was made with 30 minutes of CdCl$_2$ treatment time. An additional possibility, which would not be seen in a study on glass, is that cracks developed in the AZO film due to flexing.

Let us assume that the shunt was caused by pinholes and that we can use the wire equation to estimate the total pinhole size. The resistance of the pinhole would then be

$$\frac{\rho_{TCO} t}{A} = \frac{R_{SHEET}^{TCO} t^2}{A}$$, with t the thickness of the TCO and A the pinhole area. The shunt

resistance could be more than that (for a pinhole of given size) if the TCO resistance further screened the pinhole, but we will neglect that now (including it would increase the estimated size). Assuming the 300Ω/square value from above and a TCO thickness of 0.3μm, we find A$_{SHUNT}$=4.3x10-$^2\mu$m^2=4.3x10^{-10}cm^2. That would be a characteristic diameter of 0.1μm. This would correspond to s=6x10^{-9} in equation 5.35. When s is so small, equation 5.35 simplifies to $\rho t = s \dfrac{V_{OC}}{J_{SC}}$. This results in ρt=32$\Omega\mu$m^2. For a thickness of 0.1μm, this implies ρ=320$\Omega\mu$m. This is an achievable value for an HRT in figure 6.4 (and would be achieved with about 0.04% oxygen in the sputter gas).

7.3 Cells on Home-Cast Polymer

Although in the previous section we made estimates of possible loss mechanisms in initial polymer cells, there are other possible concerns for flexible cells. We have already mentioned shunting and flexing as concerns. Another issue could be that (very generally) something could diffuse from the polymer into the cell (especially during high temperature fabrication processes) and contaminate the semiconductor layers. We wished to completely eliminate the possibility of the former two issues while investigating the latter issue. To do this, we have made cells on home-cast polymer films. Dr. Dean Giolando supplied the polymer films. The polymer films were cast on glass and remained on glass throughout the entire fabrication and measurement process. This prevented flexing of the cells. In our original trial we also used a slightly thick CdS layer, of 0.15μm. Of course, the AZO and other layers will still be deposited onto the polymer, so any possible contamination issues would remain.

The polymer films were fabricated by applying approximately 0.25mL of polyamic acid (poly[pyromellitic dianhydride-*co*-4,4'-oxydianiline] amic acid) solution to a microscope slide. A second microscope slide was placed over the solution; the weight of the second slide distributed the solution evenly over both slides. After the slides were separated, a solvent was used to allow the solution to distribute uniformly. The polymer was cured in 0.5 Torr vacuum for 85°C for three hours, then 110°C for eight hours.

The transmission of the polymer is shown in Figure 7.4. The transmission is extremely high initially, but unfortunately decreases significantly after $CdCl_2$ treatment.
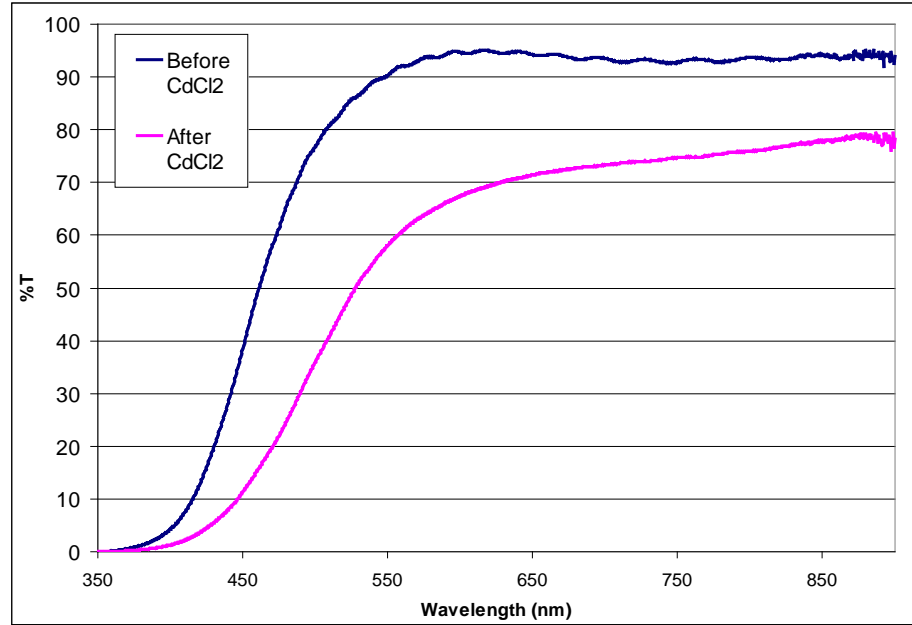
Figure 7.4. Transmission of home-cast polymer, before and after CdCl$_2$ treatment.

Nevertheless, even after CdCl$_2$ treatment the film remains partially transparent. The theoretical maximum short circuit current, based on the transmission curve of Figure 7.4, would be 17.3 for no CdS and 16.1 for thick CdS. This is enough to make a reasonable CdTe cell.

JV from the first cell is shown in Figure 7.5. The particular cell shown has Voc=584 mV, Jsc=13.40 mA/cm^2, FF=45.8%, Eff.=3.6%. The fill factor is now large enough to extract the sheet and shunt resistances directly, without need to refer to the very poor cell model. The sheet resistance is 14.7Ωcm^2. Although we had not yet carried out the experiment in Section 6.5, we had already speculated that the high sheet resistance was due to the zinc oxide being poorly conducting and not a more complicated effect (eg., some sort of non-ohmic contact). Evidence at the time for that was that

efficiency markedly improved when more indium for collecting current was applied to

the AZO (originally, the efficiency was 1.3%)
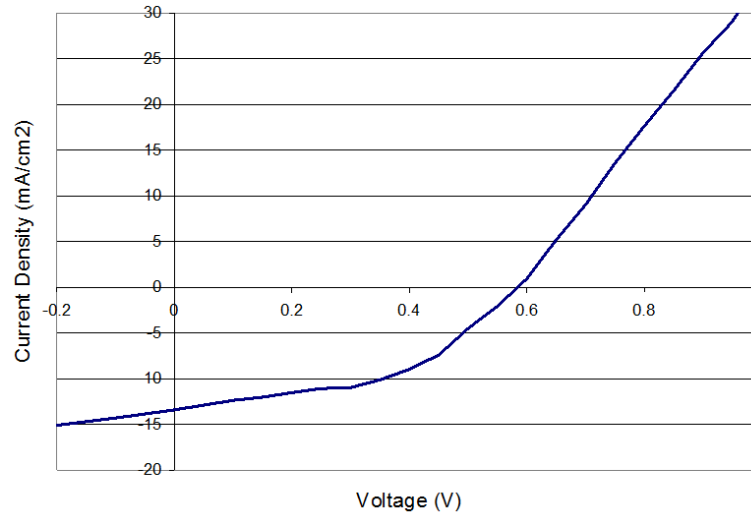
Figure 7.5. The first CdTe cell made on "home cast"
polymer. Efficiency=3.6%.

For the next sample on home made polymer, we increased the thickness of the

AZO layer to about 0.7 µm and used an unusually thick CdS layer of about 0.5µm.

Regions of thin CdS have been identified by others (such as Feldman et al.[53]) as causes

of nonuniformities and shunts. Due to absorption of the substrate, there was little current

to gain by using less CdS anyway. Although we were also using thick CdS, we also had

an HRT layer of about 70nm of intrinsic ZnO made by flowing about 0.047% oxygen in

the sputter gas. The CdTe was also slightly thicker than usual, about 3µm. The best JV

from this sample is shown in Figure 7.6.

This device represented considerable improvement. The best cell was 6.5%, with

Voc=720mV, Jsc=13.7mA/cm^2, and FF=64.9%. The yield was also good as the average

cell efficiency, averaged over 48 cells on the device, was 5.5%. The lowest parameter, as

compared to a good cell on glass, is short circuit current, but it is not so low when

considering the transmission of the polymer and the maximum theoretical J_{SC} with thick

CdS.
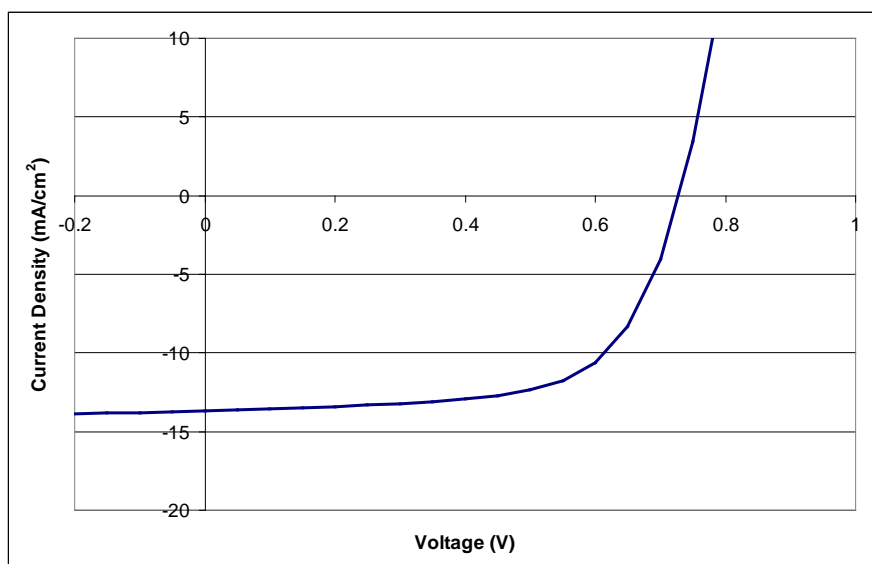
Figure 7.6. JV from home-made polymer cell with thicker layers.
Efficiency=6.5%.
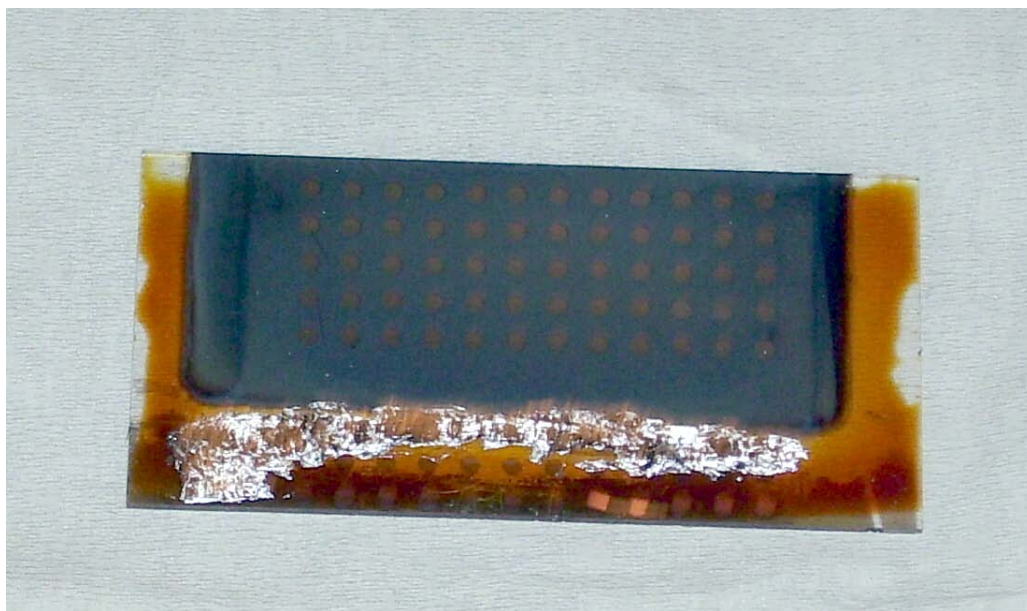
Figure 7.7. Photograph of the cell made on home-cast polymer adhered to
glass.

Although this device was technically "made on polymer", it was not truly "flexible", since the polymer was always strongly adhered to glass. Figure 7.7 shows a photograph of the device. We were not able to remove similar polymer films from glass without significant damage to the films.

Still, this cell demonstrated that simply *being on polymer* is not an insurmountable obstacle for reasonable performing cells. This cell, as compared to the previously cited cell on homemade polymer, also suggests that a buffer layer is capable of reducing shunting (though in this case CdS rather than ZnO is doing the work) and that thicker AZO may be needed for good fill factor than would be surmised by initial sheet resistance alone.

We used this same recipe for a device on free standing 50μm Kapton (a polyimide made by Dupont). The polymer was held in place for deposition by taping it (with high temperature Kapton tape) to glass or holding the polymer to glass with paperclips; we also assumed the polymer was in thermal equilibrium with the glass for the purposes of applying our systems' temperature calibrations.

Unlike the home-made polymer, the Kapton underwent virtually no degradation with a high temperature treatment. See Figure 7.8.
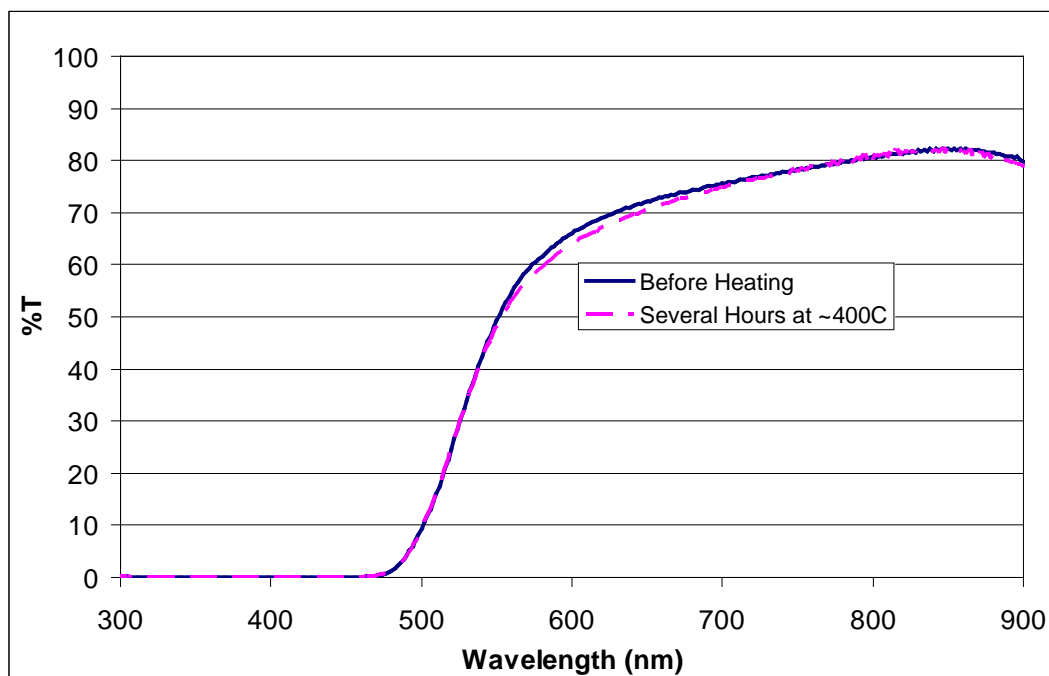
Figure 7.8. Transmission of 50μm Kapton, before and after high temperature treatment. Transmission virtually does not change.

The recipe essentially transferred to the free standing polymer. Good results (considering polymer transmission) and yield were obtained. Figure 7.9 shows a JV curve from a cell made with this recipe on 50μm Kapton. Efficiency was 6.4%.
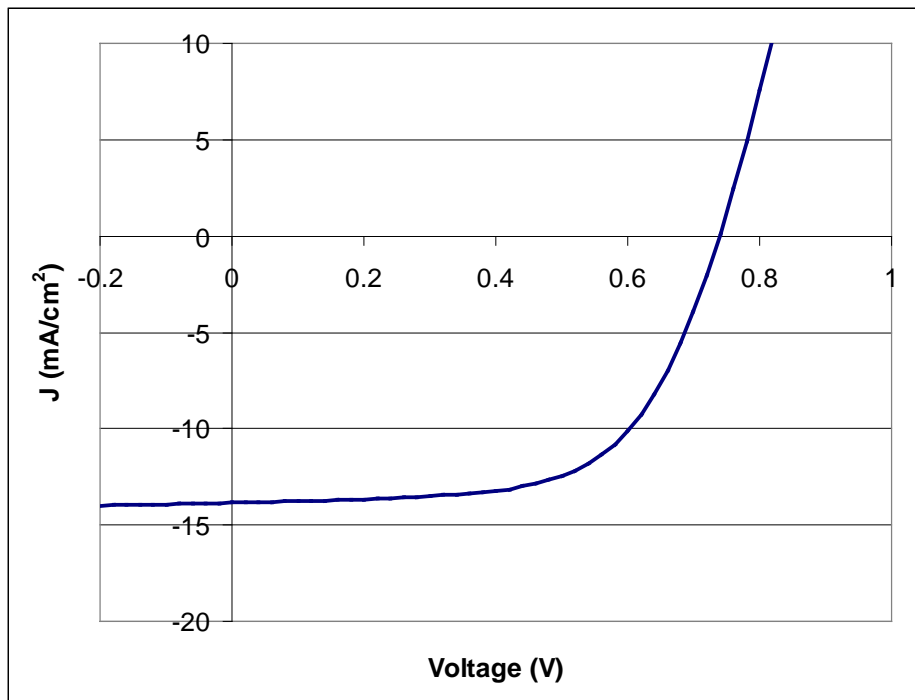
Figure 7.9. JV of cell on 50μm Kapton, using the recipe developed on home-made polymer. Voc=740mV, Jsc=13.8mA/cm^2, FF=62.4%, Eff=6.4%

7.4 Wet CdCl$_2$ Treatment

Although we have discussed issues that relate to cells on polymer in particular, one general issue our laboratory had experienced was inconsistent results for our standard baseline cells on glass. While our standard "recipe" was capable of giving cells up to 13% on Tec glass, other times cells of perhaps only 8% would be produced. This would confuse the results of experiments involving any cells more complicated than our standard recipe.

We attributed the inconsistent results to our vapor CdCl$_2$ treatment protocol.

The protocol: A piece of aluminosilicate glass (ASG) would be textured, either with sandpaper or beadblasting. This was to improve adhesion of a $CdCl_2$ film. The glass was heated on a hot plate in a fume hood. Drops of methanol saturated with $CdCl_2$ were applied to the glass. The methanol would quickly evaporate, leaving a small ring of $CdCl_2$ on the glass. This was repeated until the glass was fairly uniformly coated (using about 2.5mL of solution).

The glass was placed in a graphite crucible. The sample to be treated was placed film side down, facing the $CdCl_2$ and a few millimeters above it. Another graphite block was placed on top of the sample. Some small gap was allowed for dry air, which was periodically flowed through the system by computer controlled valves, to enter the space between the $CdCl_2$ and the sample. An illustration of this is shown in figure 7.10.
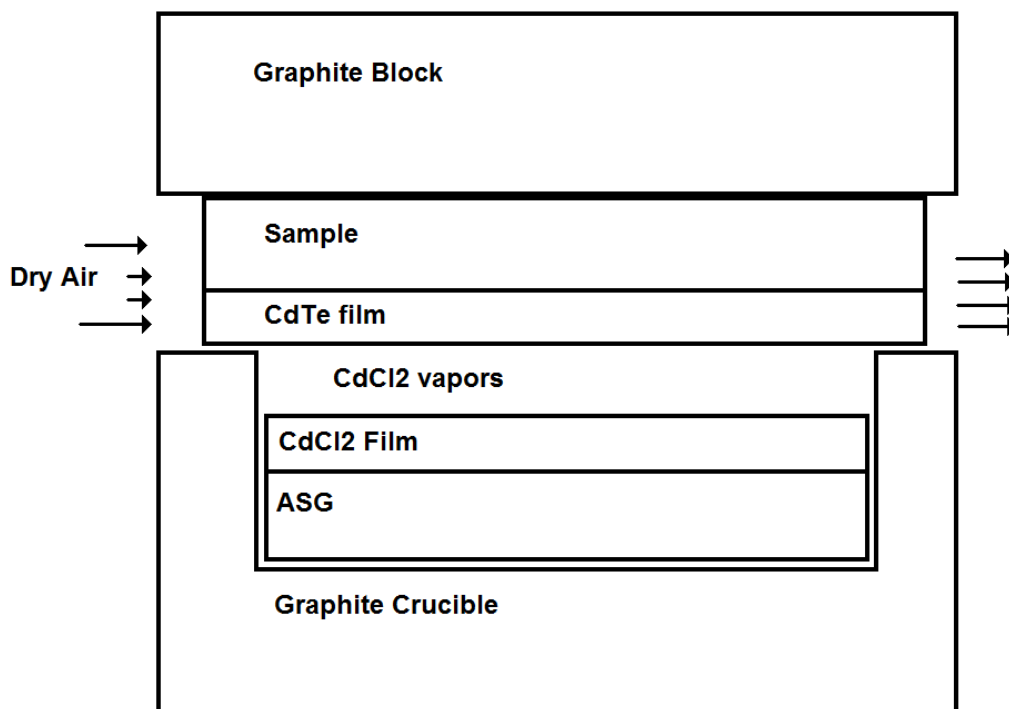
Figure 7.10. Our old vapor $CdCl_2$ treatment. The $CdCl_2$ source is a film on glass. When the graphite blocks are heated to 387C, $CdCl_2$ vapor pressure becomes significant and treats the CdTe film. Dry air periodically flows.

CdCl$_2$ is hygroscopic; it will absorb water from vapor in the air. Although we attempted to minimize the CdCl$_2$ film's exposure to atmosphere – the assemblage in figure 7.10 is in a quartz tube sealed from outside air – the system was opened to air whenever a sample was loaded and unloaded. Also, CdCl$_2$ reacts with oxygen; eventually, the CdCl$_2$ film would become cadmium chlorate and need to be replaced.

We considered testing material from the film for oxygen or water but our colleagues who perform inductively coupled plasma (ICP) measurements wanted to dissolve the material in water before performing ICP, which would defeat the entire purpose of the experiment.

In any case, the problem could be summarized as simply a result of using a single source of CdCl$_2$ for treating multiple films, though the CdCl$_2$ may not be stable for multiple films, and the stability of the CdCl$_2$ may be controlled by other variables, such as ambient humidity.

This motivated us to switch to a "wet" CdCl$_2$ treatment. For this treatment, methanol saturated with CdCl$_2$ was applied directly to the CdTe film being treated. I used about 0.2 mL of solution for a 3x3 inch sample. The solution was dried (only moderate heating of a sample was needed for the methanol to dry almost upon application) and then placed in the same crucible as shown in figure 7.10 (though minus the glass with the CdCl$_2$ film).

When performing a wet treatment, some CdCl$_2$ remains on the CdTe after treatment. It is possible to try to rinse away the remaining CdCl$_2$, but we have not done so with this particular study.

Through use of this treatment, we saw improvement in the consistency of our results.

7.5 Wet CdCl$_2$ Treatment Optimization

We applied the wet CdCl$_2$ treatment to our cells on polymer.

By this point, since we had already demonstrated that improved yield and reduced shunt conductance were possible on cells on polymer, we wished to have a path available for higher current if more transparent polymer substrates were used. Thus, we returned to a more usual CdS thickness of about 100nm (and also standard CdTe thickness of about 2.4µm), while using an HRT layer of 1x10^6 ohm-µm and 0.1µm thick. By previous considerations, even this HRT layer (0.01ohm-cm^2) will have virtually no effect on series resistance.

We optimized the CdCl$_2$ treatment using cells grown on 50µm Kapton. There were several reasons for this. Thicker polyimide films are easier to work with. Free standing thin (say, 12.5µm thick) polyimide films are flimsy, easily develop crinkles, and are influenced by static electricity. Working with them by hand is akin to working with plastic wrap. See Figure 7.11. This is not merely an issue of convenience. Sharp crinkles can be causes for cracks in semiconductor layers, and deformation of the substrate during chloride treatment is believed to relate to film delamination. If delamination occurred during treatment of a device on thicker polyimide, we would expect the same treatment to lead to delamination for thinner polyimide as well. Therefore, we considered early optimization with 50µm Kapton would provide the most meaningful results.   Also, 50µm Kapton, while thick, was sufficiently transparent. Some

reasonable results had already been obtained with 50μm Kapton with the previous

chloride treatment. As a simple practical consideration, for various reasons which do not

need exploring at this juncture, 50 μm Kapton was the most abundantly available

polyimide film for optimization experiments.
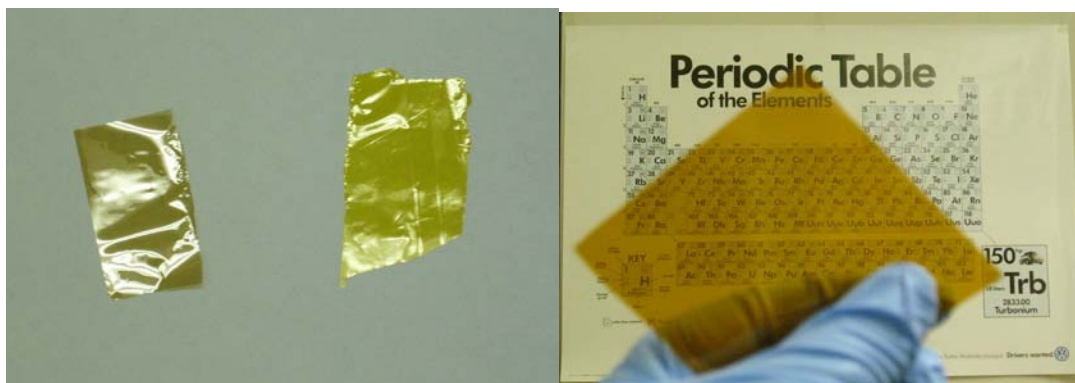
Figure 7.11. Polyimide films. Thin polyimide films of 12.5μm (left picture) (Upilex is on the left, Kapton is on the right) are flimsy. Polyimide films are also not perfectly clear but are yellow, orange, or ochre. However, even thick films of 125μm Kapton (right) are partially transparent. Thicker films are also more mechanically rigid.

We used our standard $CdCl_2$ treatment temperature of 387°C but varied the

treatment time.

Our standard treatment time for 2.4 μm cells on glass is 30 minutes. However,

this time is immediately ruled out as a possible optimum as even 20 minutes of treatment

time led to film delamination. Wet $CdCl_2$ is evidenced to be an even harsher treatment

than vapor treatment (though film delamination on some samples with vapor treatment

had also been observed).

Initial optimization was done with 50μm Kapton, but delamination with 20

minute CdCl2 treatments was observed in various other samples. See Figure 7.12.

Figure 7.12. CdTe film delamination as a consequence of 20 minute CdCl$_2$ treatment time. (left) 50 μm Kapton. Chunks of CdTe have flaked off from the substrate. (middle) 12.5 mm Upilex. The ochre substrate is partially visible through regions of missing CdTe. (right) An alternative polyimide, which also had CdTe delamination.

In some cases, CdTe delamination is not complete, and we might wonder what the performance is of areas which remain. However, since growing dot cells on polymer should eventually lead to photovoltaic large area modules on polymer, such results are simply considered failures. (In any case, in situations when dot cells where measured on the remaining CdTe, no cell surpassed the efficiency of our best polymer cell)

10 minute treatment times have led to very poor cells which often exhibit "roll-under" in their JV curves. See Figure 7.13. Roll-over is defined as negative second derivative in the JV curve; roll-under is when this negative second derivative is in the fourth quadrant. We saw in Figure 3.8 that role-under is possible with strong back barriers; however, those curves also were nearly parallel to the x-axis in the first quadrant. The cell in figure 7.13 rolls under but also exhibits secondary exponential turn on; that is, the second derivative becomes positive again in the first quadrant. This cannot be modeled by two diodes, a forward and back. It can be modeled by four diodes, a pair of forward and reverse diodes in parallel, one pair of which is "stronger" than the other; for real cells, this is interpreted to be an indication of nonuniformity[54].

180
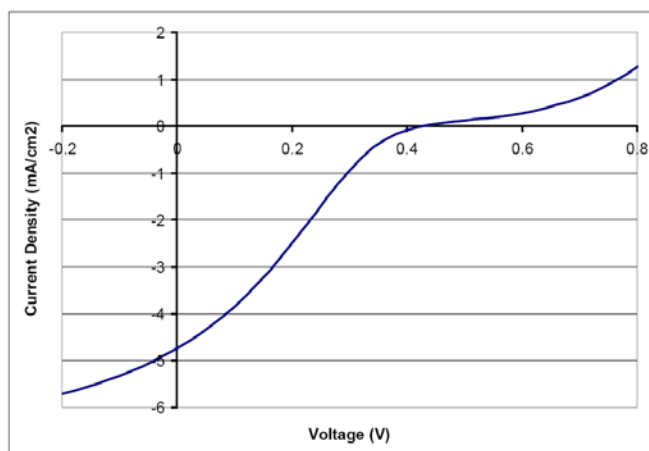
Figure 7.13. JV of CdTe cell on 50μm Kapton, CdCl2 treated for 10 minutes, exhibiting roll-under.

This is evidence that cells treated for ten minutes are not only uniformly undertreated, but that treatment progress varies spatially.

Between the previous limits, we have found 14 minutes treatment has led to good cell performance, with no film delamination (100% cell yield). The best cell was 7.2%; JV is shown in figure 7.14. This is better than the previous cell result using a vapor treatment, establishing the wet treatment not only as viable but as the best current recipe for our polymer cells.
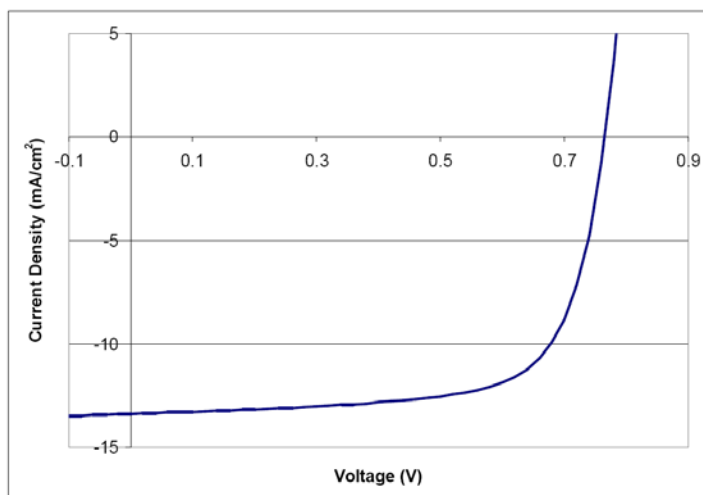
Figure 7.14. Best cell on 50μm Kapton, produced with wet CdCl$_2$ treatment. Voc=765mV, Jsc=13.4mA/cm2, fill factor=70.2%. Efficiency=7.2%.

7.6 Extension to Other Substrates

Figure 7.15 shows transmission data (line of sight, reflection losses included) of several possible substrates for solar cells. Pilkington Tec15 is a standard glass substrate used in our laboratory, and is included for comparison to polymer substrates. Kapton and Upilex are two competing brands of commercial polyimide.
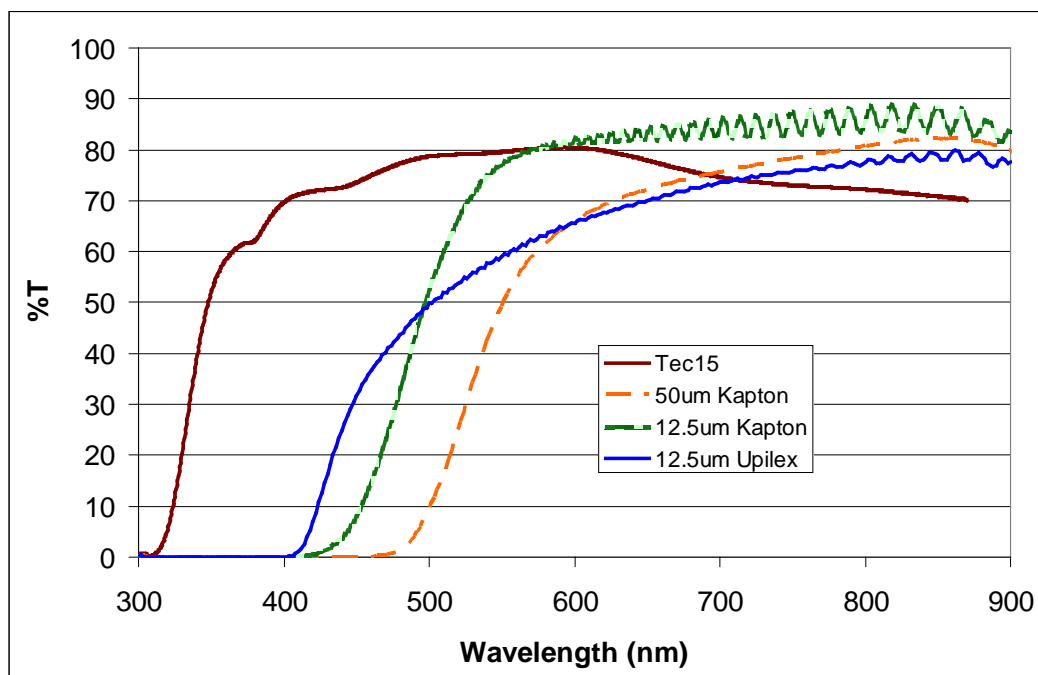
Figure 7.15. Transmission curves for selected possible solar cell substrates.

As seen, polyimide transmission, even for thicker films, at long wavelengths compares favorably to Tec 15. However, for all three polyimides transmission below 450nm is poor, and below 550 nm transmission is poor unless thin substrates are used.

Due to improved transmission in thinner films, we would expect higher current and thus cell performance is possible than what was obtained from 50μm thick Kapton. We thus wished to see whether our best recipe would translate to other substrates.

This recipe indeed translates to Upilex (see below). Also, Tiwari's group reported their best flexible performance with Upilex. However, we see in Figure 7.15 that, for equivalent thicknesses, Kapton is more transparent than Upilex.

Unfortunately, we did not see substantially improved performance when using thinner Kapton films. We obtained a 7.5% efficient cell on 25μm Kapton, which is a slight but not significant improvement over the 50μm Kapton cell. The reason improvement was so slight is not yet completely understood. For 12.5μm Kapton, even a 14 minute $CdCl_2$ treatment time was not short enough to prevent film delamination.

This might suggest that delamination during $CdCl_2$ treatment might not exclusively be an issue of inherent adhesion between semiconductor films and substrate, but that delamination could occur as the polyimide deforms slightly (if only due to thermal expansion) at high temperature. We would certainly expect CdTe delamination in the case of extreme physical deformation (say, if we grabbed a cell in our hands and rapidly flexed it back and forth).

This leads us to suspect that the mechanical properties of Kapton and Upilex are responsible for the superior performance of Upilex. Figure 7.16 shows data on the tensile strength of 25μm Upilex and Kapton[55,56]; the value for Upilex is higher. Also, Rabilloud states, "Upilex S is preferred to Kapton H when applications requires [sic] high modulus and low coefficient of linear thermal expansion."[57] The linear expansion coefficient of Upilex is $8x10^{-6}$/K while the linear expansion coefficient of Kapton is $2x10^{-5}$/K[58].
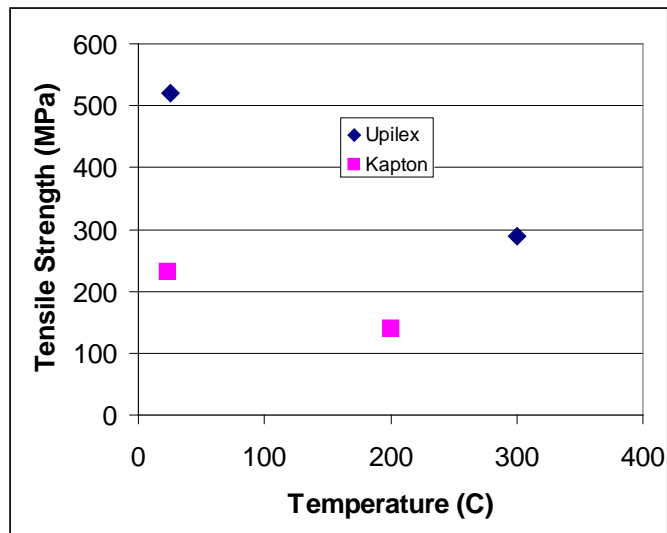
Figure 7.16. Tensile strength of 25µm Upilex and Kapton films at different temperatures. (from [55] and [56])

7.7 Best Cell

When we applied the wet chloride treatment and cell structure recipe described in the previous section to a device on 7.5µm Upilex we obtained our best result. The JV, light and dark, of the best cell is shown in Figure 7.17. The parameters are V_{OC}=768 mV, J_{SC}=19.5 mA/cm^2, fill factor=69.8%, and efficiency=10.5%.
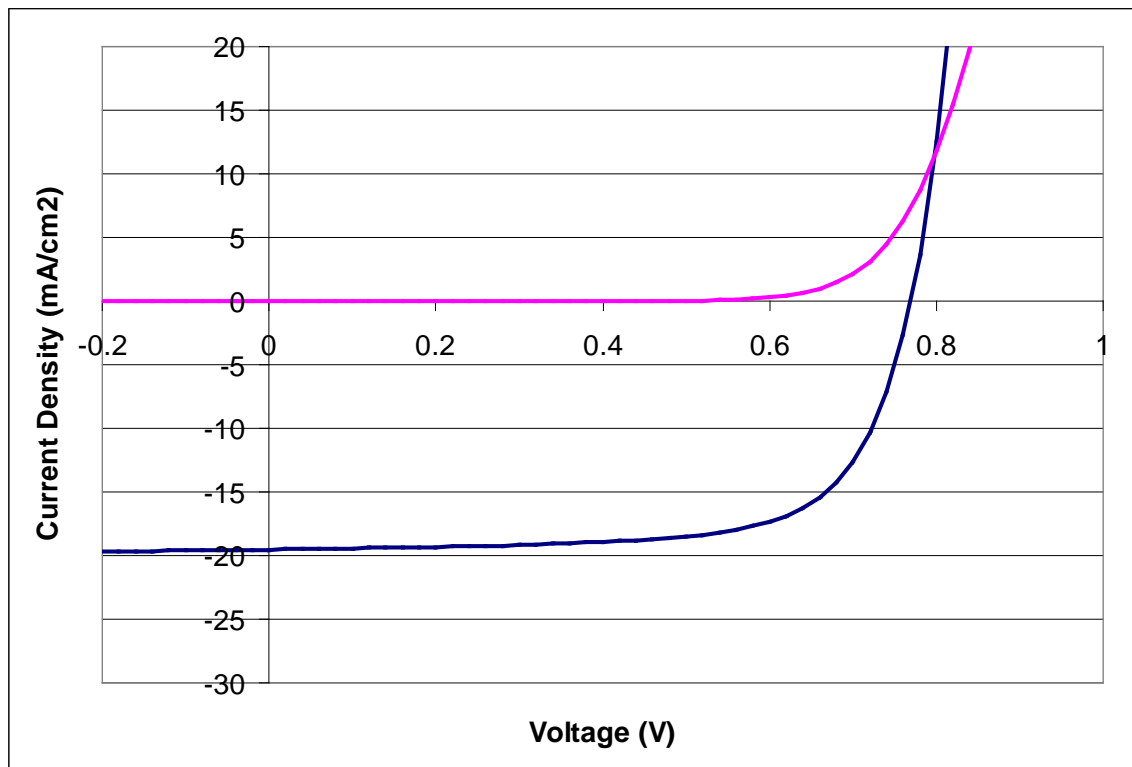
Figure 7.17. Best Cell on Polymer. Light and Dark curves of best cell on 7.5µm Upilex, made with wet chloride treatment. The parameters are V_{OC}=768 mV, J_{SC}=19.5 mA/cm^2, fill factor=69.8%, and efficiency=10.5%.

7.8 Conclusions and Future Work

Open circuit voltages for cells in this chapter have consistently been under 800mV, leaving room for improvement. The cause of this somewhat low voltage could be investigated in future work. Our chloride treatment times are shorter than for cells of equivalent thickness on glass. In our approach, it may was necessary to keep the activation treatment time low to avoid delamination so the cells may be slightly undertreated during the CdCl$_2$ step. Another possibility is that chloride treatment does progress faster for polyimide cells (due to, for example, chloride vapors permeating

185

through the polymer and treating the cell from both sides simultaneously). This could be

investigated further. If the CdCl$_2$ treatment is in fact insufficient for high voltage, other

approaches could perhaps maintain voltage while still preventing delamination.

Possibilities for investigation include depositing the CdTe at different pressures (compare

with Section 2.12 – controlling molybdenum delamination with sputter pressure), using

textured (as opposed to smooth) polyimide films to increase adhesion through increased

surface area, or using polymers that are adhered to glass (or similar rigid substrate)

throughout the deposition cycle so polymer deformation and thus film delamination is

less likely.

Secondary ion mass spectroscopy (SIMS) is a commonly used technique for

profiling elemental concentrations in devices (Auger analysis can give similar

information). A common result for CdTe cells is the discovery that copper from the back

contact has diffused all the way to the CdS. SIMS on flexible cells could potentially

show interesting information, such as whether any chemicals from the polyimide have

diffused into the semiconductor layers during fabrication and, if so, if any diffusion

barrier layers may be deposited to prevent such diffusion.

Polymer transparency is a dominant factor in cell performance. The performance

of the best cell on 50μm Kapton is very similar to the best cell on 7.5μm Upilex, aside

from current, which is mostly determined by the substrate. We would expect future work

that could use more transparent substrates, if or when they would be available, to result in

even higher cell performance.

Working through the difficulties presented in this chapter (and thesis generally)

suggests a program for improving cells when similar challenges are encountered. For

example, experiments on fill factor as a function of cell area are useful for determining the effect of TCO sheet resistance on cell performance, especially for flexible cells. We believe these results would have been extremely useful to us as a diagnostic had they been available earlier. We would also recommend anyone attempting to duplicate or further this work to understand and use this principle.

There is opportunity for further work to experimentally study the predictions made regarding the effects of including an HRT. Intentionally making pinholes or shunts is a possible path for confirming those predictions, but care must be taken that any intentional pinholes produced in CdTe (such as by laser ablation) do not damage the HRT or TCO. As some approximations were used in developing the HRT calculations, the calculations could be furthered by using fewer approximations. For example, it is possible to include the effect of what lateral current flow remains in the HRT.

Another possibility for dealing with shunts is to use a treatment with aniline or similar[41]. In our early studies of using this technique on polymer, we have found that the aniline chemical bath can be harsh enough to remove the CdTe from the substrate. Applying this technique to polymer cells, then, will require new optimization if not drastic modifications.

We have devoted significant effort to understanding AZO but it would at least be possible to attempt to use ITO as a TCO, as in Tiwari's work. Our early cells with ITO (even on glass substrates) were very poor, however, so work would be needed to progress in this area.

Even now, the state of small cell performance is good enough that another step that could be taken in the near future would be using our fabrication procedure to make

larger area cells and laser scribed and interconnected models on flexible substrates. Some work on this has already begun. Shunting and series resistance issues are even more pronounced with larger cells and modules, so techniques developed for small area cells will be challenged further with module production. Work may also be required to determine what laser parameters may be used to scribe the various cell layers without damaging the polyimide (which is usually not very transparent) substrate.

In this chapter, we have mapped a series of continuous improvements to the performance of our cells on polymer, overcoming in turn challenges such as high series resistance (AZO instability), high shunt conductance, and film delamination. After overcoming these challenges, we have succeeded in fabricating a flexible cell of 10.5% efficiency.

References

[1] "Economics of the Energy Industries", William Spangar Peirce, pp. 187, Praeger Publishers, 1996

[2] "Nuclear Energy and the Fossil Fuels", M. King Hubbert, Drilling and Production Practice, 1956

[3] http://www.ez2c.de/ml/solar_land_area/ (retrieved July 3, 2009)

[4] "Residential Photovoltaics; An Investment Vehicle for Retiree's III", Edward J. Simburger, Joseph T. Simburger, Thirty Fourth IEEE PVSC, June 2009

[5] "The Handbook of Photovoltaic Science and Engineering", Jeffery L. Gray, John Wiley and Sons, 2003, pp73

[6] "A Shortage Hits Solar Power", Roberta Bernstein, The Wall Street Journal, April 29, 2006

[7] http://www.fraunhofer.org/News/ISE_PI_e_World%20Recod.pdf

[8] http://rredc.nrel.gov/solar/spectra/am1.5/

[9] "Critical Issues in the Design of Polycrystalline, Thin-film Tandem Solar Cells", Timothy J. Coutts, J. Scott Ward, David L. Young, Keith A. Emery, Timothy A. Gessert and Rommel Noufi, Prog. Photovolt: Res. Appl. 2003; 11:359–375

[10] "19.9%-efficient ZnO/CdS/CuInGaSe2 solar cell with 81.2% fill factor", Ingrid Repins, Miguel A. Contreras, Brian Egaas, Clay DeHart, John Scharf, Craig L. Perkins, Bobby To, Rommel Noufi, Progress in Photovoltaics: Research and Applications 16, 235 (2008)

[11] "Optically induced conductivity changes in discharge-produced hydrogenated amorphous silicon", Staebler, D. L. and Wronski, C. R., J. Appl. Physics. 51(6), June 1980

[12] "The Handbook of Photovoltaic Science and Engineering", Antonio Luque and Antonio Marti´, John Wiley and Sons, 2003, pp123

[13] "Physical model of CdS-based thin-film photovoltaic junctions", M. L. C. Cooray and V. G. Karpov, Appl. Phys. Lett. 88, 093508 (2006)

[14] http://www.udel.edu/iec/CdTe.html (retrieved July 3, 2009)

[15] "Magnetron Sputtered CdTe Solar Cells on Flexible Substrates", Jennifer Drayton, Anthony Vasko, Akhlesh Gupta, A.D. Compaan, Conference Record of the Thirty-first IEEE Photovoltaic Specialists Conference, 2005, pp408

[16] "Copper Inclusion and Migration from the Back Contact in CdTe Solar Cells", C. R. Corwine, A. O. Pudov, M. Gloeckler, S. H. Demtsu, and J. R. Sites, Solar energy materials and solar cells, 2004, vol. 82, n°4, pp. 481-489

[17] "High-efficiency polycrystalline CdTe thin-film solar cells", Xuanzhi Wu, Solar Energy, Volume 77, Issue 6, December 2004, Pages 803-814

[18] "Quantification of Losses in Thin-Film CdS/CdTe Solar Cells", S.H. Demtsu and J.R. Sites, Conference Record of the Thirty-first IEEE Photovoltaic Specialists Conference, 2005, Pages 347-350.

[19] "Life cycle impact analysis of cadmium in CdTe PV production", Vasilis M. Fthenakis, Renewable and Sustainable Energy Reviews, 8 (2004) 303–334

[20] "Emissions from Photovoltaic Life Cycles", Vasilis M. Fthenakis, Hyung Chul Kim and Erik Alsema, *Environ. Sci. Technol.*, 2008, 42 (6), pp 2168–2174

[21] http://en.wikipedia.org/wiki/Template:Plastics (retrieved June 3, 2009)

[22] "Flexible CdTe Solar Cells on Polymer Films", A. N. Tiwari, A Romeo, D. Baetzner, H. Zogg, Prog. Photovolt: Res. Appl. 2001; 9:211-215

[23] "High-efficiency flexible CdTe solar cells on polymer substrates", A. Romeo, G. Khrypunov, F. Kurdesau, M. Arnold, D.L. Bätzner, H. Zogg and A.N. Tiwari, 14th International Photovoltaic Science and Engineering Conference, Solar Energy Materials and Solar Cells Volume 90, Issues 18-19, 23 November 2006, Pages 3407-3415

[24] "Verwendung von Schwingquarzen zur Waegung duenner Schichten und zur Mikrowaegung", Gunter Sauerbrey, Zeitschrift fur Physik 155, 206--222 (1959)

[25] "The Materials Science of Thin Films", Second Edition, Milton Ohring, Academic Press (2002), pp.150.

[26] "Plasma sources for thin film deposition and etching", Maurice H. Francombe and John L. Vossen (editors), Academic Press, 1994, pp.241

[27] *Ibid.,* pp 239

[28] "Correlation of Argon-Copper Sputtering Mechanisms with Experimental Data Using a Digital Computer Simulation Technique" (thesis), Herbert M. Effron, 1967, pp.34

[29] "Influence of substrate temperature and deposition rate on structure of thick sputtered Cu coatings", John A. Thornton, J. Vac. Sci. Technol., Vol. 12, No. 4, July/Aug. 1975, pp.830-835.

[30] http://en.wikipedia.org/wiki/Poisson's_ratio (retrieved July 6, 2009)

[31] "The Handbook of Photovoltaic Science and Engineering", Jeffery L. Gray, John Wiley and Sons, 2003, pp. 102-104

[32] "Thin-Film Solar Cells Device Measurements and Analysis", Steven S. Hegedus and William N. Shafarman, Progress in Photovoltaics: Research and Applications, 2004, 12:115-176

[33] "Impact of sheet resistance on 2-D modeling of thin-film solar cells", Galymzhan T. Koishiyev and James R. Sites, Solar Energy Materials and Solar Cells, Volume 93, Issue 3, March 2009, Pages 350-354

[34] "The effect of the front contact sheet resistance on solar cell performance", M.W. Denhoff and N. Drolet, Solar Energy Materials and Solar Cells, Volume 93, Issue 9, September 2009, Pages 1499-1506

[35] "Shunt screening, size effects and I/V analysis in thin-film photovoltaics", V. G. Karpov, G. Rich, A. V. Subashiev, and G. Dorer, Journal of Applied Physics, Volume 89, Number 9, 2001

[36] "Thin-Film Solar Cells: An Overview", K. L. Chopra, P. D. Paulson and V. Dutta, Prog. Photovolt: Res. Appl. 2004; 12:69–92

[37] "Electronic properties of ZnO/CdS/Cu(In,Ga)Se$_2$ solar cells — aspects of heterojunction formation", Uwe Rau and Marion Schmidt, Thin Solid Films, Volume 387, Issues 1-2, 29 May 2001, Pages 141-146

[38] "Measurement of Sheet Resistivities with the Four-Point Probe", F. M. Smits, The Bell System Technical Journal, 1958

[39] http://sites.google.com/site/resistorgrid/grid

[40] "Lock-in thermography and nonuniformity modeling of thin-film CdTe solar cells", Diana Shvydka, J. P. Rakotoniaina and O. Breitenstein, Applied Physics Letters, Volume 84, Number 5, pp. 729-731

[41] "Blocking thin-film nonuniformities: Photovoltaic self-healing", Y. Roussillon, D. M. Giolando, Diana Shvydka, A. D. Compaan, and V. G. Karpov, Applied Physics Letters, Vol. 84, No. 4, pp. 616–618, 26 January 2004

[42] "A simple method for the determination of the optical constants n, k and the thickness of a weakly absorbing thin film", J C Manifacier, J Gasiot and J P Fillard, Journal of Physics E: Scientific Instruments, Volume 9, issue 11, November 01, 1976, pp. 1002-1004

[43] "Photo-excited processes, diagnostics, and applications", Aaron Peled, Springer, 2003, p. 34.

[44] "Carrier concentration dependence of band gap shift in n-type ZnO:Al films", J. G. Lu, S. Fujita, T. Kawaharamura, H. Nishinaka, Y. Kamada, T. Ohshima, Z. Z. Ye, Y. J. Zeng, Y. Z. Zhang, L. P. Zhu, H. P. He, and B. H. Zhao, J. Appl. Phys. **101**, 083705 (2007)

[45] "Anomalous Optical Absorption Limit in InSb", Elias Burnstein, Phys. Rev. **93**, 632 (1954), pp. 632-633

[46] "The Handbook of Photovoltaic Science and Engineering", page 591

[47] "Residual Native Shallow Donor in ZnO", D. C. Look, J. W. Hemsky, J. R. Sizelove, Physical Review Letters, Volume 82, Number 12, pp.2552-2555 (1999)

[48] "Influence of Oxygen Addition and Substrate Temperature on Textured Growth of Al-Doped ZnO Thin Films Prepared by RF Magnetron Sputtering", P. Kuppusami, K. Diesner, I. Sieber, K.Ellmer, Mat. Res. Soc. Symp. Proc. Vol. 721

[49] "Polycrystalline intrinsic zinc oxide to be used in transparent electronic devices", A. Pimentel, E. Fortunato, A. Gonçalves, A. Marques, H. Águas, L. Pereira, I. Ferreira and R. Martins, Thin Solid Films, Volume 487, Issues 1-2, 1 September 2005, Pages 212-215

[50] "Improving the Repeatability of Ultra-High Resistance and Resistivity Measurements" (white paper), Adam Daire, www.keithley.com, 2001

[51] *Ibid.*

[52] "Damp-Heat Induced Degradation of Transparent Conducting Oxides for Thin-Film Solar Cells", F.J. Pern, R. Noufi, X. Li, C. DeHart, and B. To, 33rd IEEE Photovoltaic Specialists Conference, (2008)

[53] "Non-uniformity mitigation in CdTe solar cells: the effects of high-resistance transparent conducting oxide buffer layers", Feldman, S.D., Mansfield, L.   Ohno, T.R., Kaydanov, V., Beach, J.D., Nagle, T., Conference Record of the Thirty-first IEEE Photovoltaic Specialists Conference, 2005, pp. 271-274

[54] "Effects of non-uniformity on rollover phenomena in CdS/CdTe solar cell", A.R. Davies and J.R. Sites, Thirty-Third IEEE PVSC, May 2008

[55] http://northamerica.ube.com/content.php?pageid=81

[56] http://www2.dupont.com/Kapton/en_US/assets/downloads/pdf/summaryofprop.pdf

[57] "High-performance polymers", Guy Rabilloud, Institut Francais Du Petrole Publications, 1999, page 91

[58] *Ibid.*

Appendix A

Source Code For Extraction of Thin Film Parameters from Transmission Data

```
REM Program written June 2007 by Anthony Vasko

REM Calculates various properties of a Thin Film
REM using "A simple method for the determination of the optical
REM constants n, k and the thickness of a weakly absorbing thin film",
REM Journal of Physics E: Scientific Instruments, Volume 9, issue 11,
REM November 01, 1976, p. 1002-1004,
REM by J C Manifacier, J Gasiot and J P Fillard


REM This method requires, consecutively, a maximum, a minimum, and
REM another maximum in the transmission data, or a minimum, maximum,
REM and another minimum.

REM Wavelengths can be in any unit; the thickness will be given in the same
REM unit.

REM Likewise, the absorption coefficient is given in the inverse of that
REM unit.

REM Transmission is expected in percent.  That is, complete transmission
REM would be 100, not 1.

REM This also assumes the film is between air (nb = 1) and
REM soda lime glass (na = 1.5)

again:

PRINT "Two Ma(x)ima or Two Mi(n)ima?"

DO
a$ = INKEY$
IF a$ = "x" OR a$ = "X" THEN GOTO max
IF a$ = "n" OR a$ = "N" THEN GOTO min
IF a$ = CHR$(27) THEN END


LOOP

max:

PRINT "Enter Lamba 1 (first maximum)"
INPUT l1
PRINT "Enter %T1"
INPUT T1
PRINT "Enter Lamba 2 (minimum)"
INPUT l2
PRINT "Enter %T2"
INPUT T2
PRINT "Enter Lamba 3 (second maximum)"
INPUT l3
PRINT "Enter %T3"
INPUT T3

T1 = T1 / 100
T2 = T2 / 100
T3 = T3 / 100
```

```
na = 1.5                    'index of refraction of Soda Lime Glass
nb = 1                      'index of refraction of air


NN = (na ^ 2 + nb ^ 2) / 2 + 2 * na * nb * (T1 - T2) / (T1 * T2)

n1 = (NN + (NN ^ 2 - na ^ 2 * nb ^ 2) ^ (1 / 2)) ^ (1 / 2)

NN = (na ^ 2 + nb ^ 2) / 2 + 2 * na * nb * (T3 - T2) / (T3 * T2)


n2 = (NN + (NN ^ 2 - na ^ 2 * nb ^ 2) ^ (1 / 2)) ^ (1 / 2)



thick = l1 * l3 / (2 * (n1 * l3 - n2 * l1))


PRINT


PRINT "Thickness ="; thick


PRINT "Index of refraction at lower lambda ="; n1
PRINT "...at higher lambda ="; n2


c11 = (n1 + na) * (nb + n1)

c21 = (n1 - na) * (nb - n1)

alpha1 = c11 * (1 - (T1 / T2) ^ (1 / 2)) / (c21 * (1 + (T1 / T2) ^ (1 / 2)))

k1 = LOG(1 / alpha1) / thick

c12 = (n2 + na) * (nb + n2)

c22 = (n2 - na) * (nb - n2)

alpha2 = c12 * (1 - (T3 / T2) ^ (1 / 2)) / (c22 * (1 + (T3 / T2) ^ (1 / 2)))

k2 = LOG(1 / alpha2) / thick

PRINT "Absorption coeff. at lower lambda ="; k1
PRINT "... at greater lambda ="; k2

PRINT


PRINT "Run again? (y/n)"

DO
a$ = INKEY$
IF a$ = "Y" OR a$ = "y" THEN GOTO again
IF a$ = "n" OR a$ = "N" OR a$ = CHR$(27) THEN END

LOOP

min:
```

```
PRINT "Enter Lamba 1 (first minimum)"
INPUT l1
PRINT "Enter %T1"
INPUT T1
PRINT "Enter Lamba 2 (maximum)"
INPUT l2
PRINT "Enter %T2"
INPUT T2
PRINT "Enter Lamba 3 (second minimum)"
INPUT l3
PRINT "Enter %T3"
INPUT T3

T1 = T1 / 100
T2 = T2 / 100
T3 = T3 / 100




na = 1.5                  'index of refraction of Soda Lime Glass
nb = 1                    'index of refraction of air


NN = (na ^ 2 + nb ^ 2) / 2 + 2 * na * nb * (T2 - T1) / (T1 * T2)

n1 = (NN + (NN ^ 2 - na ^ 2 * nb ^ 2) ^ (1 / 2)) ^ (1 / 2)

NN = (na ^ 2 + nb ^ 2) / 2 + 2 * na * nb * (T2 - T3) / (T3 * T2)


n2 = (NN + (NN ^ 2 - na ^ 2 * nb ^ 2) ^ (1 / 2)) ^ (1 / 2)



thick = l1 * l3 / (2 * (n1 * l3 - n2 * l1))

PRINT

PRINT "Thickness ="; thick


PRINT "Index of refraction at lower lambda ="; n1
PRINT "...at higher lambda ="; n2


c11 = (n1 + na) * (nb + n1)

c21 = (n1 - na) * (nb - n1)

alpha1 = c11 * (1 - (T2 / T1) ^ (1 / 2)) / (c21 * (1 + (T2 / T1) ^ (1 / 2)))

k1 = LOG(1 / alpha1) / thick

c12 = (n2 + na) * (nb + n2)

c22 = (n2 - na) * (nb - n2)

alpha2 = c12 * (1 - (T2 / T3) ^ (1 / 2)) / (c22 * (1 + (T2 / T3) ^ (1 / 2)))

k2 = LOG(1 / alpha2) / thick
```

```
PRINT "Absorption coeff. at lower lambda ="; k1
PRINT "... at greater lambda ="; k2




PRINT


PRINT "Run again? (y/n)"

DO
a$ = INKEY$
IF a$ = "Y" OR a$ = "y" THEN GOTO again
IF a$ = "n" OR a$ = "N" OR a$ = CHR$(27) THEN END

LOOP
```